STORAGE CAPACITY AND REGIONAL IMPLICATIONS FOR LARGE-SCALE STORAGE IN THE BASAL CAMBRIAN SYSTEM

Plains CO_2 Reduction (PCOR) Partnership Phase III
Task 16 – Deliverable D92

Prepared for:

Andrea M. Dunn

National Energy Technology Laboratory
U.S. Department of Energy
626 Cochrans Mill Road
PO Box 10940
Pittsburgh, PA 15236-0940

DOE Cooperative Agreement No. DE-FC26-05NT42592

Prepared by:

Wesley D. Peck
Guoxiang Liu
Robert C.L. Klenner
Megan M. Grove
Charles D. Gorecki
Edward N. Steadman
John A. Harju

Energy & Environmental Research Center
University of North Dakota
15 North 23rd Street, Stop 9018
Grand Forks, ND 58202-9018

March 2014
2014-EERC-05-12 Approved

EERC DISCLAIMER

LEGAL NOTICE This research report was prepared by the Energy & Environmental Research Center (EERC), an agency of the University of North Dakota, as an account of work sponsored by the U.S. Department of Energy (DOE) National Energy Technology Laboratory (NETL). Because of the research nature of the work performed, neither the EERC nor any of its employees makes any warranty, express or implied, or assumes any legal liability or responsibility for the accuracy, completeness, or usefulness of any information, apparatus, product, or process disclosed or represents that its use would not infringe privately owned rights. Reference herein to any specific commercial product, process, or service by trade name, trademark, manufacturer, or otherwise does not necessarily constitute or imply its endorsement or recommendation by the EERC.

ACKNOWLEDGMENT

This material is based upon work supported by DOE NETL under Award No. DE-FC26-05NT42592.

DOE DISCLAIMER

This report was prepared as an account of work sponsored by an agency of the United States Government. Neither the United States Government, nor any agency thereof, nor any of their employees, makes any warranty, express or implied, or assumes any legal liability or responsibility for the accuracy, completeness, or usefulness of any information, apparatus, product, or process disclosed, or represents that its use would not infringe privately owned rights. Reference herein to any specific commercial product, process, or service by trade name, trademark, manufacturer, or otherwise does not necessarily constitute or imply its endorsement, recommendation, or favoring by the United States Government or any agency thereof. The views and opinions of authors expressed herein do not necessarily state or reflect those of the United States Government or any agency thereof.

NDIC DISCLAIMER

This report was prepared by the EERC pursuant to an agreement partially funded by the Industrial Commission of North Dakota, and neither the EERC nor any of its subcontractors nor the North Dakota Industrial Commission (NDIC) nor any person acting on behalf of either:

(A) Makes any warranty or representation, express or implied, with respect to the accuracy, completeness, or usefulness of the information contained in this report or that the use of any information, apparatus, method, or process disclosed in this report may not infringe privately owned rights; or

(B) Assumes any liabilities with respect to the use of, or for damages resulting from the use of, any information, apparatus, method, or process disclosed in this report.

Reference herein to any specific commercial product, process, or service by trade name, trademark, manufacturer, or otherwise does not necessarily constitute or imply its endorsement, recommendation, or favoring by the North Dakota Industrial Commission. The views and opinions of authors expressed herein do not necessarily state or reflect those of the North Dakota Industrial Commission.

TABLE OF CONTENTS

Continued…

TABLE OF CONTENTS (continued)

LIST OF FIGURES

Continued…

LIST OF FIGURES (continued)

Continued…

LIST OF FIGURES (continued)

LIST OF TABLES

STORAGE CAPACITY AND REGIONAL IMPLICATIONS FOR LARGE-SCALE STORAGE IN THE BASAL CAMBRIAN SYSTEM

EXECUTIVE SUMMARY

A binational effort, between the United States and Canada, characterized the lowermost saline system in the Williston and Alberta Basins of the northern Great Plains–Prairie region of North America in the United States and Canada. This 3-year project was conducted with the goal of determining the potential for geologic storage of carbon dioxide (CO_2) in rock formations of the 517,000 sq mi Cambro-Ordovician Saline System (COSS). This project was led on the U.S. side by the Energy & Environmental Research Center (EERC) through the Plains CO_2 Reduction (PCOR) Partnership and on the Canadian side by Alberta Innovates Technology Futures (AITF). The project characterized the COSS using well log and core data from three states and three provinces and determined its storage potential by creating a heterogeneous 3-D model and determined the effects of CO_2 storage in this system using dynamic simulation. The area underlain by the COSS includes several large CO_2 sources that each emits more than 1 Mt CO_2/year. Assuming that each of these sources will target the COSS for the storage of their CO_2, the primary questions addressed by this study are 1) what is the CO_2 storage resource of the COSS, 2) how many years of current CO_2 emissions will it be capable of storing, and 3) what will be required and what will be the effect of injecting 104 Mt/yr of CO_2 into the COSS?

A 3-D geocellular model was created and used to determine the static CO_2 storage resource and the dynamic storage capacity. The complexity of the reservoir was characterized from numerous sources of data, including the online databases of North Dakota, South Dakota, and Montana and a wealth of data provided by project partners in Canada. Multimineral petrophysical analysis was conducted to determine the system's gross lithology and key petrophysical characteristics. Information derived from these analyses was used to create a facies model that captures the heterogeneity of the COSS at this broad scale. The completed geocellular model contains information on temperature, pressure, porosity, permeability, and salinity. These variables were distilled to produce components needed to compute the CO_2 storage resource of the COSS following the E_{saline} formula detailed by the U.S. Department of Energy (DOE) Office of Fossil Energy Atlas III and IV (2010, 2012). The resulting effective static CO_2 storage resource is 218, 412, and 706 Gt at the P10, P50, and P90 percentiles, respectively. This resource potential represents more than 2100 years of storage for the current 104 Mt/yr point source emissions.

To further evaluate this extensive system and thus its viability as a potential sink, the geocellular model was used as the framework for an assessment of the system's dynamic CO_2 storage capacity. In the area above the COSS, there are 25 large stationary sources that were

grouped into 16 geographic areas that have a combined annual emission of 104 Mt. With this in mind, the first injection scenario considered seven cases where the target was to inject this total mass of CO_2 for 36 or 50 years in the 16 injection areas using a total of 210 wells. Results from these cases show a total mass of CO_2 injected ranging from 82 to 1412 Mt across the injection period of 36 and 50 years. These values represent between 2.2% and 27.2% of the available CO_2 emitted from the 16 source locations. In the second scenario, eight new cases where the original 16 injection locations were disaggregated and moved (pipelined) to areas defined by the model as having good reservoir volume connection (geobodies) based on permeabilities greater than 50 mD. Injection amounts in the second scenario range from 1949 to 3112 Mt of CO_2. These values represent 37.5% to 59.8% of the CO_2 emitted from the source locations. Based on the results of both scenarios, the selection of areas with better permeability and connected volume had a large impact on increasing the total amount of CO_2 stored and the per well injection rates. However, even in the better area, the COSS was not able to support 211 injection wells with an average injection rate of 0.5 Mt/yr. In the second scenario, the average annual per well injection rate was between 185,000 and 275,000 tons/yr. At these injection rates, a total of 378 to 563 wells would have been required to meet the injection target. Pressure differences monitored in the second scenario show small changes in the 50-year injection time period. These minimal pressure differences indicate small risks of leakage from the reservoir and integrity of the sealing cap rock due to CO_2 injection in the COSS.

The results of the static CO_2 storage resource estimate indicate that the COSS has thousands of years of storage potential at the current point source CO_2 emission levels. However, the actual task of injecting the annual emissions is more difficult. Results from simulation indicate that injecting all the point source CO_2 in an area directly beneath the sources using 210 wells did not result in meeting the storage target. With that in mind, the COSS model and simulations were run on limited data, and just because these simulation cases indicated that the injection volumes, as a whole, could not be reached does not mean that the geology around a particular CO_2 source is poor. These results indicate that there is sufficient storage potential in the COSS to store all of the current point source CO_2 emissions for at least the next 50 years; however, more wells will likely be needed and spread out over more of the COSS to achieve this goal.

STORAGE CAPACITY AND REGIONAL IMPLICATIONS FOR LARGE-SCALE STORAGE IN THE BASAL CAMBRIAN SYSTEM

INTRODUCTION

Carbon capture and storage (CCS) in geologic media have been identified as important means for reducing anthropogenic greenhouse gas emissions into the atmosphere (Bradshaw and others, 2007). Several categories of geologic media for the storage of carbon dioxide (CO_2) are available, including depleted oil and gas reservoirs, deep brine-saturated formations, CO_2 flood enhanced oil recovery (EOR) operations, and enhanced coalbed methane recovery. The U.S. Department of Energy (DOE) is pursuing a vigorous program for demonstration of CCS technology through its Regional Carbon Sequestration Partnership (RCSP) Program, which entered its third phase (Phase III) in October 2007. This phase is planned for a duration of ten U.S. federal fiscal years (October 2007 to September 2017). One of the principal elements of the DOE effort is core R&D which includes a significant effort to identify geologic formations that can safely and efficiently store CO_2 over long periods of time.

As one of the seven RCSPs, the Plains CO_2 Reduction (PCOR) Partnership, led by the Energy & Environmental Research Center (EERC), is assessing the technical and economic feasibility of capturing and storing CO_2 emissions from stationary sources in the central interior of North America (Figure 1). Through a major regional characterization activity, the EERC and Alberta Innovates Technology Futures (AITF) completed characterization of the lowermost saline system in the Williston and Alberta Basins of the northern Great Plains–Prairie region of North America. The goal of these characterization efforts as carried out in Phase III determines the potential resource and the effects of large-scale injection of CO_2 into this deep saline reservoir through dynamic simulation.

The storage of captured CO_2 in geologic media is a technology that is immediately applicable as a result of the experience gained mainly in oil and gas exploration and production and deep waste disposal. Studies have also shown that geologic media has a large potential for CO_2 storage, with retention times of centuries to millions of years (Intergovernmental Panel on Climate Change [IPCC], 2005). Geologic storage of CO_2 is being actively investigated and pursued at several locations across the United States, Canada, and the world, including several sites in the PCOR Partnership region.

Three geologic media have been identified as suitable for CO_2 storage: uneconomical coal beds, depleted oil and gas reservoirs, and deep (<2500 feet) saline formations (also referred to as deep saline aquifers). Storage of CO_2 in coal beds has the smallest potential in terms of storage resource and is an immature technology that has not yet been proven (Bachu and others,

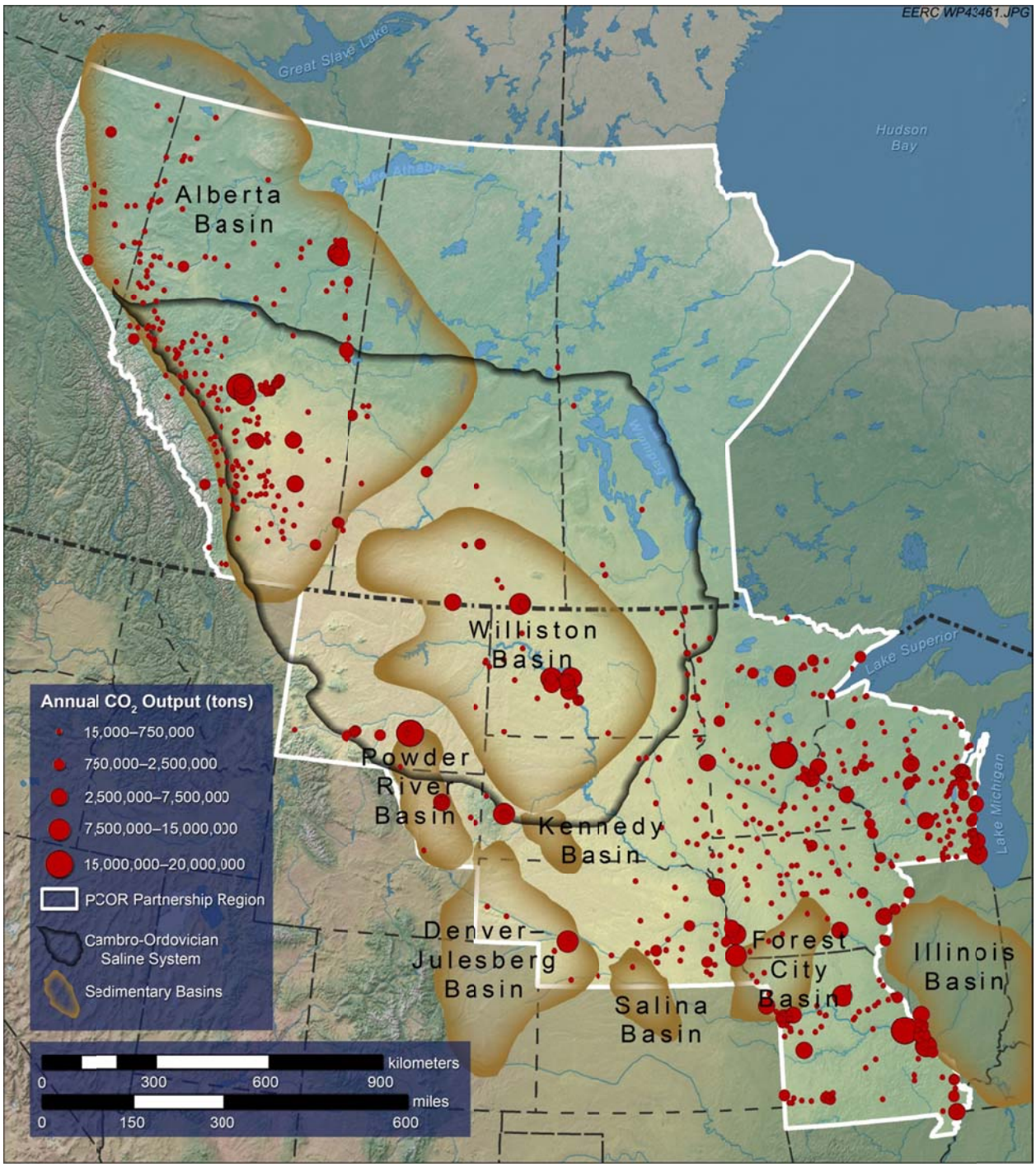

Figure 1. The PCOR Partnership region and the distribution of large stationary sources in relationship to sedimentary basins and the extent of the Cambro-Ordovician Saline System (COSS).

2011). Depleted hydrocarbon reservoirs have the advantage of demonstrating storage and confinement properties by having previously stored oil and/or gas resources for millions of years. The quest to discover and extract hydrocarbon resources has provided a broad base of

understanding about the subsurface in oil- and gas-producing areas. The potential downside is that the numerous wells that have been drilled in those areas may diminish storage security (Bachu and others, 2011). Deep saline formations have the advantage of being much more widespread and, theoretically, have correspondingly larger storage capacities than the other geologic media.

In the United States and Canada, various studies have been initiated for more than a decade to estimate the CO_2 storage resource at the country or regional level. Regional characterization efforts of the PCOR Partnership project have conducted several regional and local investigations to evaluate the CO_2 storage resource potential of deep saline formations in the Denver–Julesburg and Williston Basins. The formations investigated in these evaluations include the carbonates of the Madison and Red River Formations and the siliciclastics of the Deadwood, Black Island, Broom Creek, Newcastle, and Inyan Kara Formations in the Williston Basin. In the Denver–Julesburg Basin, the sandstones of the Maha Formation were evaluated for CO_2 storage resource potential. Bachu and Adams (2003) have estimated the storage resource for the carbonate Keg River and siliciclastic Viking saline formations in the Alberta Basin. The results of that specific work were also included in the CO_2 resource of the PCOR Partnership as reported to DOE for inclusion into the Carbon Sequestration Atlas of the United States and Canada (U.S. Department of Energy Office of Fossil Energy, 2007, 2008, 2010).

Work conducted in 2010 and 2011 by the Geological Survey of Canada (GSC) regarding the CO_2 storage potential and resource in Canada has identified the Alberta Basin and the Canadian part of the Williston Basin as the region in Canada with the greatest potential for CCS implementation. In those basins, the GSC has applied DOE's methodology (U.S. Department of Energy Office of Fossil Energy, 2008) to several saline formations, namely, the Elk Point, Beaverhill Lake, Woodbend, Winterburn, and Rundle–Charles Formations. The storage resource values derived in this work by GSC were included in the 4th edition (revised) of the PCOR Partnership Atlas (Peck and others, 2013) and the North American Atlas of CO_2 Storage Capacity (Bachu and others, 2011). Frequent and unfortunate by-products of the individual efforts conducted in this central interior portion of North America are evaluations and related maps that show a "fault line" (discontinuity) at the U.S.–Canadian border. Evaluating the resource and effects of CO_2 storage in the Canadian or U.S. portions of the Williston Basin should not be done in isolation. The regional geology of sedimentary basins is not influenced by political boundaries.

Energy production from fossil fuels is generally associated with sedimentary basins, and it is these same sedimentary basins that contain the geologic media suitable for CO_2 storage. This juxtaposition of large stationary sources of CO_2 and potential geologic storage targets makes for an opportune geographic relationship, and sixteen of these aggregated sources were used for the dynamic simulation. The COSS is the storage target for Shell's Quest project near Edmonton, Alberta, and the Aquistore project near Estevan, Saskatchewan. It is very possible that many large CO_2 emitters in the northern Great Plains–Prairie region of North America will choose to store CO_2 in this saline system because of its apparent large storage resource and because it is penetrated by relatively few wells, thus increasing the security of CO_2 storage. However, the storage resource of this saline system has not been previously thoroughly evaluated.

To address the evaluation and consideration of this extensive saline system and viability as a potential sink, the following objectives were established to be determined from the results of the static model creation and dynamic simulation: 1) assess the volumetric static CO_2 storage resource of the northern Great Plains–Prairie basal saline system based on its geometry, internal architecture, lithology, relative permeability and porosity, and temperature and pressure distributions; 2) assess the dynamic storage capacity of the saline system assuming that the 16 major large CO_2 sources located above or in close vicinity to this saline system will choose it for CO_2 storage during their respective lifetimes; and 3) assess the effect of pressure-related changes related to the injection of large volumes of CO_2.

STATIC MODEL

Different than the 2-D model completed in Phase II, the 3-D geocellular model takes into account the internal heterogeneity of complex facies relationships that exist vertically and laterally throughout the COSS. The goal of the modeling activities is to assess the volumetric CO_2 storage of the system based on its geometry, internal architecture, lithology, permeability and porosity, and temperature and pressure distributions. In addition, the geocellular model is also used for the dynamic simulation portion to determine dynamic storage and the effects of reservoir pressure buildup.

The complexity of the reservoir was characterized from numerous sources of data. Well data used in the development of the 3-D model across the U.S. portion of the basal saline system were obtained from the online databases of the North Dakota Industrial Commission and the Montana Board of Oil and Gas. Data were also obtained from the Montana Geological Society and the South Dakota Geologic Survey. Data from these organizations included formation tops, well files, which included core measurements, and wireline logs in raster and, in many cases, Log ASCII (LAS) format. Other forms of data were included from Bachu and others (2011) who went through a similar process to characterize the basal saline system in Canada. Figure 2 shows a general workflow for the 3-D model construction of the basal saline system.

Study Area

The central interior portion of North America covered in this report encompasses the northern Great Plains–Prairie region of the United States and the southern Interior Plains of Canada. This region of North America is generally characterized by broad expanses of relatively flat land covered by prairie, steppe, and grassland and is bounded by the Canadian Shield to the northeast, the Rocky Mountains to the west, and the central lowlands of Minnesota and Iowa to the southeast. In addition to the strong agricultural focus, this region is also home to a robust energy industry that includes coal, oil, and gas development. The abundant energy resources of this area have resulted in the establishment of many large-scale CO_2 sources such as coal-fired power plants and refineries.

Similar to the Mt. Simon Formation that overlies the Precambrian crystalline basement in the U.S. Midwest (Leetaru and McBride, 2009; Barnes and others, 2009), the COSS overlies the

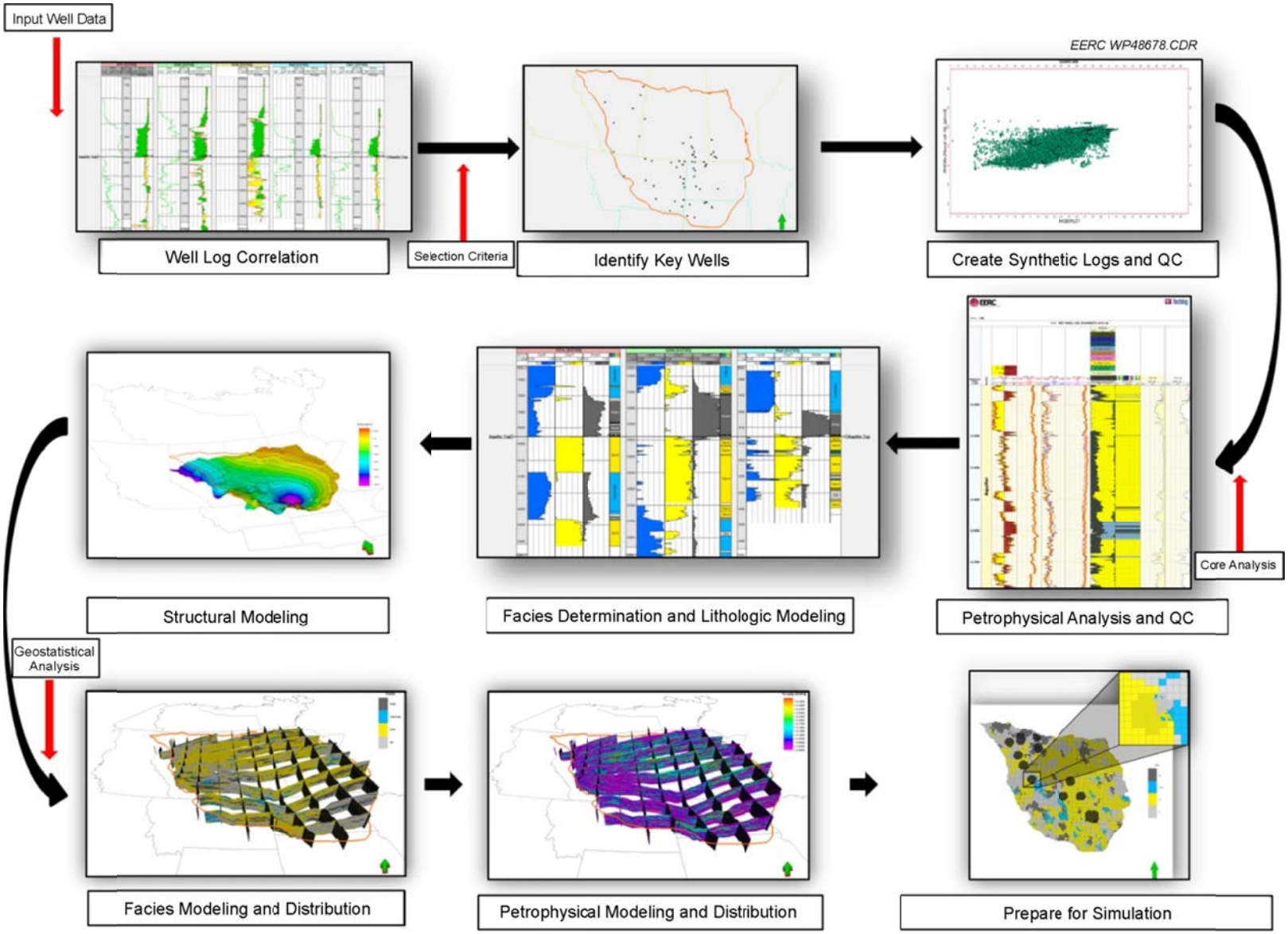

Figure 2. Workflow method used to build the basal saline system model.

Precambrian basement in the northern Great Plains–Prairie region, extending from north of Edmonton, Alberta, to South Dakota and covering a combined area of ~517,000 sq mi. The Canadian part of the saline system covers 313,285 sq mi, and the U.S. part covers ~195,814 sq mi (Figure 3). Given its reservoir characteristics and extent, this basal saline system should be considered as a prime target for the storage of CO_2 from large stationary sources in the northern Great Plains and Prairie region. In addition, most of the Cambrian to Silurian strata at the base of the sedimentary succession in Williston and Alberta Basins do not contain fossil fuels and also has limited prospects for unconventional oil or gas production, and as such, little of the prospective storage space is leased.

Stratigraphic Correlation

The greater Williston Basin area has been explored for oil and gas resources for over 70 years and thus has had a large number of wells drilled into it. However, only wells that penetrated the contact of the Black Island and overlying Ice Box Formations or deeper were examined in this study for stratigraphic correlation. Of primary importance with respect to the wells was the availability of LAS files which provide for a wide range of analytical capability when incorporated into the modeling workflow. Ninety-four of the well control points had LAS files available and were either obtained from the respective state agency or acquired from the TGS-NOPEC Geophysical Company (TGS). Such files were used to provide quality control (QC) and correlate the basal saline system across this large area.

The basal saline system comprises several diachronous rock units of variable lithology: the Middle Cambrian Basal Sandstone in the Alberta Basin adjacent to the Late Cambrian Deadwood and Early Ordovician Black Island Formation in Saskatchewan, Manitoba, and the Dakotas. These strata are overlain by Upper Ordovician and Lower Silurian carbonates. The basal saline system is overlain by Cambrian shales in the Alberta Basin and by Ordovician shales or Middle Devonian tight shaley carbonates in the Williston Basin. The basal saline system reaches depths of more than 16,000 ft near the Rocky Mountain Thrust and Fold belt in the Alberta Basin, and nearly 16,000 ft at the depocenter of the Williston Basin. The rock sequence crops out and is a source of fresh groundwater in south-central to southeastern Manitoba (e.g., Ferguson and others, 2007) and in South Dakota and Montana (Figure 4).

The vast extent and thickness of the model contribute to the large effort to characterize the basal saline system because of changes in nomenclature and the sparse data available from the relative absence of oil and gas development compared to other stratigraphically oil-bearing zones in this region. The nomenclature for these alternating beds of fine siliciclastics and carbonates varies throughout the study area. In parts of Montana and Wyoming, they are referred to as the Gros Ventre and Gallatin Groups and are equivalent to parts of the Emerson Formation in the Little Rocky Mountains area of Montana and the Deadwood Formation in North and South Dakota. The Gros Ventre Group is made up of the Wolsey Shale, the Meagher Limestone, and the Park Shale. The Gallatin Group consists of the Pilgrim Limestone, the Snowy Range Formation (which consists of the Dry Creek Shale and the Sage Pebble Conglomerate), and the Grove Creek Limestone (which is sometimes included within the Snowy Range Formation) (Macke, 1993) (Figures 3 and 4).

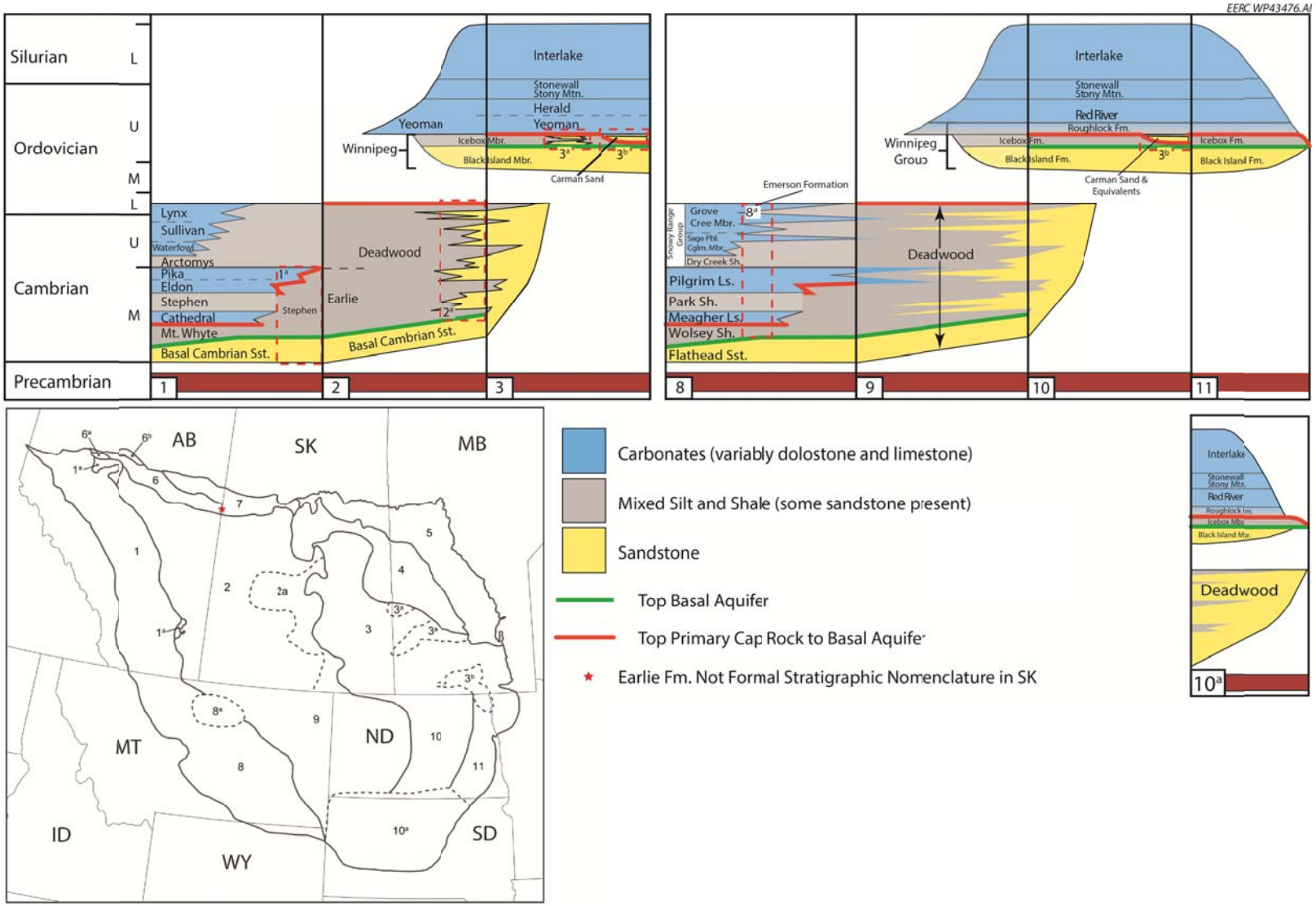

Figure 3. Stratigraphic correlation chart comparing the U.S. portion of the study region with the adjacent Canadian portion (modified from Bachu and others [2011]). The numbers on each stratigraphic column correlate to a region on the map. Nomenclature changes across the U.S.–Canadian border. Region 8a signifies a change in nomenclature, not lithology, in the Little Rocky Mountains area.

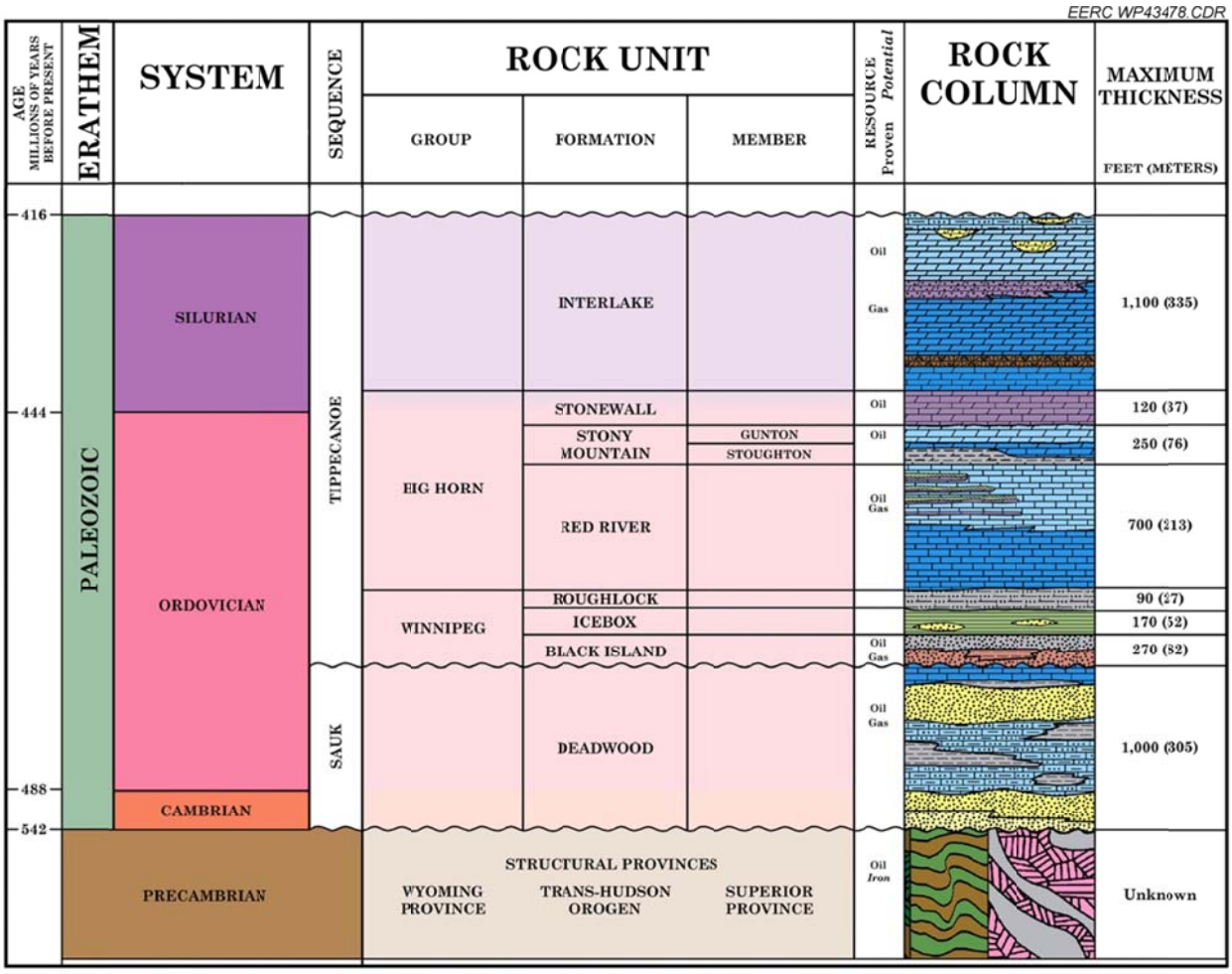

Figure 4. Stratigraphic column showing the early Paleozoic strata of the Williston Basin (modified from Murphy and others [2009]).

Formation tops of these stratigraphic sections were imported from state databases for Montana, North Dakota, and South Dakota, while tops in Canada were previously picked by Bachu and others (2011) in collaboration with our efforts. After import, the tops went through a QC process to adjust the aquifer top or Precambrian top if needed based on available digital well logs. A uniform aquifer top was established throughout the area to comprise the units described above prior to structural modeling.

Petrophysical Analysis

A petrophysical analysis was conducted to determine the reservoir's gross lithology and petrophysical characteristics. Determination of the basal saline system's lithology and effective porosity was determined from a multimineral petrophysical analysis (MMPA). The results went through QC and were calibrated to core-shifted data. Key wells with core data and appropriate logging suites were identified throughout the basil aquifer region to have such an analysis conducted.

Core Data Shift

Prior to the petrophysical analysis, core depths were usually incompatible with the depth of the logs, typically caused by the difference in driller and logger's depth. The depth mismatch resulted in the miscorrelation of the petrophysical results and the core laboratory data and made it impossible to compare results and give confidence in the results of the petrophysical model. However, core gamma log from lab analysis was available and allowed for the core to be depth-shifted to match the wireline gamma log. This adjusted the core data to be on the same depth scale as the wireline log. If core gamma log information was unavailable, core porosity measurements were shifted to match the calculated inversion porosity.

Identifying Key Wells

An MMPA was conducted on 61 wells with a quality log suite in Canada, North Dakota, South Dakota, and Montana for the basal saline system using the Quanti.Elan multicomponent inversion module in Schlumberger's Techlog 2011 (Figure 5). The wells cover a majority of the aquifer, important in calculating changes in the aquifer geostatistically to populate petrophysical properties. The desired log suite for the Quanti.Elan process includes gamma ray, bulk density, neutron porosity, sonic, deep and shallow resistivity and photoelectric factor logs. Additional desired data include routine core analysis data for QC and calibration of the petrophysical model. Additionally, 19 wells with quality log suites in the basal saline system had a routine core analysis performed in rock units of the system.

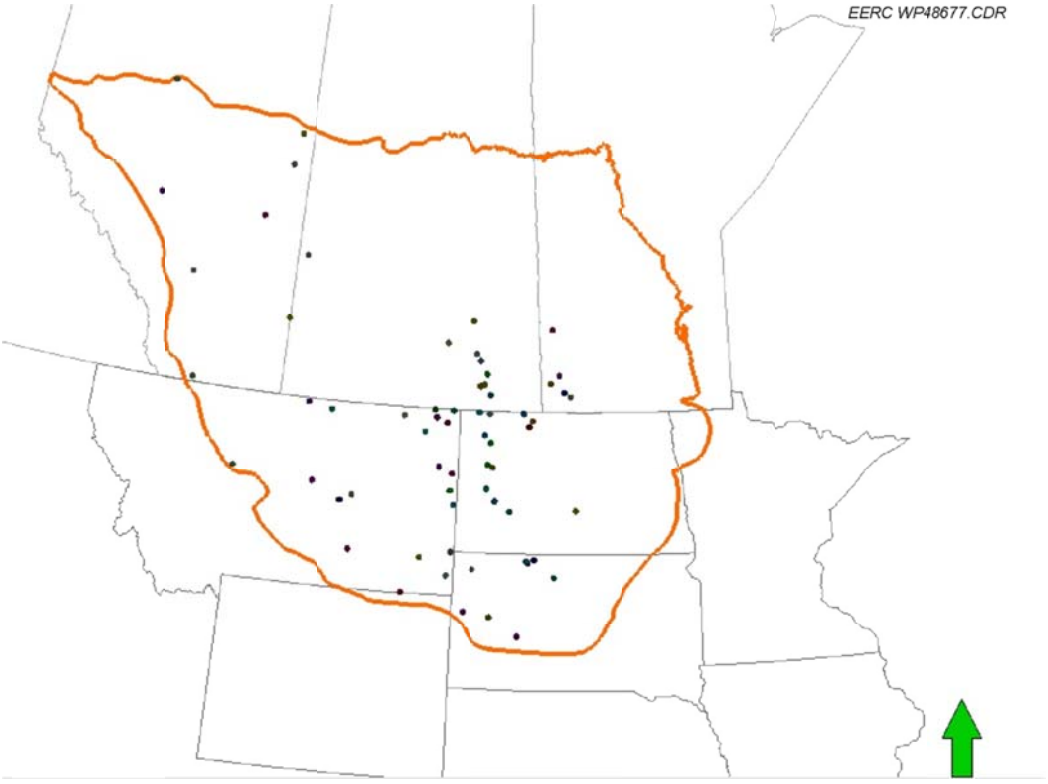

Figure 5. Map of well locations used for MMPA and core-calibrated MMPA.

Multimineral Petrophysical Analysis

An MMPA is typically conducted to determine the complexity of oil and gas reservoirs and the effects the overall mineral content has on fluid movement and production estimates. Mineral composition ultimately determines the rock's physical parameters which can be used as a tool to determine the overall characteristics of the reservoir and the depositional environment. The Quanti.Elan module calculates the overall volume of different mineral components in each wellbore. The mineral volume calculation aids in determining the stratigraphy and the overall correlation from one wellbore to another, thus describing the lithological stratigraphy for property distribution in the 3-D model.

The Quanti.Elan module uses sequential quadratic programming to solve nonlinear problems from log measurements and outputs the mineralogy of the formation being evaluated. Prior to inversion, to optimize the model and results, the geological environment was determined through core analysis and x-ray diffraction to predefine the system for the mineralogical components. This analysis helped populate the geologic 3-D model with lithology and corresponding petrophysical properties.

Mineralogical core samples evaluated in this study for the basal saline system range from clastic, well-sorted quartz sandstone to medium energy fossiliferous carbonates. Many samples from the petrographic analysis demonstrated secondary mineralization, mainly, dolomite and glauconite. Other mineral components reported in mud logs indicate traces of pyrite. The mineral assemblage of quartz, calcite, dolomite, glauconite, pyrite, and clays helped predefine the system prior to the inversion process. Because the model comprises such a large area, the changes in mineralogy for the basal saline system helped identify major zones comprising sand, carbonates, shale, and silty zones. Additional key properties calculated from the MMPA process include pore fluid volumes and effective and total porosities.

The primary QC mechanism for the results is the use of the reconstructed logs created by the inversion process. After inversion, the results went through a quality check process by crossplotting the reconstructed logs made by the inversion process with the geophysical wireline logs. Additionally, the results of the core porosity measured in the lab and the effective porosity calculated from the MMPA were crossplotted as a quality check (Figure 6). Changes to the mineral's property end points were adjusted accordingly until crossplotted results had an acceptable line of regression and approached a line of best fit. Once the inversion process was complete, each system underwent a quality check. Although reconstructed logs are the optimum mechanism for quality check, the user should have an understanding of the geologic environment. Other data may fit the model, which is why the system should be predefined from the analysis of core and/or x-ray diffraction.

Seen in Figure 7, the Quanti.Elan reconstructed logs are crossplotted with the measured wireline logs. Different zones are created in the log where results are not near the $y = x$ line. Mineral physical properties may be changed to achieve these results in areas not representative of the properties determined from the core calibration. Satisfactory quality check of the mineralogy and other petrophysical determinations occurs when the line of regression approaches a slope of one.

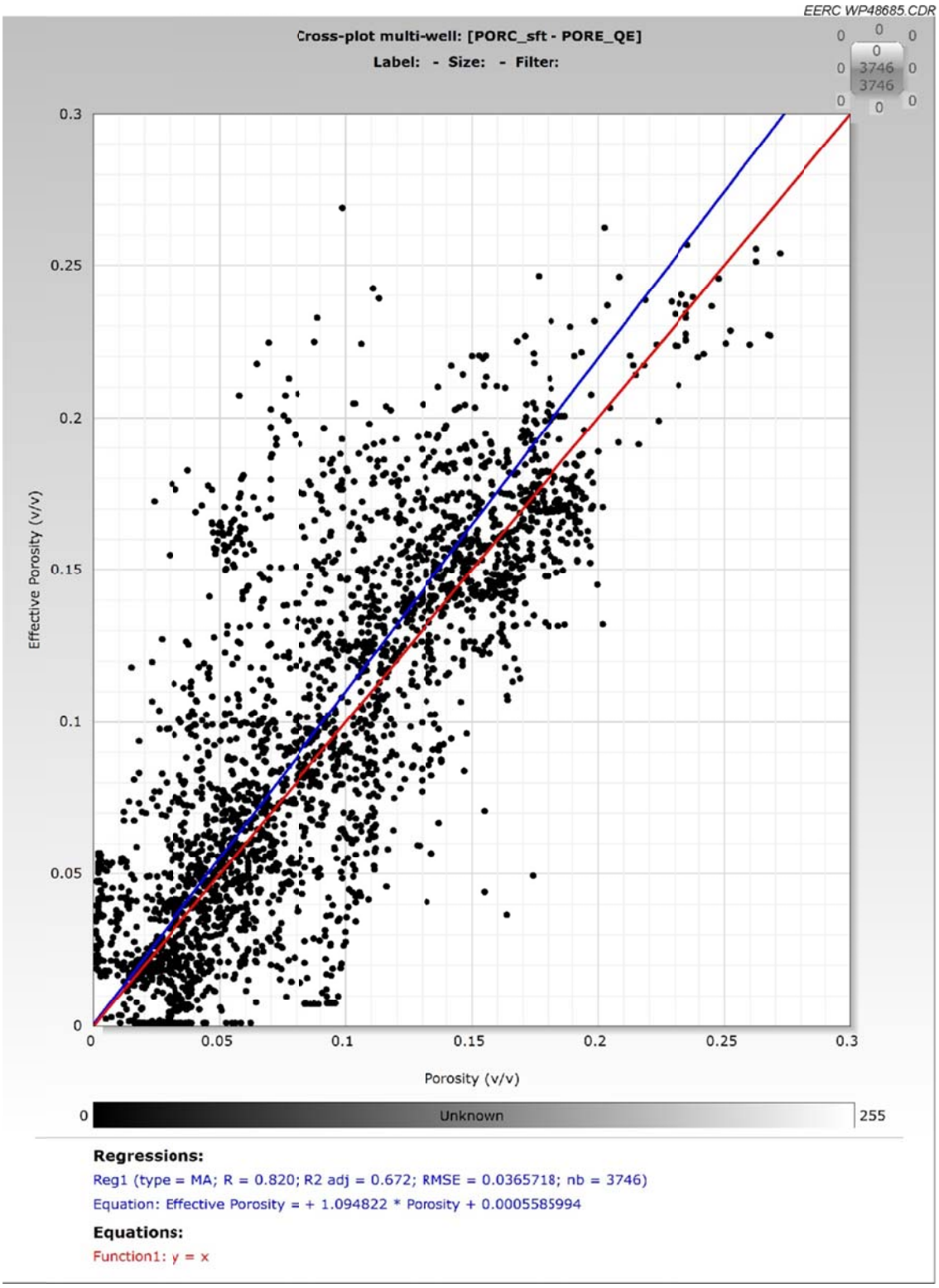

Figure 6. Crossplot of inversion porosity results and lab porosity results.

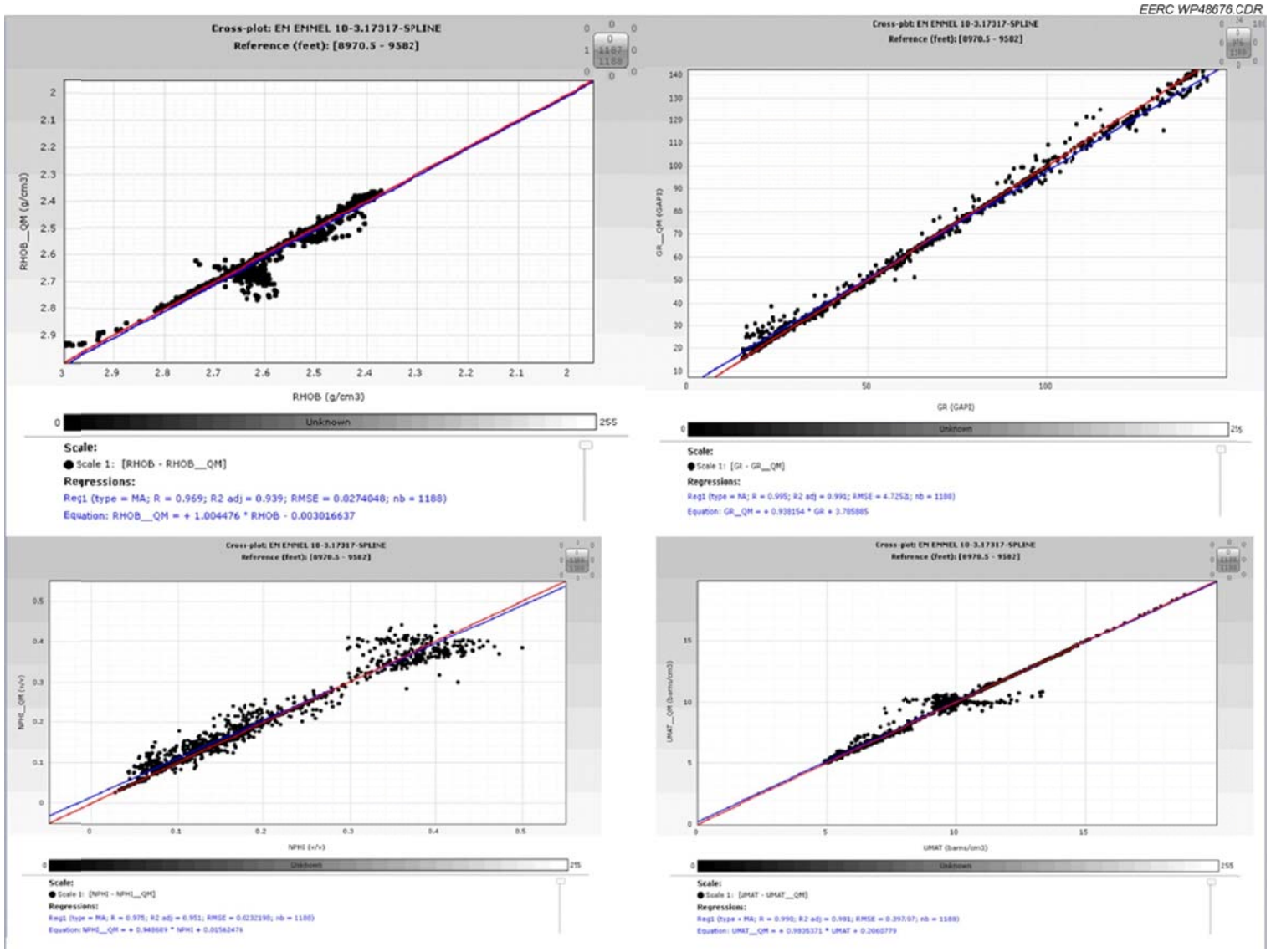

Figure 7. Quality check using crossplotted data of the wireline logs and the reconstructed logs from the inversion process. Crossplots are bulk density (upper left), gamma ray (upper right), neutron porosity (lower left), and volumetric photoelectric factor (lower right).

Results of the MMPA built the stratigraphy for each well comprising Black Island sandstone and alternating layers of carbonates, sandstones, and shale of the Deadwood Formation. Figure 8 shows the lithology for a well evaluated in North Dakota from the top to the base of the aquifer. Changes from one well to another can be vastly different because of the large aerial extent of this project and the distance between wells evaluated.

Structural Model

The structural model was built to capture the changes in thickness of the saline system and structural characteristics. Overall, the relief of the Precambrian basement and reactivation of various structures have affected thickness, porosity, and facies distribution of the basal saline system. Utilizing the tops picked from the stratigraphic analysis, structural surfaces of the basal saline system were built using a kriging approach using Schlumberger's Petrel.

Probably the most significant of the structural features affecting the deposited sediments of the basal saline system is the subsidence of the Williston Basin which occurred as early as the Late Cambrian to Early Ordovician and steadily continued to the Jurassic (Kent, 1987). Seen in Figure 9, the structural surfaces show the subsidence of the Williston and Alberta Basins reaching depths >12,000 ft below sea level. This subsidence has a large effect on notable characteristics of the basal saline system's reservoir properties.

Other notable structures affecting deposition include the Transcontinental Arch, a northeast-trending structure, and the Nesson Anticline, a north south trending structure. Both structures were Precambrian highs before transgression of the Cambrian Sea, causing the Deadwood Formation and Winnipeg Group to onlap these structures during deposition. However, sediments are thin or nonexistent on the structure because of postdepositional erosion. Many other structures within the study area did not form until after the Silurian and, therefore, did not significantly affect deposition of the Deadwood, Winnipeg, and their equivalent formations. However, many of these post (Cambro/Ordovician) depositional uplifts have become outcrop areas for Ordovician, Cambrian, and even Precambrian rocks. Many of these uplifts now act as recharge areas, such as the Central Montana uplift, the Black Hills, the Big Horn Mountains, the Little Rocky Mountains, and the Big Snowy Mountains. Others act as subsurface structural barriers between sedimentary basins. The Sweetgrass/Bow Island Arch separates the Williston Basin from the Alberta Basin, and the Miles City Arch separates the Williston Basin from the Powder River Basin.

The thickness of the basal saline system is highly variable. Sedimentation kept up with subsidence throughout deposition of the system, which is the main reason the thickest sections of most formations are located near the center of the basin (Figure 10). An isopach map was created from data produced from thickness points from wells that penetrated both the aquifer top and Precambrian basement. Because of the limitation of penetrating wells into the Precambrian, the isopach map and outcrop locations helped structurally control the base of the aquifer (i.e., top of the Precambrian).

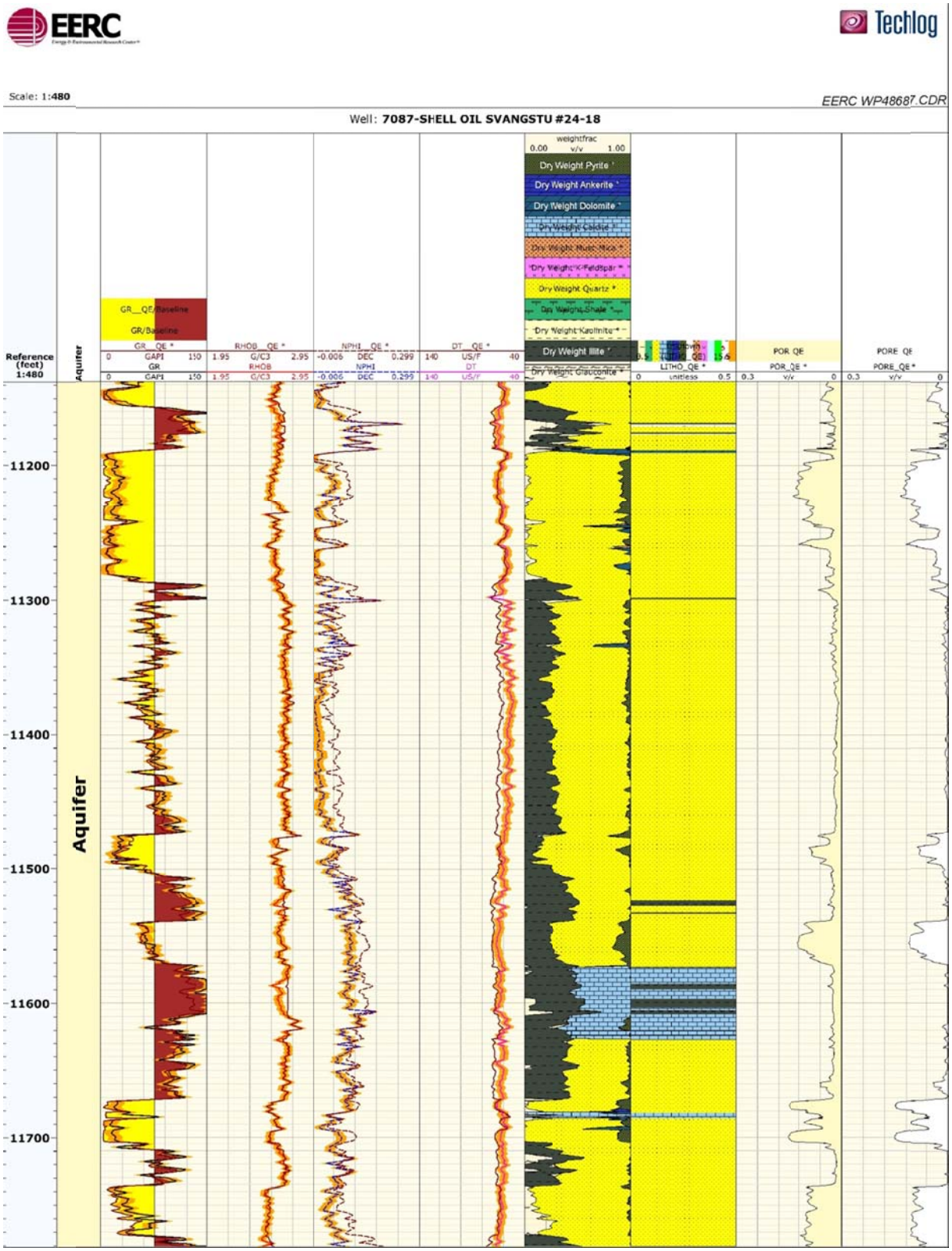

Figure 8. MMPA results using Techlog's Quanti.Elan module. Combinations of key minerals help determine the gross lithology and effective porosity.

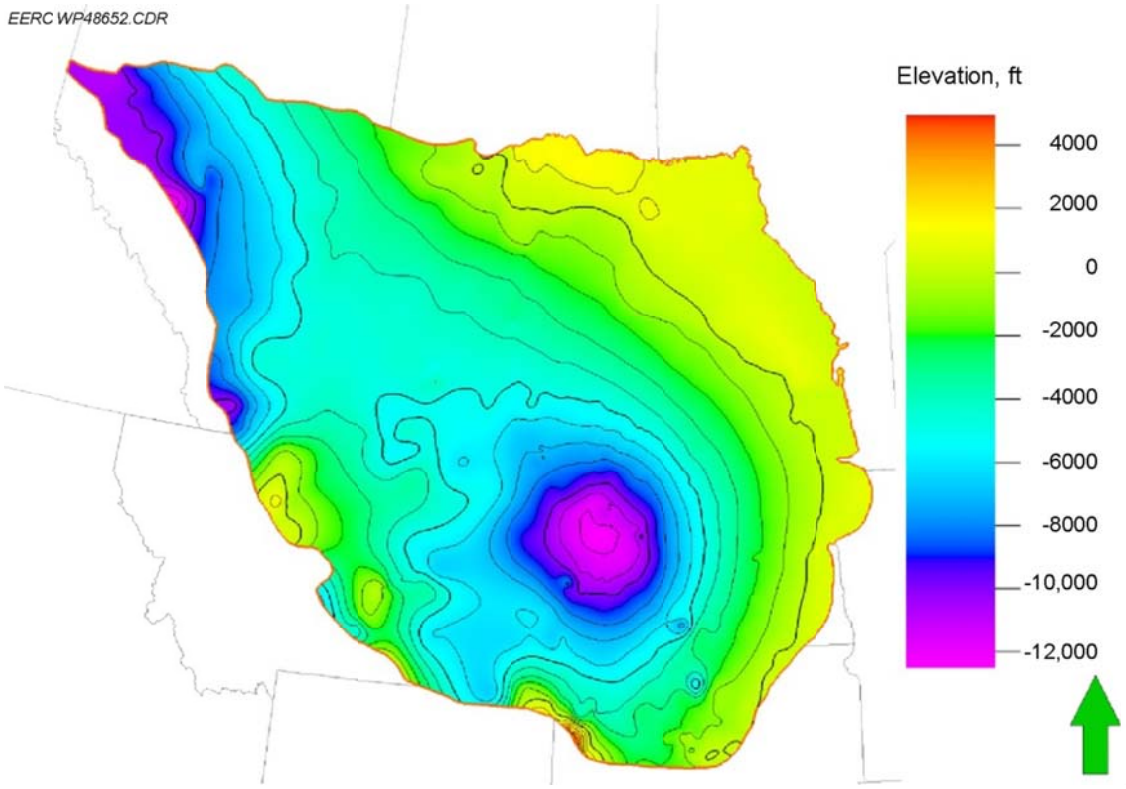

Figure 9. General structure of the basal saline system.

The vertical thickness of the system is greatest (>1000 ft) near the depocenter of the Williston Basin, overlain by shale of the Winnipeg Group, and in northeast Canada where the aquifer is unconfined to the surface. Areas of the aquifer that are thin include eastern portions of South Dakota and North Dakota. In this region, subaerial exposure occurred after deposition and eventual erosion of sediments occurred around the basin's edges.

The structural surfaces of the basal saline system top and the Precambrian were used to create a 3-D model with a 2250 × 2250-ft grid mesh. The model was then broken into five arbitrary zones, all of which were proportional, and broken down further into five proportional layers distributed for each zone. The zones and layers determined cell thickness and allowed for lithology and petrophysical properties to be distributed vertically, creating model heterogeneity.

Facies Model

A facies model was created to capture the heterogeneity of the basal saline system and delineate areas that are hydraulically connected. These Cambrian-aged strata are an extensive unit comprising coarse- to fine-grained quartzose and glauconitic sandstone that is locally conglomeratic at its base (Bell, 1970; Carlson and Thompson, 1987; Macke, 1993; LeFever, 1996). The depositional environments have been interpreted as marine foreshore to shoreface, tidal flat and, where conglomeratic, fluvial to alluvial (LeFever, 1996). This basal sandstone blankets the Precambrian basement throughout much of the northern Great Plains area and is a main component of potential CO_2 storage in the basal saline system.

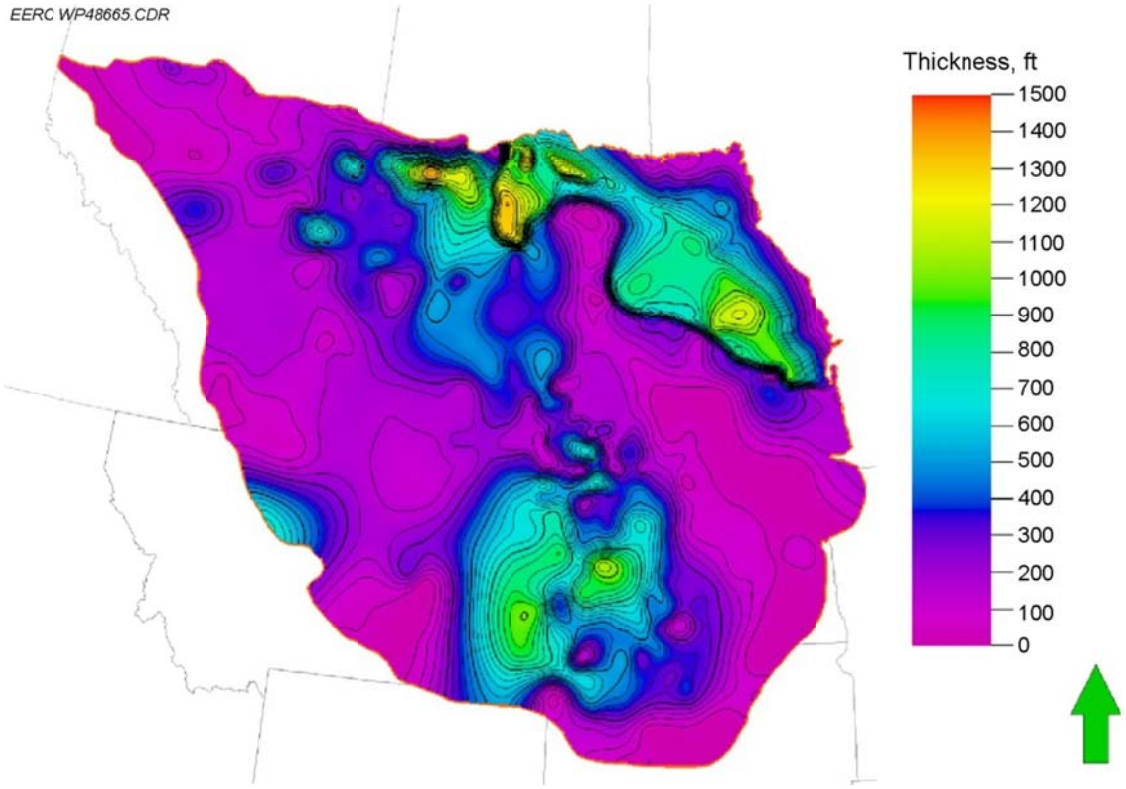

Figure 10. Isopach map of the basal saline system.

As the Cambrian Sea continued its eastward transgression, it began to deposit fine siliciclastics and eventually carbonates to the west, some of which extend into central North Dakota as part of the Deadwood Formation. This alternating sequence of fine siliciclastics and carbonates acts as a seal to the basal saline system throughout most of Montana, Alberta, and Saskatchewan. In eastern Montana, these formations begin to grade into the more clastic-rich Deadwood Formation. The lithology of the Deadwood varies greatly throughout North Dakota, eastern Montana, and northern South Dakota. Multiple layers of sand make good targets for potential CO_2 storage, whereas multiple layers of shale create many minor seals (baffles).

The Winnipeg Group consists of, in ascending order, the Black Island, Icebox, and Roughlock Formations. The Black Island Formation consists predominantly of sandstones with minor amounts of shale. It unconformably overlies the Deadwood Formation throughout eastern Montana and most of North Dakota, except in parts of eastern North Dakota where it lies nonconformably on the Precambrian basement. Deposition is interpreted as beginning in fluvial and deltaic environments and transitioning to a shallow marine environment as sea level continued to rise and transgress eastward (LeFever, 1996).The gross lithology was determined for each key well from the MMPA capturing the vertical and lateral heterogeneity mentioned above. The minerals were classified to their corresponding lithology and broken into the respective gross lithologies of shale, carbonate, sand, and silt (Figure 11). Further applying geostatistics helped map gross packages of these lithologies.

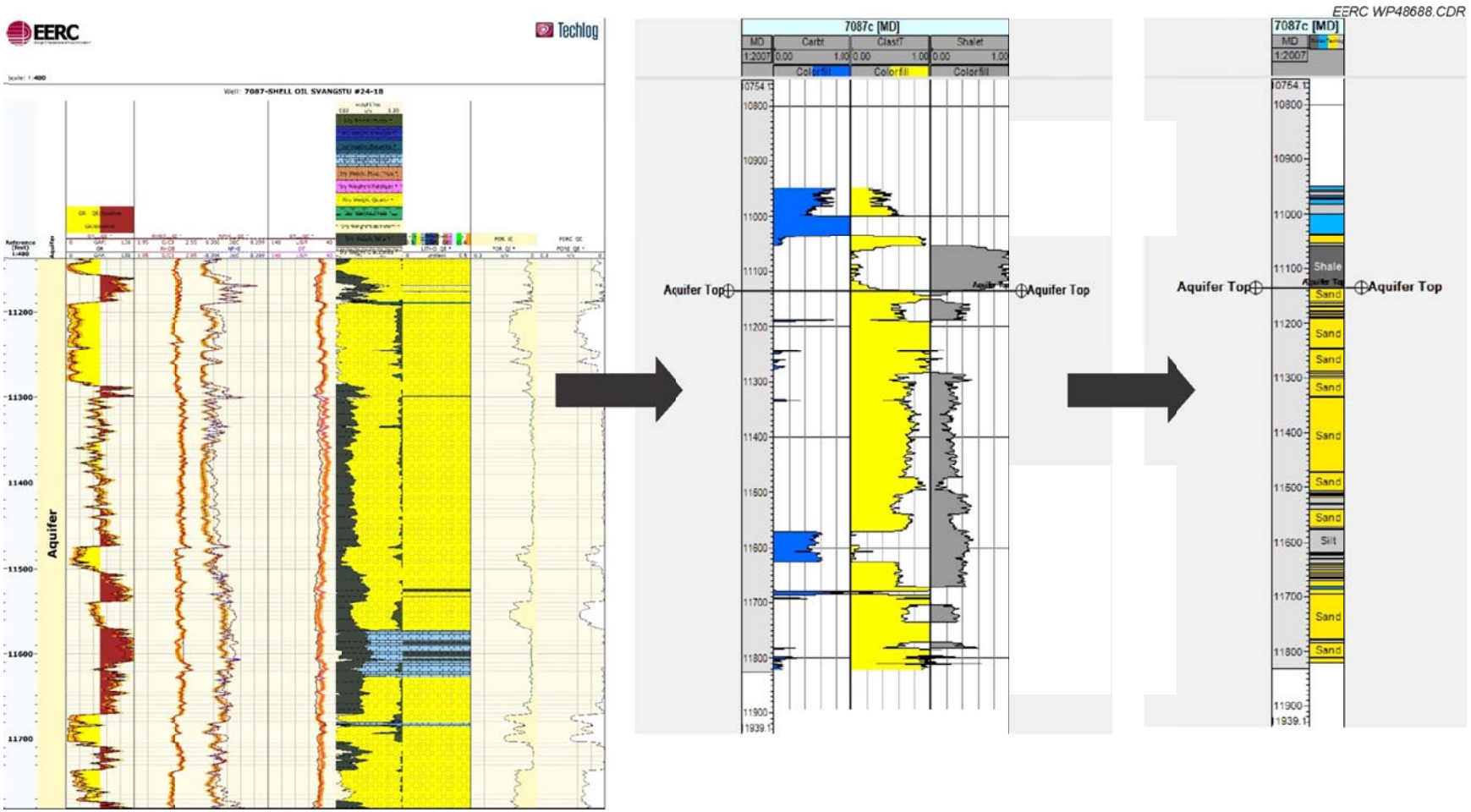

Figure 11. The minerals computed from the MMPA were classified into the respective gross lithologies of shale, carbonate, sand, and silt. The facies determination was then imported from Techlog into Petrel.

Because of the large area of the model, the 61 wells from the MMPA only represented a small portion of the study area (Figure 12). Lithology was calculated for an additional 180 wells based on the bulk density, gamma ray, and sonic wireline logs to acquire an improved data density for statistical analysis and reduce uncertainty. The lithology generated from the 61 MMPA wells helped serve as a baseline lithology log and was used to provide QC for the lithology log calculated from the wireline logs.

The resulting calculated lithology logs were populated throughout the model using the sequential indicator simulation method and variograms for each lithology from data analysis (Appendix A). Variograms in the model are large. Because of the well spacing in the model, they are much larger than those determined from a field-scale model. A variogram major and minor direction was determined, but the variograms in the minor direction are almost identical to the major direction, showing little anisotropy regionally.

Because of the large variograms and lack of well control, the lithology was further controlled based upon the work of Bachu and others (2011) which evaluated lithology of the basal saline system in Canada and found it to be primarily sandstone. To better align with the results of that research, a probability model was created to reduce the carbonate facies in the northern areas of Canada during simulation. The probability model gradationally reduces carbonates north of the U.S. border instead of a hard arbitrary cutoff.

Figure 13 of the facies model shows a map view of the top layer and the representative facies. The distribution of the facies is primarily sand (48%) with minor amounts of shale, silt, and carbonates in the geocellular model (Figure 14). Cross-sectional views east to west

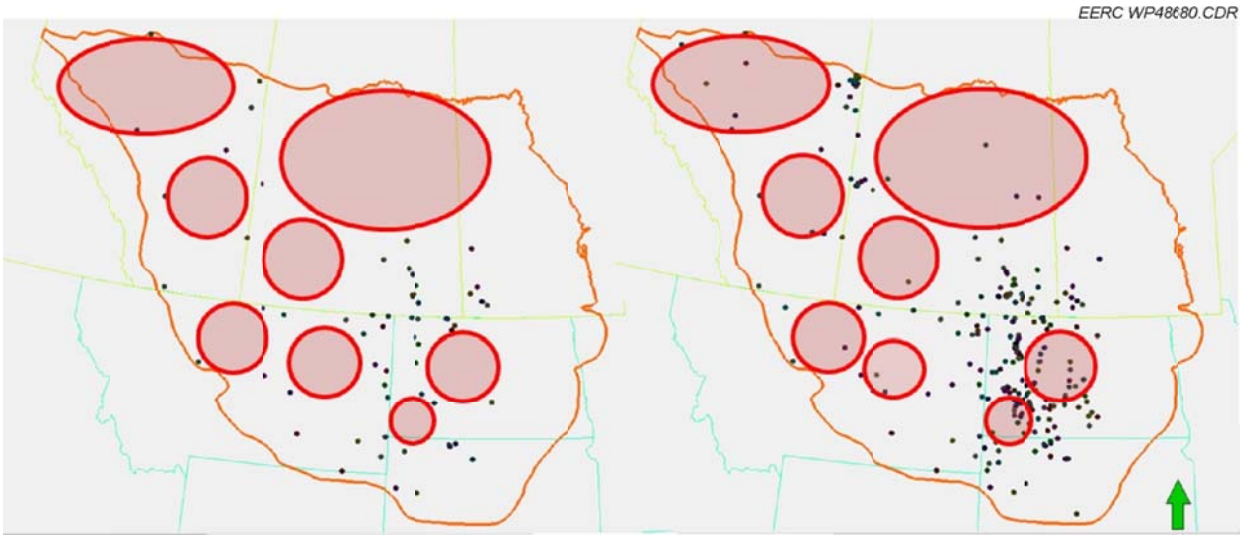

Figure 12. The 61 key wells from the MMPA only represented a small portion of the study area (left). An additional 180 wells had a facies log calculated from the bulk density, gamma ray, and sonic wireline logs to acquire an improved data density for statistical analysis and reduce uncertainty (right).

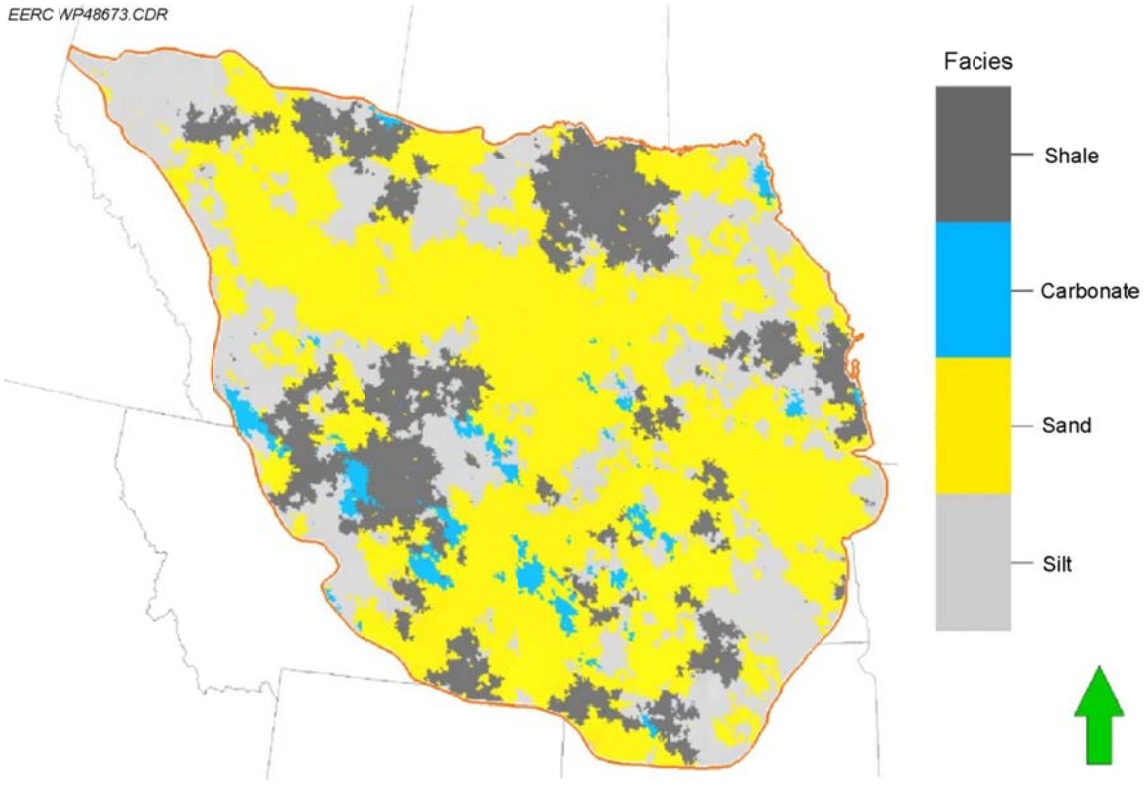

Figure 13. Top layer of the basal saline system displaying the facies property and its distribution.

(Figure 15) and north to south (Figure 16) display the distribution vertically and laterally of the interfingering layers of silt, sand, shale, and carbonate rock throughout the different zones and layers of the model. The resulting facies model is important when distributing the porosity and permeability and their relationship to facies.

Reservoir Properties

Reservoir properties distributed into the geologic model include porosity, permeability, water saturation, temperature, pressure, rock compressibility, and salinity. Petrophysical methods from the MMPA derived the total and effective porosities and fluid saturations. These properties were then distributed by different simulation techniques in Schlumberger's Petrel, a 3-D geostatistical modeling software, after a data analysis was performed to determine variogram range and orientation. Furthermore, to distribute the properties accurately, porosity and facies relationships and permeability and porosity relationships were distributed accordingly using univariate and bivariate statistics.

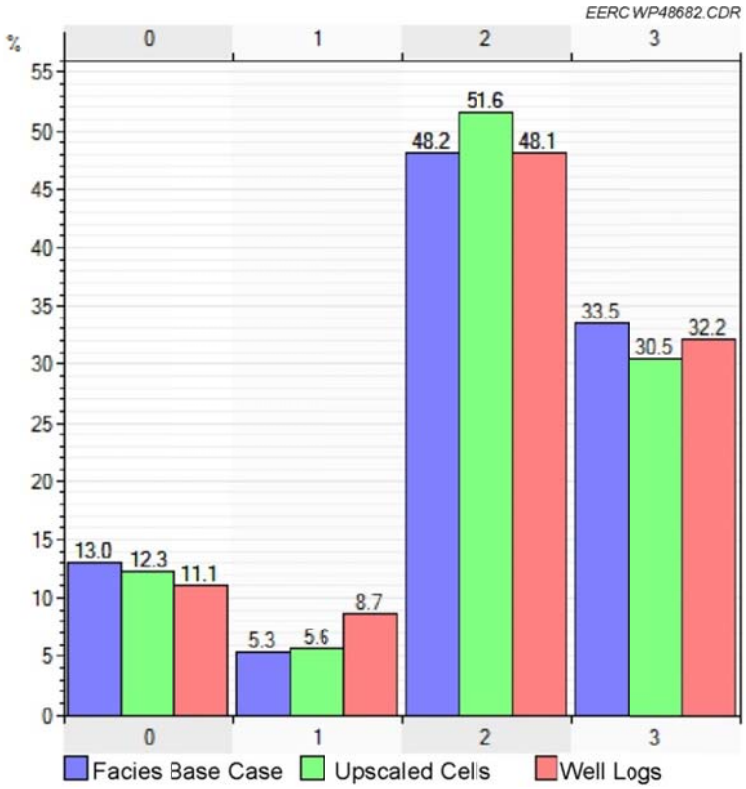

Figure 14. Histogram of facies (shale, carbonate, sand, and silt are 0, 1, 2, and 3, respectively).

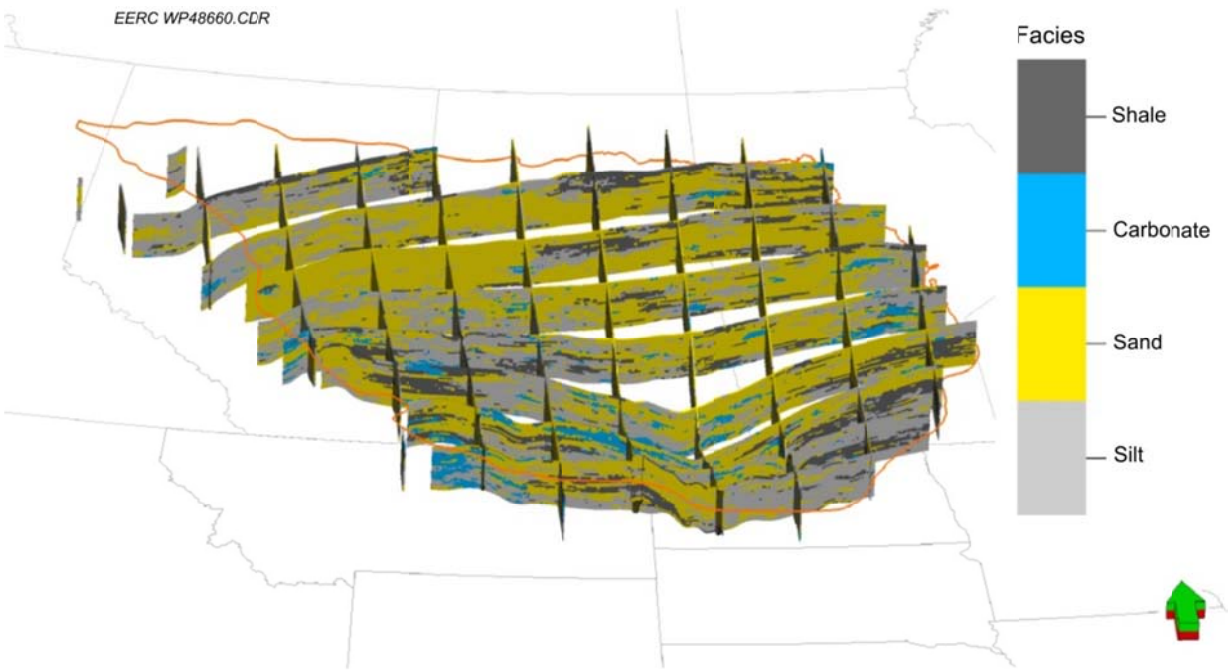

Figure 15. Cross-sectional fence diagram of the facies distribution from east to west.

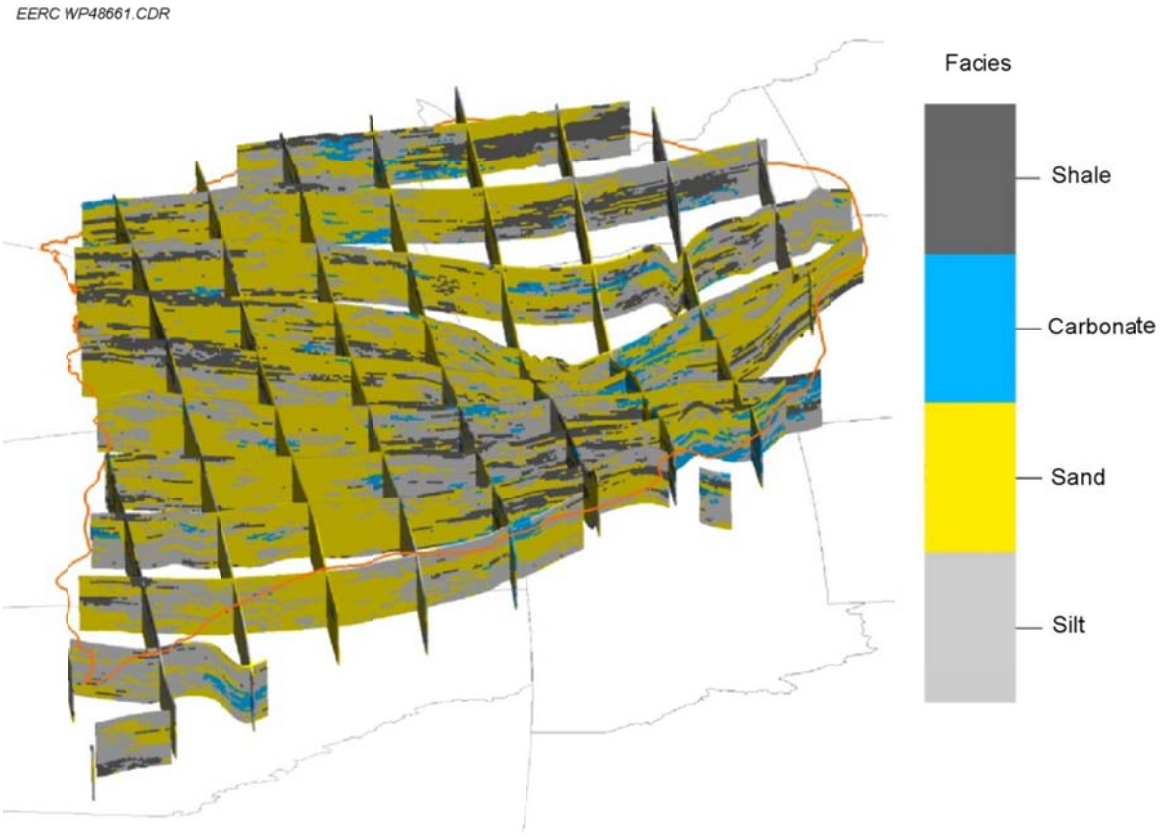

Figure 16. Cross-sectional fence diagram of the facies distribution from north to south.

Porosity

Porosity was determined petrophysically for 61 wells from the MMPA. The MMPA calculates total porosity and effective porosity based on computations of the fluid volumes and mineral volumes. The resulting porosity curves calculated from the logs are then compared to core data (if available). Crossplots of the core and porosity log help provide QC for the mineral output and the resulting porosity curves as described previously.

The results of the porosity data were populated into the 3-D model using the Gaussian random function simulation method and conditioning the porosity to the facies it represented (Figure 17). The variograms and histogram statistics control the distribution for each facies determined from data analysis (Appendix A). Porosity statistics can be found for each facies in Appendix A. Overall, the effective porosity for the varying lithologies and depths is log normal for the basal saline system (Figure 18).

Within the model, the porosity tends to be highest within the sandstone which can be seen in the cross-sectional views in relation to the facies model (Figures 19 and 20). Highest porosity occurs in the northern portion of the Williston Basin, where depths of the aquifer in this area are shallower and tend to be high for each of the 25 layers in the model. This high-porosity area

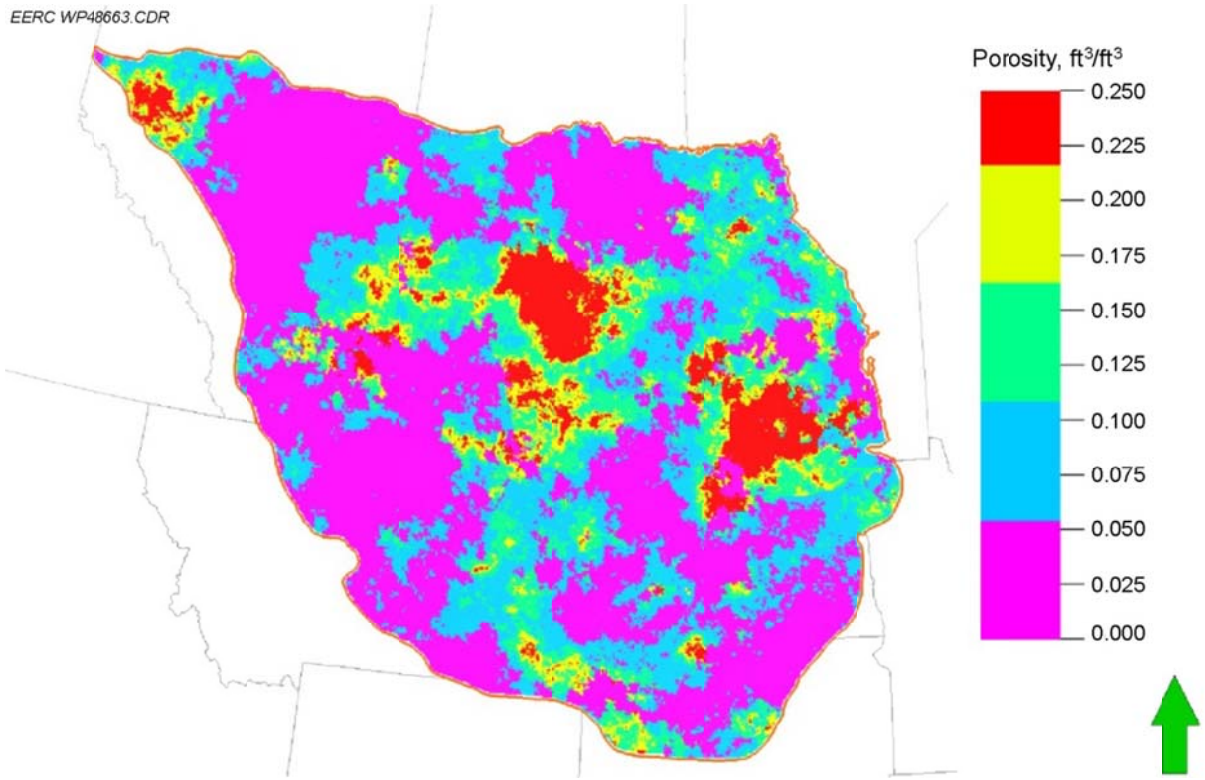

Figure 17. Top layer of the basal saline system displaying the distribution of the porosity property.

resembles similar porosity trends determined by Bachu and others (2011) of the basal saline system. Deeper parts of the basal saline system tend to have lower porosity even in areas where sandstone is present and could be the result of the confining pressure of the rock column.

Permeability

Permeability in the model was distributed for the sand and silt facies using a bivariate cloud distribution of the porosity and permeability relationship found in the core data. The permeability core values are properly depth-shifted according to the methods described previously using core gamma or core porosity data. Depth-shifted core permeability data give confidence that the data are properly shifted to the correct depth and lithology type they represent determined from the MMPA. Because of the small interval the permeability core data cover for each well, Petrel's neural network process created a permeability log for the entire wellbore and for the rest of the MMPA wells that had no core data. The neural network module uses an algorithm to create an estimation model that compares logs and resulting mineral outputs from the MMPA wells to the core permeability data. The resulting estimation model created a permeability model that responds similar to the petrophysical logs and mineral outputs where core permeability data were not collected. After the data go through QC, the resulting synthetic logs were used to distribute permeability laterally and vertically using a cloud transform throughout the model and conditioned to each facies it represented.

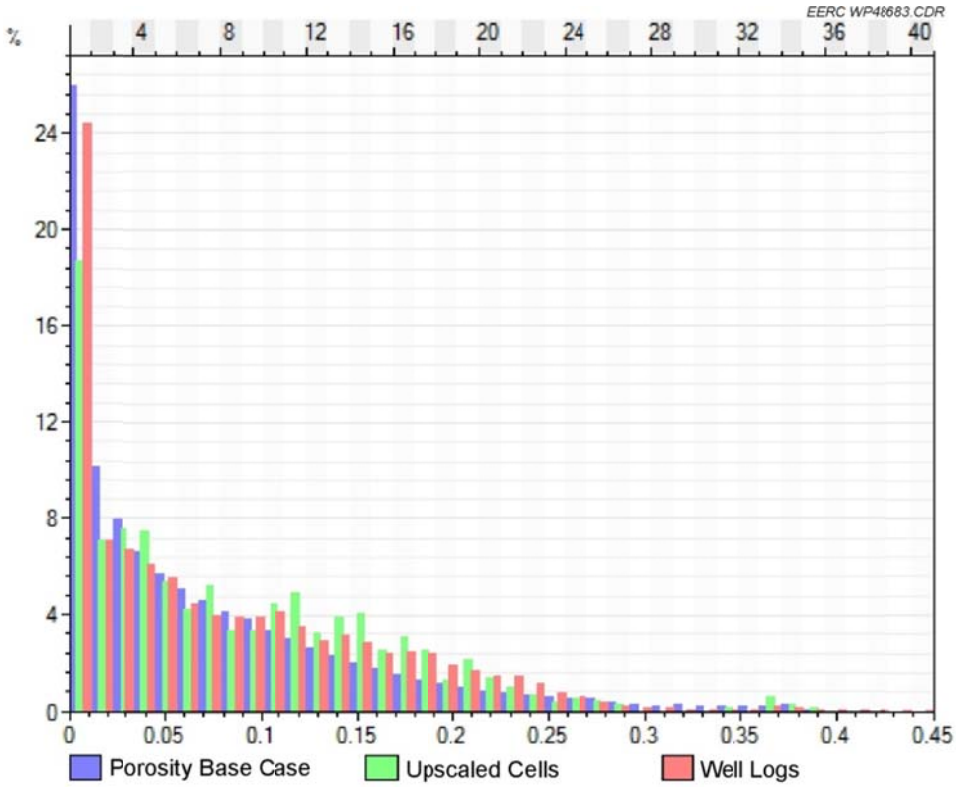

Figure 18. Histogram of the porosity property and distribution in the model.

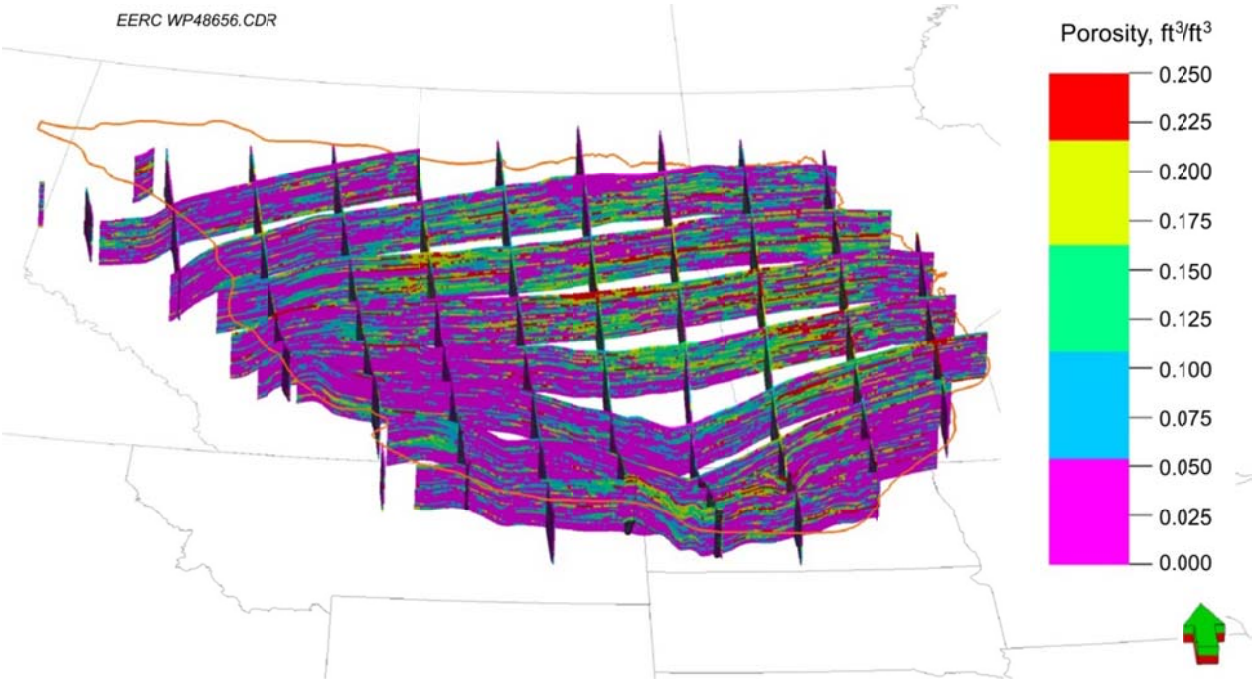

Figure 19. Cross-sectional fence diagram of the porosity distribution from east to west.

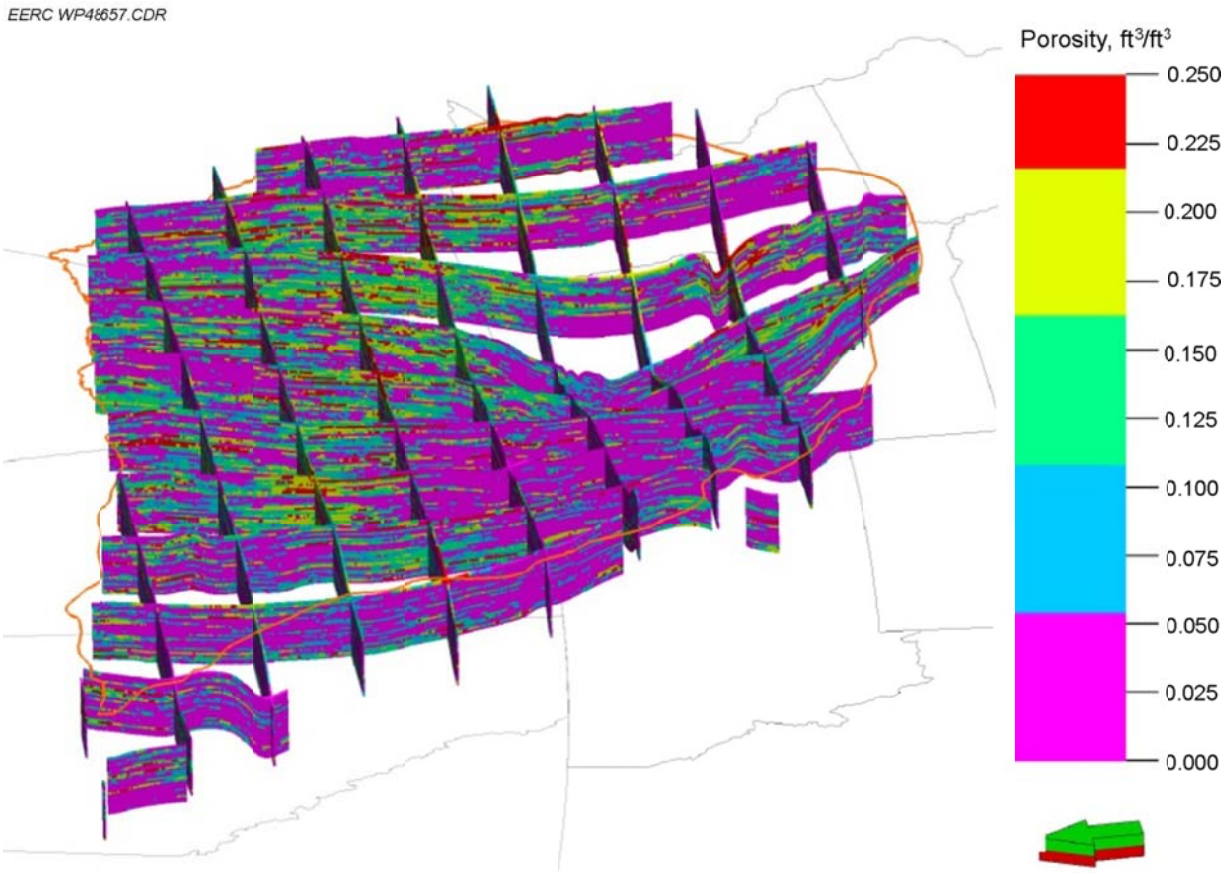

Figure 20. Cross-sectional fence diagram of the porosity distribution from north to south.

Because of the general relationship of permeability and porosity, core porosity and permeability data were plotted against each other to create a crossplot for the silt and sand lithology to honor the porosity–permeability relationship during simulation (Figure 21). Simulation utilizes the histogram (Figure 22) and the crossplot to populate the model using the bivariate distribution method. Statistics were used to populate the remaining facies because no general porosity–permeability relationship was apparent from the core data.

Figure 23 shows the overall distribution for permeability in the model. Permeability is highest in the sands, with measurements ~4000 mD measured in the core. However some of these higher numbers were reduced during the upscaling process of the logs. Overall, the property follows a similar trend in comparison to the porosity and facies properties seen in the cross sections (Figures 24 and 25) Permeability distributions for each facies are found in Appendix A.

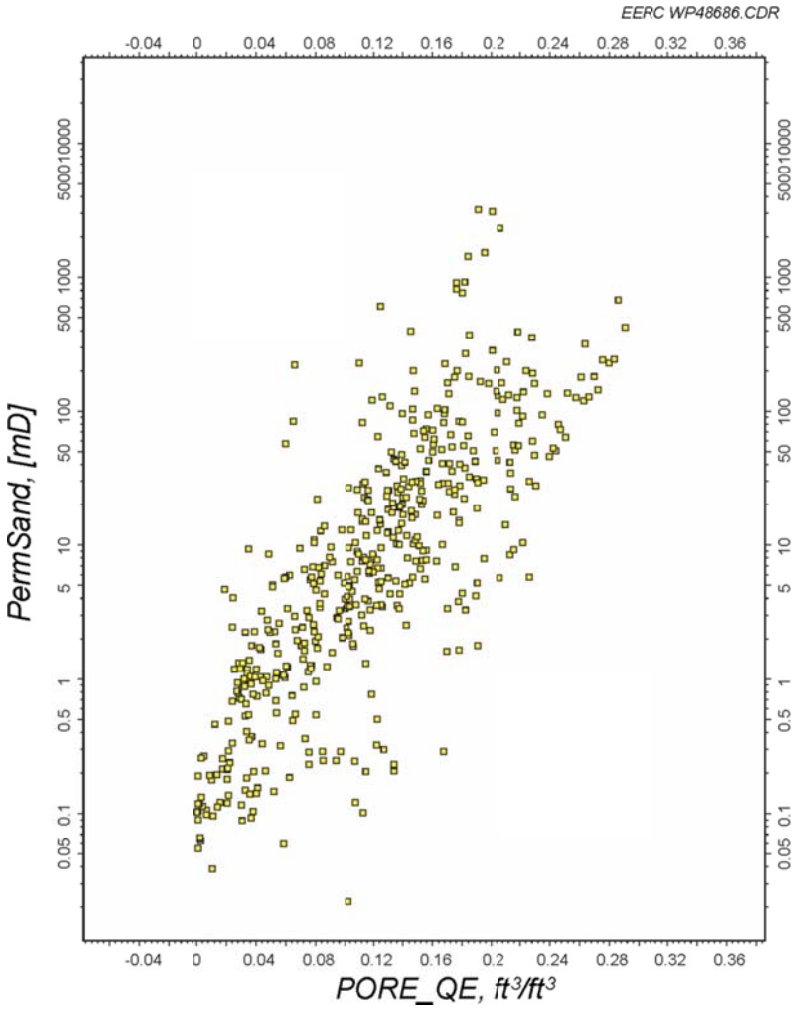

Figure 21. Porosity and permeability crossplot of the core data in the sand for the basal saline system. This crossplot is used as an input to distribute permeability in the model.

Temperature

Temperature in the model is a necessary variable to calculate CO_2 density at reservoir conditions. Temperatures in the model were determined from bottomhole temperature (BHT) and drillstem test (DST) measurements. Furthermore, the thermal regime changes over the basin affecting CO_2 density.

The process for a well to come to thermal equilibrium can require a long period of time because of mud circulation and well production. Temperature measurements made from wells in equilibrium are ideal to accurately determine rock formation temperature. However, they are rare. To account for fluid circulation affecting BHT measurements made shortly after drilling, a correction must be applied to accurately estimate the formation temperature.

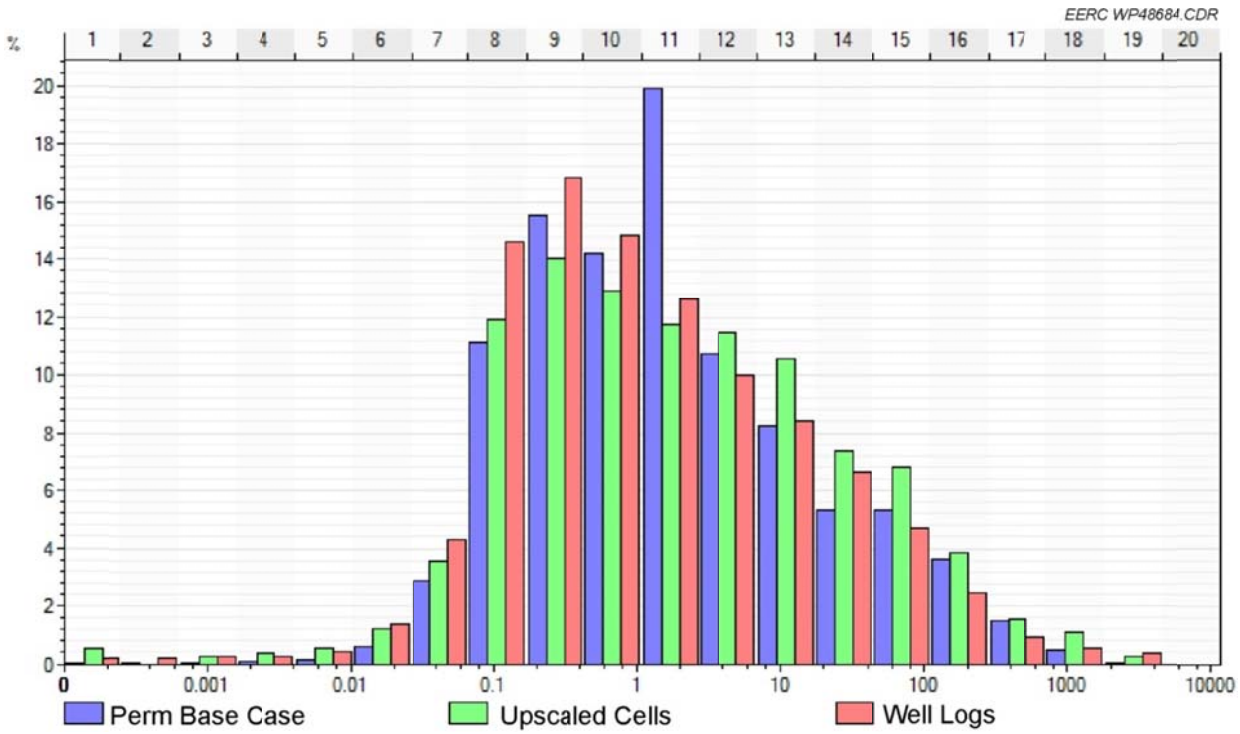

Figure 22. Histogram of the permeability and its distribution in the model.

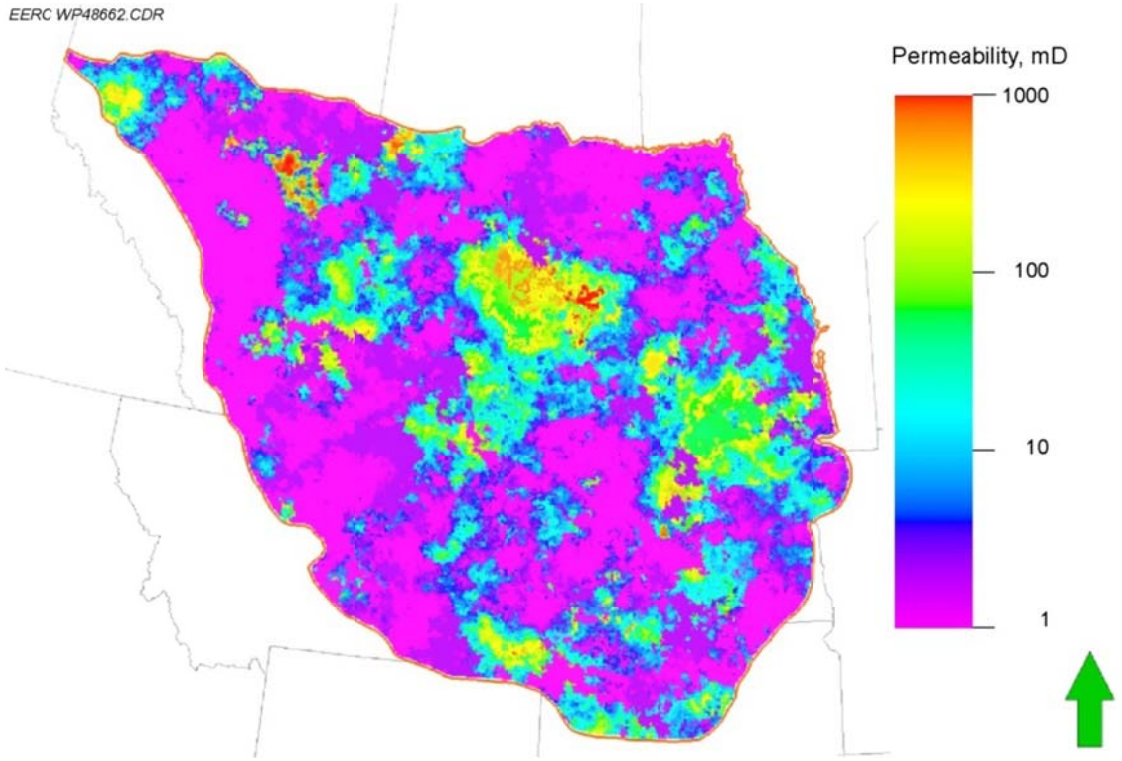

Figure 23. Top layer of the basal saline system displaying the permeability property and its distribution.

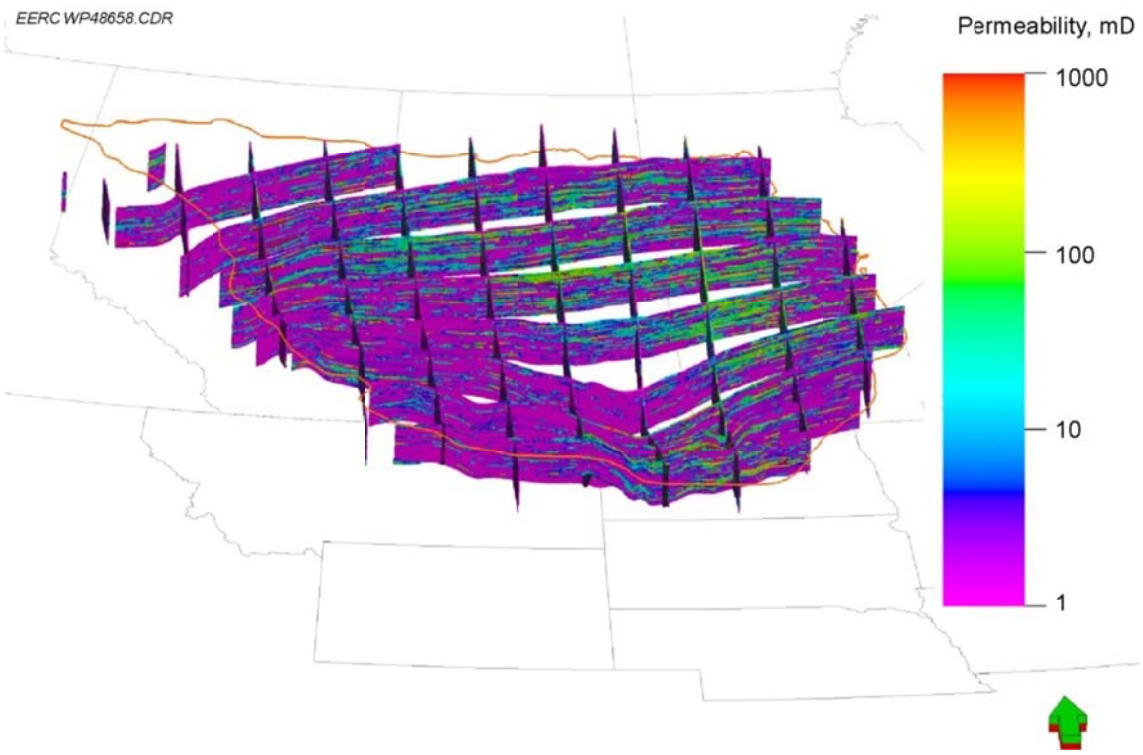

Figure 24. Cross-sectional fence diagram of the permeability distribution from east to west.

Harrison and others (1983) proposed a depth-dependent correction to BHT measurements to represent in situ temperatures calibrated from the Anadarko and Arkoma Basins. This correction works best for depths <9840 feet. Depths >12,900 feet increase slightly by 0.05°F every 500 feet from the corrected maximum (Blackwell and others, 2010).

$$\Delta°C = -16.51213476 + 0.01826842109\ z - 0.000002344936959\ z^2 \qquad \text{[Eq. 1]}$$

Where z = depth in meters.

Blackwell and others (2010) compared corrected BHT data to thermal equilibrium temperature profiles in Texas and found the data falling tightly around logged equilibrium measurements. Other correction techniques exist and were investigated, but circulation times and multiple BHT measurements in the basal saline system were rarely given and/or taken to correct for the BHT measurements. The Harrison correction is notably used by Blackwell and Richards (2004) for the Geothermal Map of North America and by Crowell and Gosnold (2011) for geothermal resource assessments of the Williston Basin.

The geothermal gradient was calculated to determine temperature changes from the top to the base of the basal saline system which overall affect the density of CO_2. The average equilibrium gradient to the top of the basal saline system is calculated as:

$$\frac{\Delta t}{\Delta z} = \frac{T_{BHT} - T_S}{z} \qquad \text{[Eq. 2]}$$

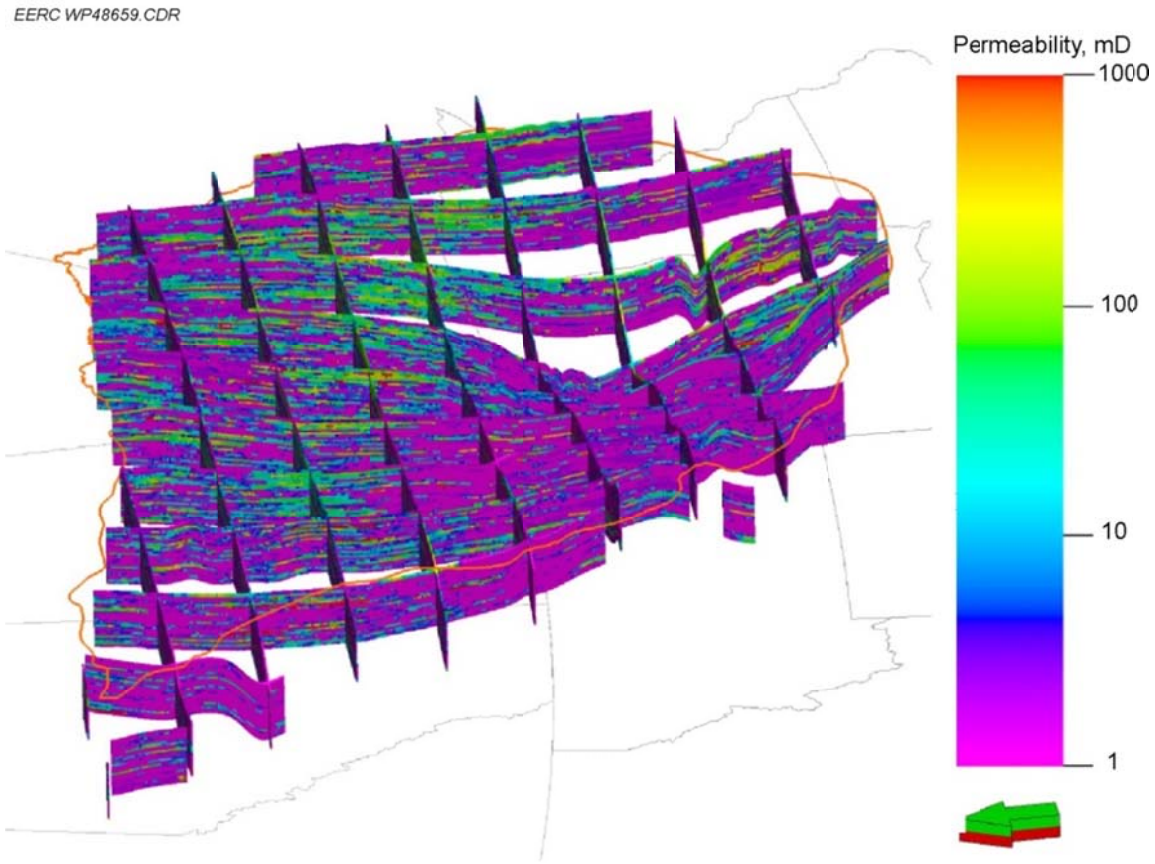

Figure 25. Cross-sectional fence diagram of the permeability distribution from north to south.

Where T_{BHT} is the corrected temperature, T_s is the average annual surface temperature (both in °C) and z is the true vertical depth of the log measurement in meters. Although an average gradient is useful to predict temperatures to the top of the basal saline system, the geothermal gradient in the crust varies from changes in thermal conductivity stratigraphically and does not represent the true gradient throughout the basal saline system.

The geothermal gradient was determined from the Southern Methodist University Heat Flow database and heat flow calculated from the AAPG (American Association of Petroleum Geologists) Geothermal Survey Data BHT database. Heat flow data and thermal conductivity were used to understand changes in the gradient laterally for the basal saline system. Fourier's law defines heat flow as:

$$Q = \lambda(\frac{\Delta t}{\Delta z}) \qquad \text{[Eq. 3]}$$

Where gradient is in °C/km, $\boldsymbol{\lambda}$ is thermal conductivity given in W/(m*K), and heat flow Q is in mW/m^2. To apply the heat flow equation, thermal conductivity must be determined for the stratigraphic column.

Thermal conductivity measurements were made by Gosnold and others (2010) from core representing different stratigraphic intervals in the Williston Basin of North Dakota. Utilizing a unit thickness and thermal conductivity from Gosnold and others (2010), the stratigraphic thermal conductivity for the BHT location is calculated:

$$\lambda = \frac{z_T}{\Sigma R} \qquad \text{[Eq. 4]}$$

Where ΣR is the sum of the total thermal resistance and z_T is the total well depth.

The gradient calculated from the BHT measurements and thermal conductivity is then utilized in Equation 3 to determine heat flow for the well. A value of 3.3 W m^{-1} K^{-1} measured by Gosnold and others (2010) for the Deadwood Formation is used to determine the geothermal gradient in areas of varying heat flow. Thus temperature gradients result between 0.007°F/ft in low heat flow areas to 0.016°F/ft in high heat flow areas. An average gradient of 0.10°F/ft was used in the model to propagate temperatures throughout the basal saline system.

BHT measurements prove a reliable temperature indicator for true formation temperature when corrected for mud circulation using the Harrison correction. Because of increasing temperature with depth, temperatures are highest, >350°F, in the depocenter of the Williston Basin, where depths are >12,000 ft to the top of the basal saline system and lowest, <85°F, at the margins where depths are 2500 ft (Figure 26).

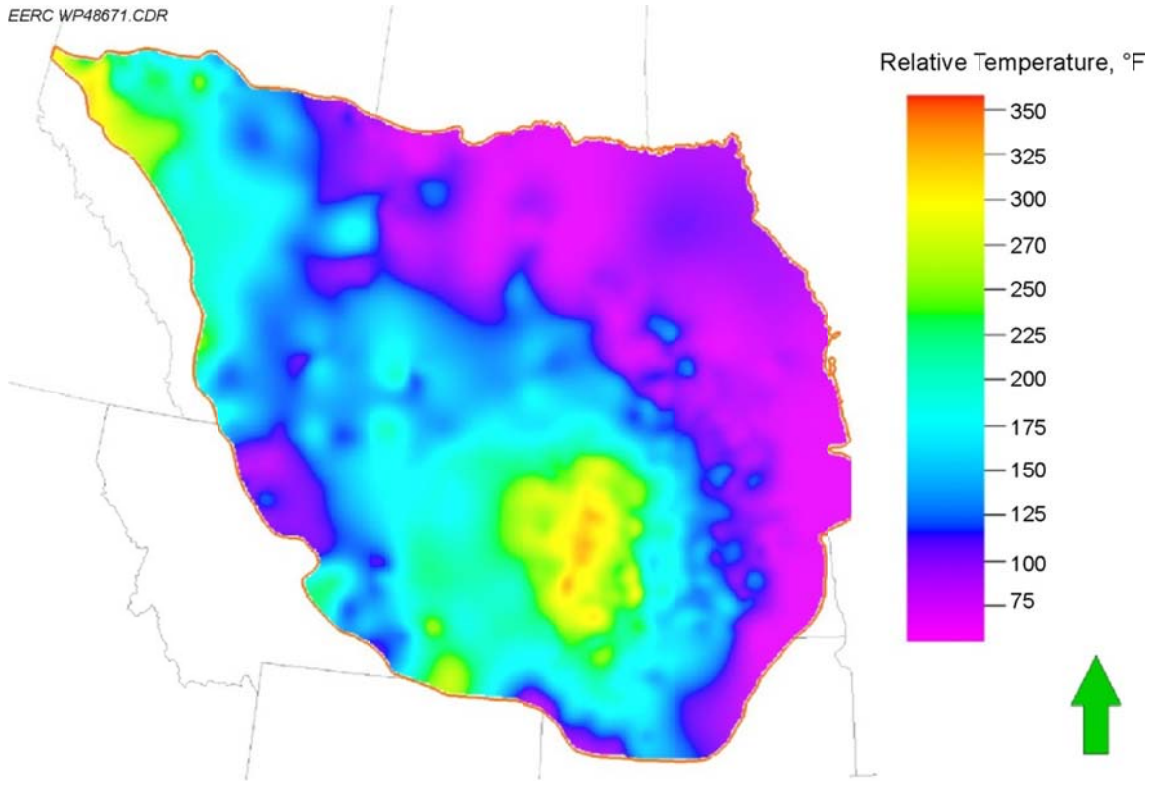

Figure 26. Temperature (°F) of the basal saline system from corrected BHT measurements.

Pressure

CO_2 density is a function of both temperature and pressure. Modeling the pressure regime and temperature regime will allow for CO_2 density to be modeled based on various changes to both properties throughout the saline system. Pressure determinations of the system are based on DST measurements.

Generally, the basal saline system pressure follows a similar trend to increases in depth (Figure 27). Pressure measurements that were analyzed by Bachu and others (2011) were used to populate the geocellular model. Bachu and others (2011) analyzed the quality of the data and screened the data using automated or manual techniques based on the DST's depth interval, flow and shut-in times, quality codes and factors, and the manual inspection of comments and charts of the DST.

The data were then contoured and constrained to allow for realistic results and for pressures to remain positive. A pressure gradient of 0.47 psi/ft calculated by Bachu and others (2011) was used to populate the model from the top of the saline system to the base.

Water Saturation

Water saturation was originally calculated in Techlog with the MMPA. Because of the complexity of the reservoir spatially, and the lack of well control in the model, a water saturation

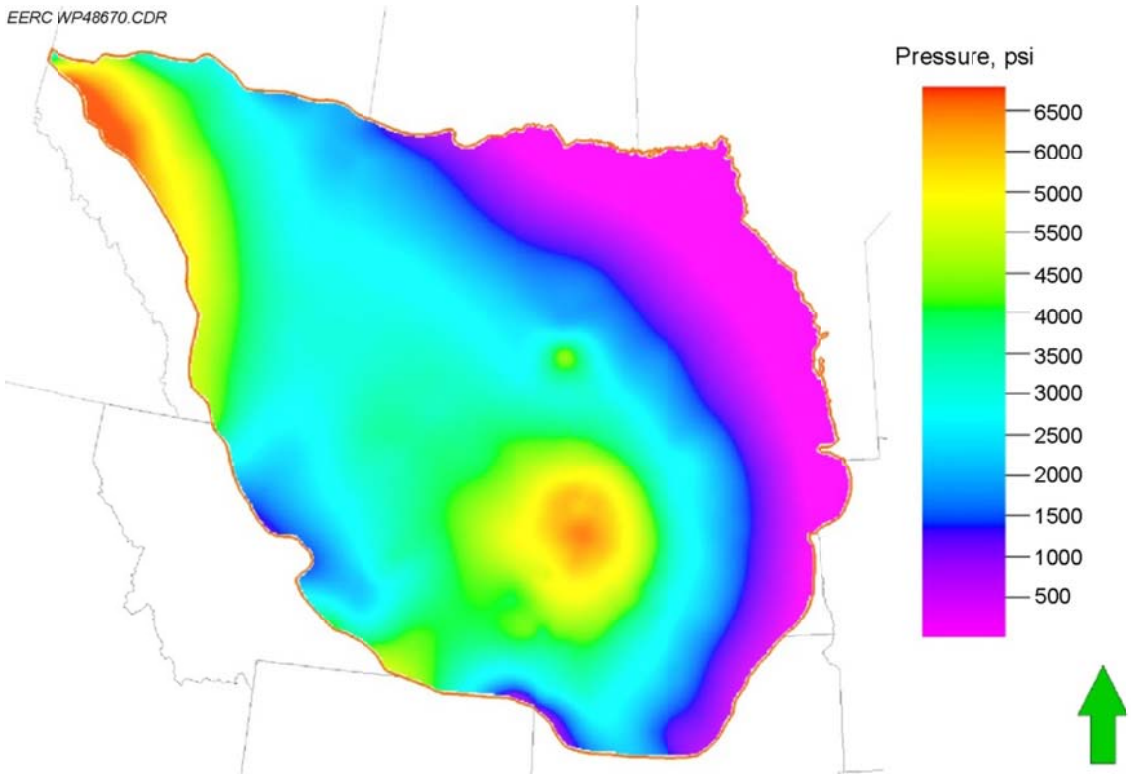

Figure 27. Pressure (psi) of the basal saline system from DST measurements.

of 1 was populated throughout the model, resulting in the absence of oil and gas. Although oil and gas are present in the reservoir, determining exactly how they are distributed in the model is a challenge. Because this model is a basin-scale model and not a reservoir-scale model, the large distance between wells delivers high uncertainty in determining the distribution of oil and gas in areas away from the wellbore.

Water Salinity

The formation waters in these saline systems range widely with respect to total dissolved solids (TDS). In the central portion of the Williston Basin, TDS levels reach nearly 350,000 ppm for the COSS (Downey and Dinwiddie, 1988). These levels taper off toward the basin margins where TDS levels are in the 5000–10,000-ppm range. The lower TDS values reflect the impact of freshwater recharge on water quality. The U.S. Environmental Protection Agency (EPA) defines potable water as having TDS levels less than 3000 ppm and underground sources of drinking water as having less than 10,000 ppm (U.S. Environmental Protection Agency, 2012). EPA definitions classify a large portion of the waters in the northern Great Plains aquifer system and, in particular, the COSS as not being underground sources of drinking water.

Water salinity in the model was determined from measurements and salinity determinations by Bachu and others (2011). The purple boundary in Figure 28 represents the 10,000 TDS line where in this area water is termed to be freshwater and injection cannot occur because of the water's use for agriculture, industry, or residential. Generally salinity increases with depth of the basal saline system where salinity varies from ~500 to ~350,000 ppm between the aquifer outcrop areas and in the deep areas of the Williston and Alberta Basins. In areas where this trend does not exist, the basal saline system water may be near recharge areas or is mixing from communication with overlying saline systems (Bachu and others, 2011).

CO_2 Storage Potential

CO_2 Storage Classification

The classification of CO_2 storage and the terminology that has evolved are intended to provide a comparable basis for assessing CO_2 storage potential from regulatory and business perspectives. The definitions of the terms are meant to convey varying degrees of confidence in the storage assessment values that are generated.

A hierarchy of classification terminology has been developed over the past 5 years that leverages increasing confidence with increasing data and a smaller geographic area of interest. These relationships were first illustrated by the techno-economic resource–reserve pyramid defined by the Carbon Sequestration Leadership Forum (CSLF) (2007). This graphical representation of terms shows the trend from broad-based resource estimations to small-scale, site-specific characterizations (Figure 29), each with differing degrees of certainty. Moving up the pyramid requires more detailed data in a more focused geographic extent along with the application of increasing constraints such as technical, geological, and economic to the CO_2 storage capacity, as defined by CSLF.

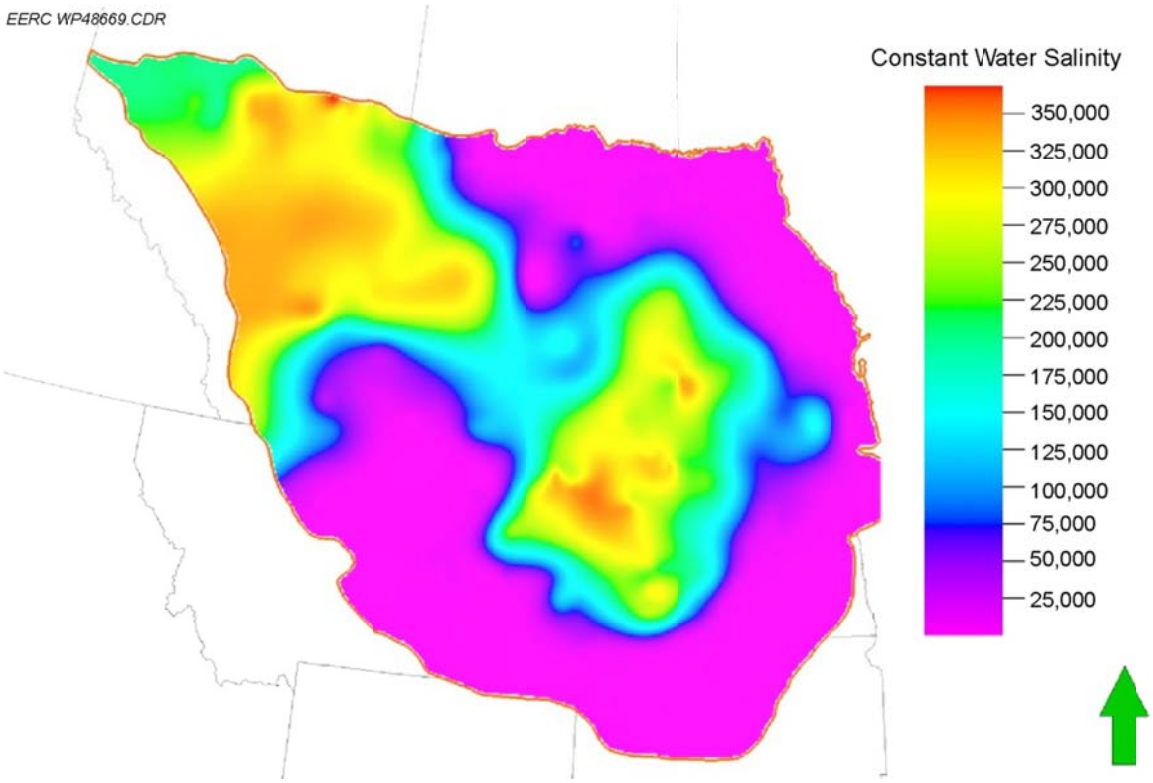

Figure 28. Water salinity (ppm) of the basal saline system.

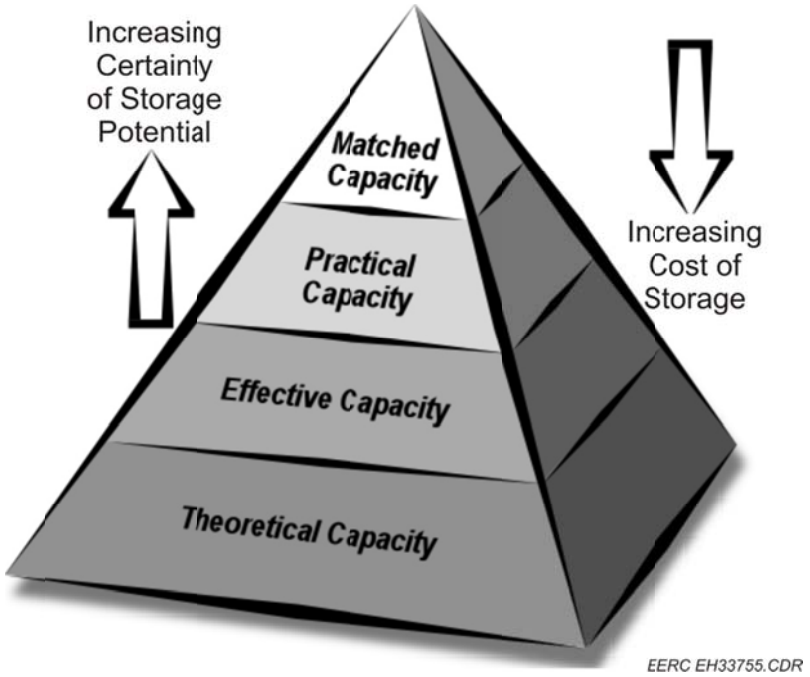

Figure 29. CSLF techno-economic resource–reserve pyramid (CSLF, 2007).

Gorecki and others (2009) proposed a refined classification incorporating terms defined by DOE (U.S. Department of Energy Office of Fossil Energy, 2008) that distinguish between storage estimates defined by physical and chemical constraints (resource) and those with added economic and regulatory constraints (capacity) (Figure 30). The first two divisions within this proposed classification framework, theoretical and characterized storage resource, are equivalent to the theoretical capacity of the CSLF pyramid. The effective storage resource refines the broader level estimates by integrating geologic and engineering limitations. This level is equivalent to the CSLF's definition of effective storage capacity, although here it is defined as a resource since economic considerations have not been implemented.

As mentioned earlier, the approach to estimating the CO_2 storage volume, as well as the required level of detail for the required data, will vary depending on the geographic scale of the assessment effort. In its Phase 2 final report, CSLF (2007) presented five terms representing scales of geographic extent for the assessment of CO_2 storage. These terms, in order of decreasing area, are country, basin, region, local, and site. Confidence in the calculated storage potential increases as the geographic scale decreases. Gorecki and others (2009) augment this geographic hierarchy by incorporating a level of spatial scale as defined by political subdivisions (Figure 31). Using the terminology presented in the previous paragraphs, this study attempts to estimate the effective storage resource of the COSS at the basin/regional scale across the northern Great Plains and Prairie regions of the central interior of North America.

Static Capacity of the Basal Saline System

The methodology used in this study follows the approach described in DOE Atlas III (U.S. Department of Energy Office of Fossil Energy, 2010) which builds on the IEAGHG work of Gorecki and others (2009). It is based on the volumetric approach for estimating CO_2 storage resource potential saline formations. The volumetric equation to calculate the CO_2 storage resource mass estimate for geologic storage in saline formations is:

$$MCO_2e = A \times h \times \varphi \times \rho CO_2 \times E_E \qquad \text{[Eq. 5]}$$

The total area (A), gross formation thickness (h), and total porosity (φ) terms account for the total bulk volume of pore space available. The value for CO_2 density (ρ) converts the reservoir volume of CO_2 to mass. The storage efficiency factor (E) reflects the fraction of the total pore volume that will be occupied by the injected CO_2. For saline formations, the CO_2 storage efficiency factor (E_E) is a function of geologic parameters (E_{geol}), such as area, gross thickness, and total porosity, that reflect the percentage of volume amenable to CO_2 sequestration and displacement efficiency components ($E_V E_D$) that reflect different physical barriers inhibiting CO_2 from contacting 100% of the pore volume of a given basin or region (Equations 6 and 7). Volumetric methods are applied when it is generally assumed that the formation is open and that formation fluids are displaced from the formation or managed via production. The COSS is assumed to be an open system for the purpose of this study. A comprehensive discussion of the derivation of the methodology and the efficiency factor is presented in Gorecki and others (2009), U.S. Department of Energy Office of Fossil Energy (2010), and Goodman and others (2011).

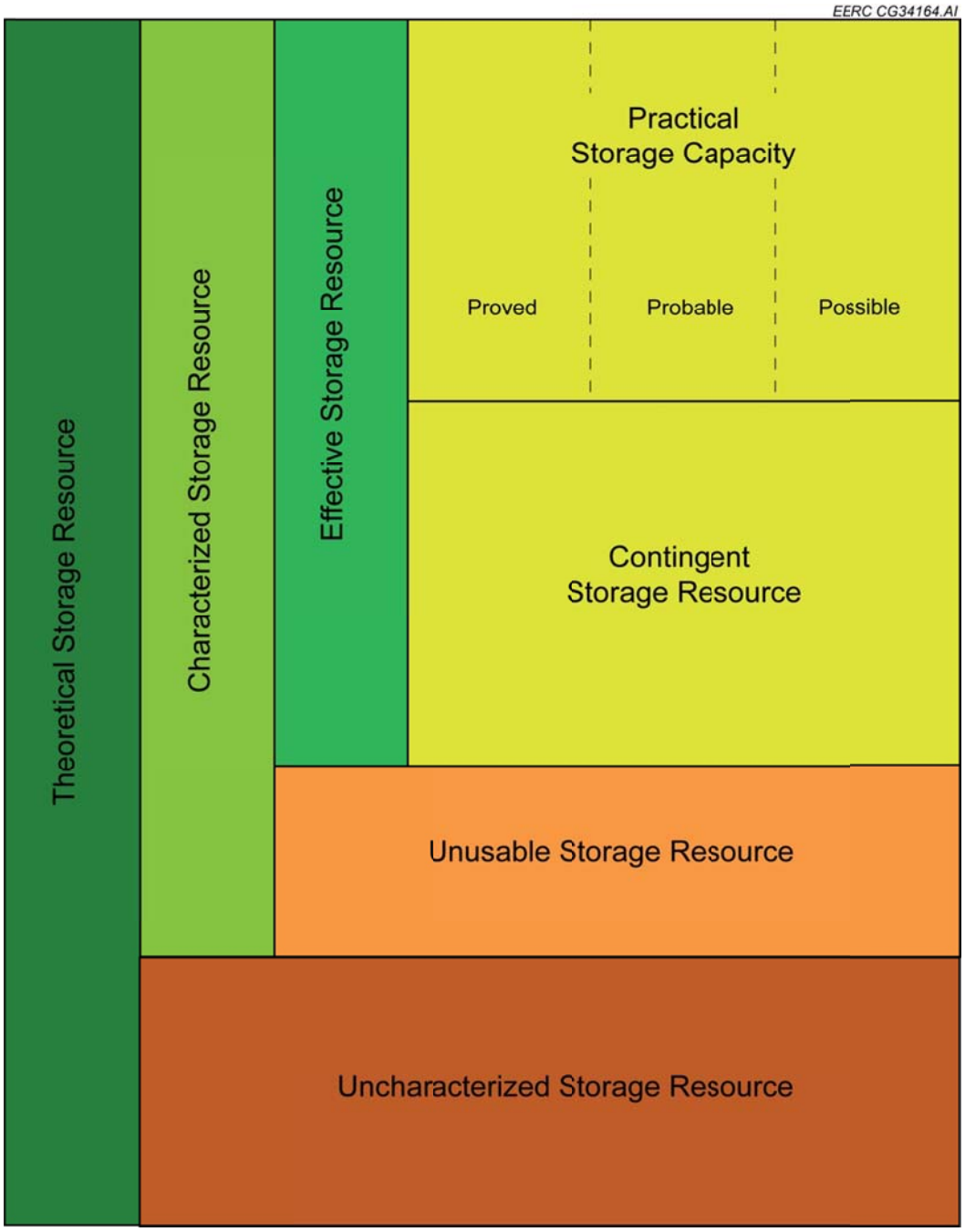

Figure 30. CO_2 storage classification framework.

$$E_E = E_{geol} \times E_v E_d \quad \text{[Eq. 6]}$$

$$E_{geol} = \frac{A_n}{A_t} \times \frac{h_n}{h_t} \times \frac{\varphi_n}{\varphi_T} \quad \text{[Eq. 7]}$$

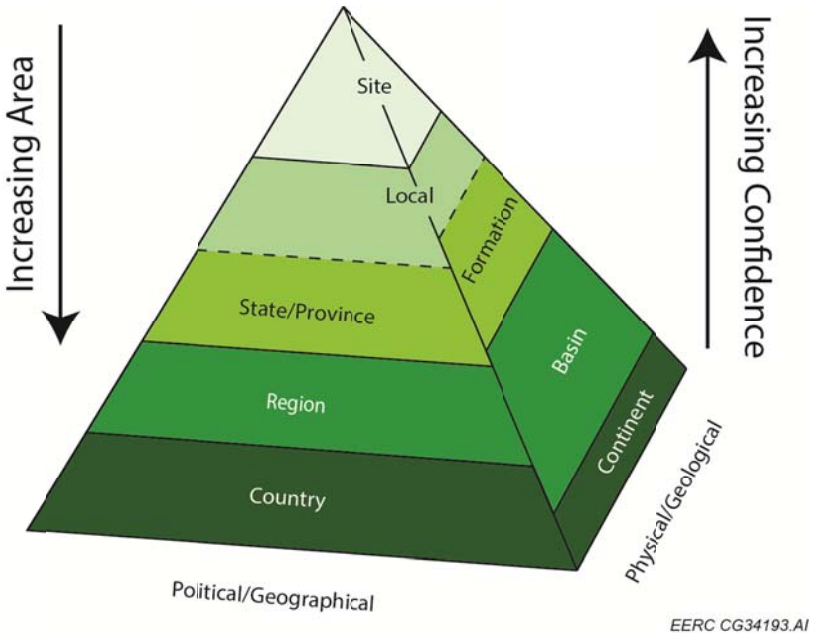

Figure 31. Political/geographic, physical/geologic pyramid of assessment area types and scales.

This storage amount calculated excludes areas where the saline system is unconfined and where the TDS is <10,000 ppm. These areas are excluded because injection will not occur because of leakage and regulations regarding the injection of CO_2 into potable water used for residential, agricultural, or industrial use. Other areas excluded are depths <2500 ft, where CO_2 is not considered to be a supercritical fluid.

CO_2 density was calculated based on the relationship of pressure, temperature, and density defined by the National Institute of Standards and Technology (2003). Temperatures and pressures were exported from the working Petrel project into a look-up function where CO_2 density is calculated. CO_2 density was then interpolated across the U.S. portion of the basal saline system using a kriging algorithm (Figure 32).

After CO_2 density was calculated, Equation 5 was applied to determine the overall storage resource of CO_2. The overall storage resource utilized saline storage efficiency values for a clastic depositional system from DOE's Office of Fossil Energy Atlas III and IV (2010, 2012). These values were used because the net-to-total area, net-to-total gross thickness, and effective-to-total porosity are known from the characterization activities above. This net volume includes a 10,000 ppm salinity cutoff and a 10% porosity cutoff, eliminating a majority of the strata with permeabilities greater than 5 mD. Utilizing the storage coefficients, a total of ~412 Gt of CO_2 could theoretically be stored in the P50 case for the basal saline system (Figure 33). Table 1 shows the P10, P50, and P90 efficiency factors and calculated CO_2 storage capacity volumes.

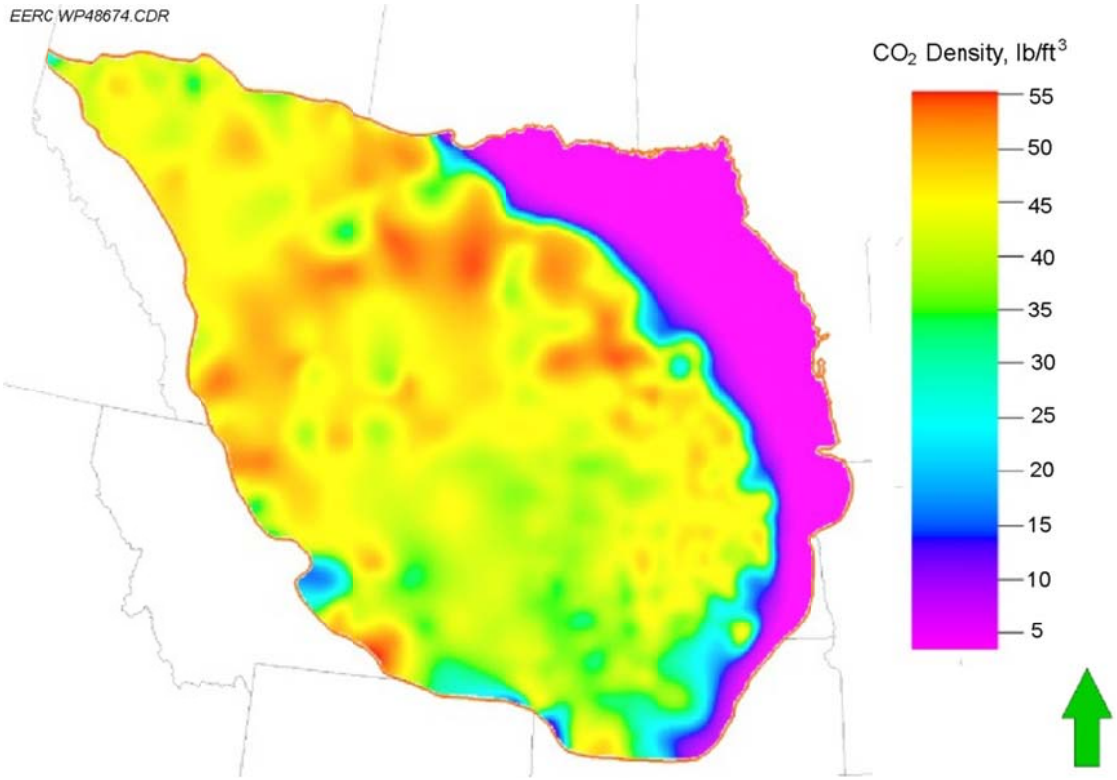

Figure 32. CO_2 density of the basal saline system and outline of the injectable area for sequestration (lb/ft^3).

DYNAMIC SIMULATION

To further evaluate this extensive saline system, and thus its viability as a potential sink, the geocellular model was used as the framework for an assessment of the dynamic storage capacity of the basal saline system with respect to the large-scale CO_2 sources in the region. Static storage resource calculations do not consider the effect of dynamic factors such as injection rate, injection pattern, timing of injection, and pressure interference between injection locations. Numerical simulation is a method that can be used to validate the estimate of the effective storage resource potential of deep saline formations by addressing the effects of multiple large-scale CO_2 injections. The main goal of this effort is to compare volumetric storage resource estimates with estimates with dynamic storage potential for the large-scale sources in the study region.

Through the dynamic simulation effort two main objectives were established: 1) assess the dynamic storage capacity of the saline system assuming the 16 aggregated major large CO_2 sources located above or in close vicinity to this saline system will choose it for CO_2 storage during their respective lifetime and 2) assess the effect of pressure-related changes induced by the injection of large volumes of CO_2. To address these objectives, two dynamic injection scenarios were designed based on the base case static model. The two scenarios determine the injectivity of the saline system through the simulated injection of ~104 Mt/yr of CO_2 from the 16 aggregated sources.

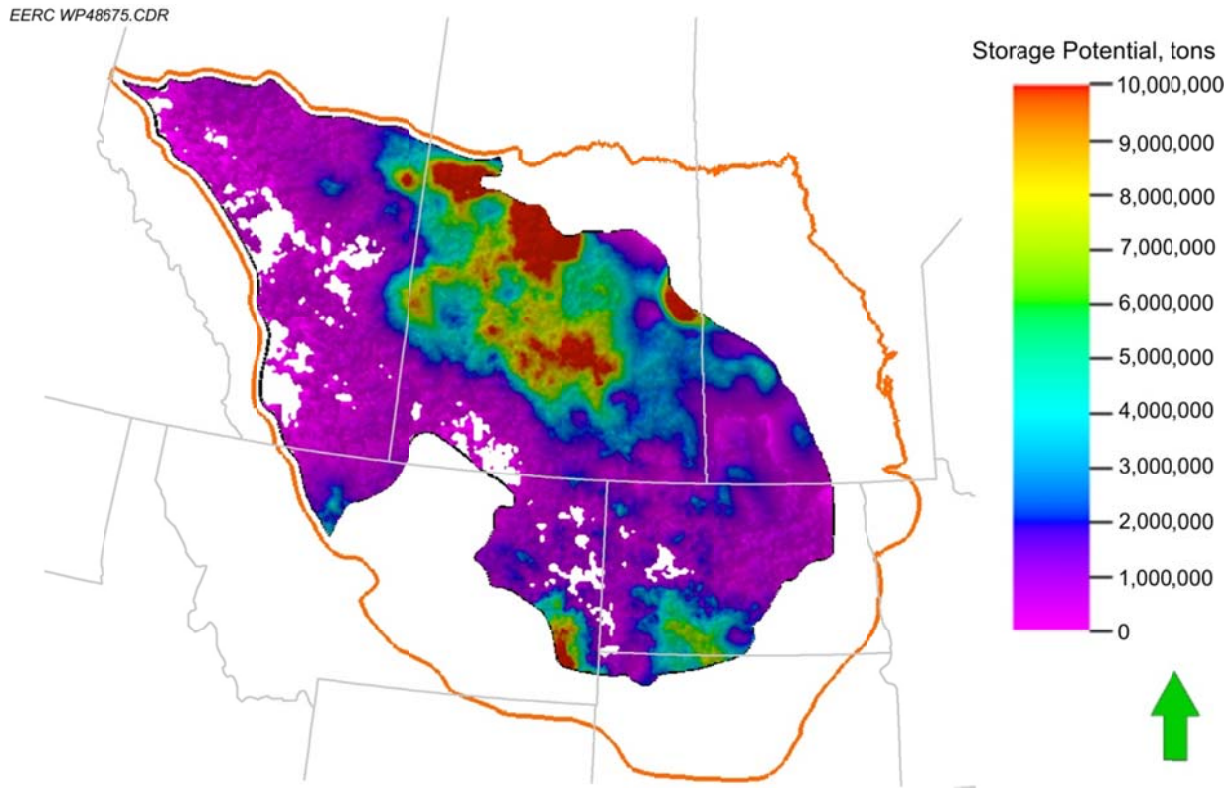

Figure 33. Storage potential (tons) of the basal saline system using a P50 efficiency factor of 9.1%.

Table 1. Storage Coefficients for Saline Formations and Storage Potential for the Basal Saline System

	P10	P50	P90
E_{geol}*, %	65	65	65
$E_v \times E_d$, %	7.4	14	24
E_E, %	4.8	9.1	15.6
CO_2 Storage Capacity, Gt	218	412	706

* $E_{geol} = A_n/A_t \times h_n/h_t \times \varphi_n/\varphi_T$; because the area is known $A_n/A_t = 1$.

Each of the two dynamic injection scenarios has multiple cases, and each case varied parameters that affected the dynamic simulation in an effort to optimize overall CO_2 injection. The first scenario positioned injection clusters at the locations of the 16 aggregated CO_2 sources. The second scenario partitioned the sources into 25 feeds that were piped to regions with "better" reservoir characteristics (i.e., high permeability of connected volumes) to optimize injection. The varying cases build upon one another in regard to changes, including the vertical to horizontal permeability ratio (Kv/Kh), addition of water extraction wells, relative permeability, rock compressibility, and horizontal injection. All of the dynamic simulations were performed using Computer Modelling Group's (CMG) software package (www.cmgl.ca/).

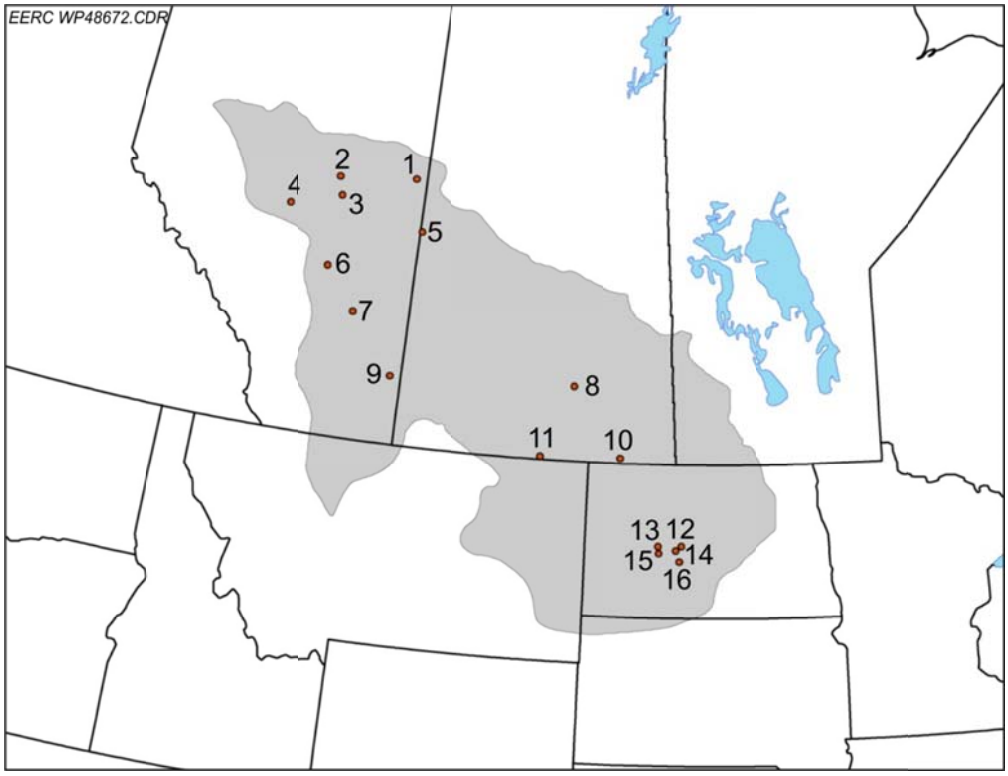

Figure 34. Locations of the aggregated CO_2 sources overlaying the portion of the basal saline system that meets injection standards (see Table 3 for corresponding ID number).

Sources Used for Dynamic Simulation

There are 25 large stationary sources within the area of the Cambro-Ordovician system where TDS values are higher than 10,000 ppm. Based on the close proximity of several of the sources, these 25 sources have been aggregated into 16 aggregated source points (Figure 34). In an effort to create a "realistic" injection scenario, a tiered approach was developed. The foundation of this approach is that a multiunit coal-fired power plant would not install a CO_2 capture system on each combustion unit in the first year. As an example, the Boundary Dam Power Station is currently retrofitting one of its three units for capture. The others would come online at some future date.

For this initial scenario-building effort, 29 CO_2 input events were developed (Table 2). The earliest event is the Boundary Dam project in 2014, and the latest is the Lloydminster plant in 2031. Other than Boundary Dam's planned 2014 date and Shell's Quest project date of 2015, all other dates are arbitrary. A graph of the deployment/injection scenario is shown in Figure 35. Based on this scenario, the maximum annual captured and injected CO_2 for the region will be reached in 2031 (104 Mt/yr). The cumulative mass of CO_2 that will have been injected at that time is 1020 Mt.

Table 2. CO_2 Sources and Their Respective Location, Plant Type, Annual Emissions, and Theoretical Injection Year

Plant	State/ Province	Plant Type	Total Annual CO_2 to Be Injected, Mt	Injection Year
Poplar River Power Station	SK	Electric generation	3.8	2022
CCRL/NEI Refinery-Upgrader Complex	SK	Petroleum and natural gas	1.7	2019
Boundary Dam Power Station	SK	Electric generation	1, 7.6	2014, 2019
Coyote	ND	Electric generation	2.8	2021
Milton R. Young	ND	Electric generation	1.65, 3.71	2019, 2024
Coal Creek	ND	Electric generation	3.82, 4.17	2016, 2018
Medicine Hat–Empress	AB	Mixed	5.2	2030
Hanna	AB	Electric generation	4.4	2026
Joffer–Forestburg	AB	Petroleum and natural gas	7.1	2028
Lloydmister	AB	Electric generation	2.1	2031
Duffield–Warburg	AB	Electric generation	3.80, 3.80, 3.80, 3.80, 3.80, 3.80	2019, 2021, 2023, 2025, 2027, 2029
Edmonton/Redwater	AB	Mixed	9.7	2020
Shell Quest	AB	Mixed	1.2	2015
Cold Lake–Bonnyville	AB	Petroleum and natural gas	8.3	2017
Antelope Valley/Dakota Gasification Company	ND	Multiple	2.15, 3.20, 2.61	2018, 2020, 2025
Leland Olds/Stanton	ND	Electric generation	1.03, 0.41, 2.11, 0.76	2019, 2020, 2021, 2025

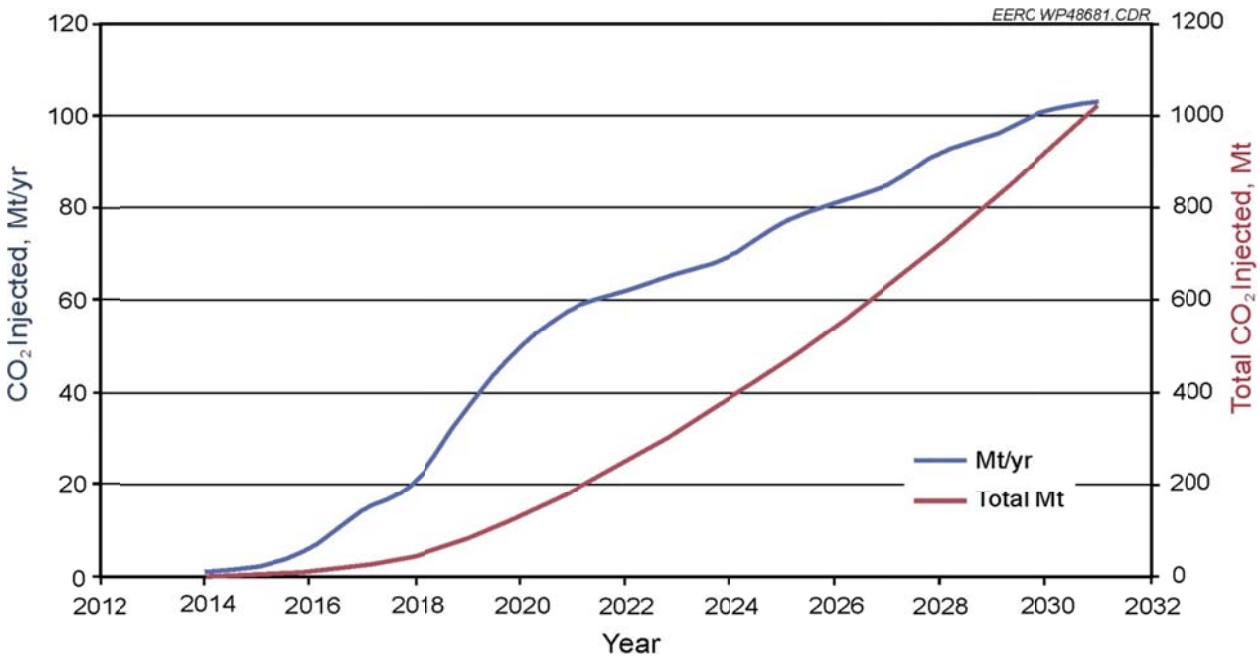

Figure 35. Deployment/injection scenario.

Table 3. Aggregated CO_2 Sources Location, Plant Type, and Annual CO_2 Output Used in the Injection Scenarios During Dynamic Simulation

Plant	State/ Province	Plant Type	Total Annual CO_2	ID No.
Cold Lake–Bonnyville	AB	Petroleum and natural gas	8.3	1
Shell Quest	AB	Mixed	1.2	2
Edmonton/Redwater	AB	Mixed	9.7	3
Duffield–Warburg	AB	Electric generation	23.0	4
Lloydminster	AB	Electric generation	2.1	5
Joffre–Forestburg	AB	Petroleum and natural gas	7.1	6
Hanna	AB	Electric generation	4.4	7
CCRL/NEI Refinery-Upgrader Complex	SK	Petroleum and natural gas	1.7	8
Medicine Hat–Empress	AB	Mixed	5.2	9
Boundary Dam Power Station	SK	Electric generation	8.6	10
Poplar River Power Station	SK	Electric generation	3.8	11
Coal Creek	ND	Electric generation	8.9	12
Antelope Valley/Dakota Gasification Company	ND	Multiple	8.0	13
Leland Olds/Stanton	ND	Electric generation	4.3	14
Coyote	ND	Electric generation	2.8	15
Milton R. Young	ND	Electric generation	5.3	16

Static Model Upscaling

The static model discussed in the previous section serves as the basis for the CO_2 injection simulations. The base grid of the static model was constructed with 2250-ft^2 grid blocks with 25 proportional vertical layers. Because of the large aerial extent of the saline system, the base grid resulted in a ~115-million-cell geocellular model. In order to efficiently investigate multiple dynamic simulation scenarios, the number of cells (complexity) of the static model was reduced through upscaling and grid refinement. The study area, mentioned in detail in the previous sections of this report, includes sixteen aggregated large-scale CO_2 sources that emit over 1 Mt of CO_2 annually. Injection wells were placed at the locations of the CO_2 sources and used as the center point for the grid refinement in the model. Originally, the grid was upscaled with five different gridding intervals radiating away from the injection points. Although the five local grid refinements were ideal, there were issues bringing the multilayer refinement into CMG for simulation using Petrel's rescue format. To avoid this issue, the aerial extent of the original geocellular grid was upscaled from 2250' × 2250' to 7000' × 7000' in a ~20-mile radius around each CO_2 source point and upscaled to 35,000' × 35,000' in the outer areas of the study region (Figure 36). This allowed for heterogeneity to be kept within the polygons where the injection wells are placed. This process upscaled the properties using different averaging techniques to redistribute the petrophysical properties from the base grid.

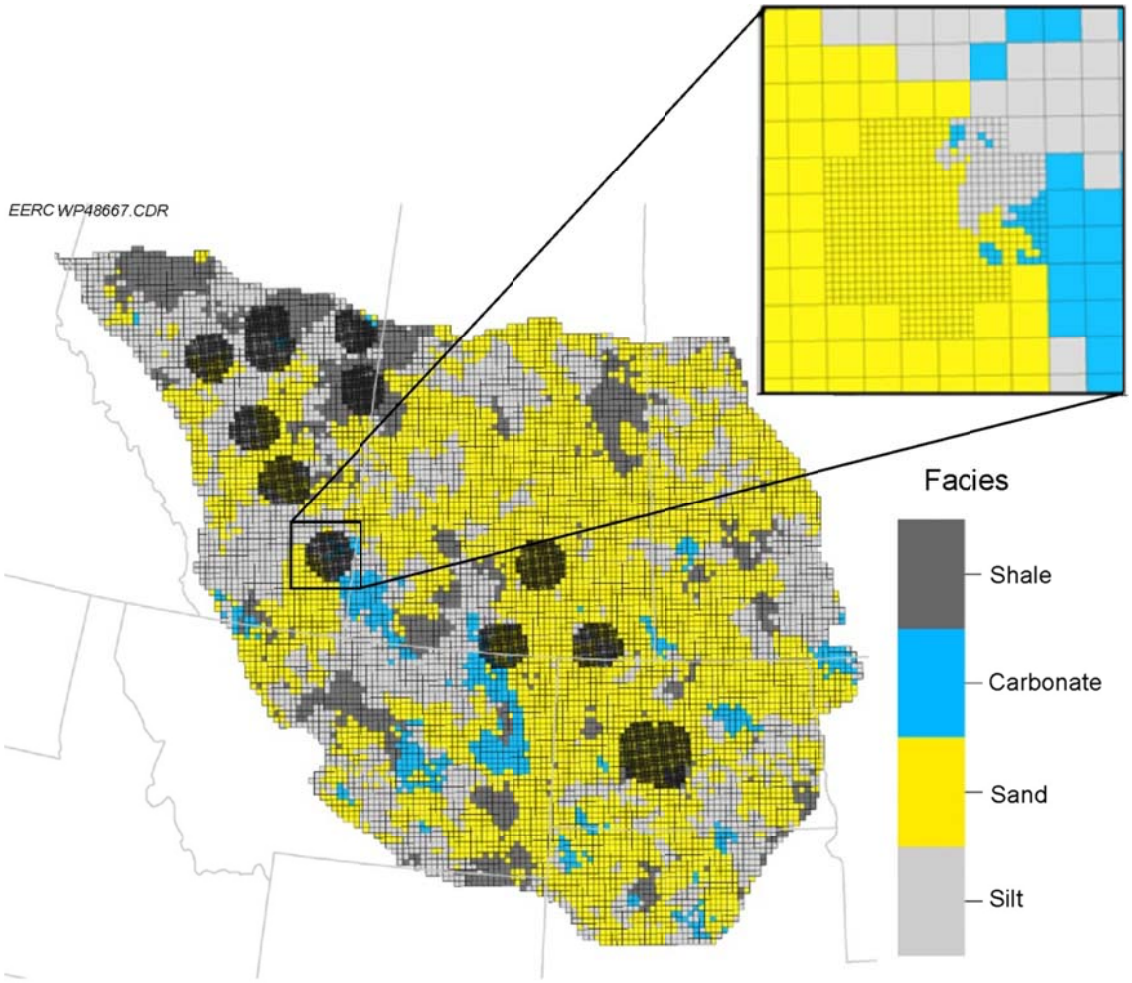

Figure 36. Local grid refinement around the large-scale CO_2 sources for Scenario 1.

Well Placement

The annual emission rate of 16 aggregated large-scale CO_2 sources is about 104 Mt with an expected 90% capture from 115 Mt of total emission (Table 2). The injection wells were placed in the finer resolution grid, with one well per 0.5 Mt of CO_2 emitted annually for the source it represented after injection rate sensitivity analysis. This ratio resulted in 210 and 211 injection wells for Scenarios 1 and 2, respectively. If the cases within a scenario included water extraction, all of the extractors were placed around the injectors following a 5-spot pattern.

Model Settings

Injection occurs in areas where TDS is greater than 10,000 ppm, a requirement by the Safe Drinking Water Act, which defines potable water as having TDS levels less than 3000 ppm and underground sources of drinking water as having less than 10,000 ppm (U.S. Environmental Protection Agency, 2012). As seen in the static model (Figure 28), the TDS increases to higher

than 300,000 ppm. The fluid settings in the dynamic simulation correspond with the static model to determine the dissolution of CO_2 in the brine mixture. Henry's Law constant was correlated by Harvey's method to determine the solubility coefficient of CO_2 in the brine. Aqueous density and viscosity of the fluids were correlated by using the Rowe–Chou and Kestin methods, respectively, over the varying temperatures and pressures of the location. The fluid model and rock–fluid settings for the dynamic simulation were based on the lithologies of the static geologic model. Relative permeability curves were obtained from published data (Bennion and Bachu, 2005) for different sedimentary lithologies including the sands, carbonates, and shales of the COSS.

Numerical Tuning

The numerical tuning technique was used to optimize the numerical settings for increasing the speed of the simulation runs. Various parameters such as pressure change and the tolerance of convergence over each time step were tracked to tune the integrated settings for producing the lowest optimization critical points (Griffith and Nichols, 1996; Hutchinson, 1989; LeDimet and others, 1995). The optimization critical points used in the project included material balance error, central processing unit (CPU) time, and simulator failure percentage. After numerical tuning, depending on the simulation scenario, up to 40% reduction in running time can be achieved.

Scenario 1

The first scenario of the dynamic simulation includes a base case and seven additional cases to explore the CO_2 storage capacity below the 16 aggregated point sources based on various factors. As mentioned in the upscaling process, a polygon was centered on each CO_2 source, placing the injection wells within a radius of 20 miles. Injection cases were then applied at each location exploring the sensitivity of the input parameters. Changes in parameters include increasing and decreasing Kv/Kh, inclusion of water extraction wells, changes in relative permeability, and a stepwise injection rate. The simulation period in each case has an injection period and a postinjection period to monitor the pressure transient.

Base Case

Seen in Figure 37, the base case includes a total of 16 wells, which is one vertical injector for each CO_2 emission source. Injection occurs over a 36-year time span (2014–2050), with an additional 50-year postinjection time span to monitor the pressure transient. The vertical to horizontal permeability ratio (Kv/Kh) is set at 0.1, and relative permeability is defined with the curves from Bennion and Bachu (2005).

During simulation of the base case, a large amount of CO_2 is injected using only 16 wells. The injection over a 36-year time span allowed for a total of 82 Mt of CO_2 to be injected which is 2.2% of the total annual CO_2 emissions from these sources (Table 4). Each of the following cases modifies parameters from this base case to optimize injection of CO_2.

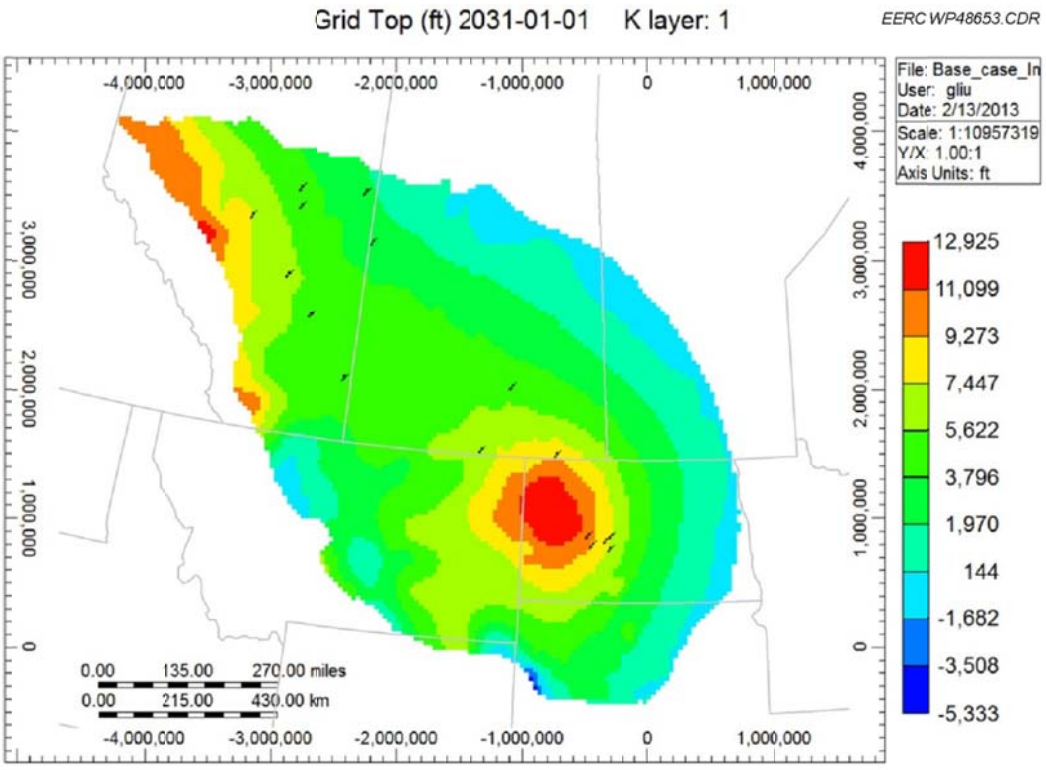

Figure 37. Location of injection wells for the base case overlain on the grid top.

Table 4. Results of the Simulation Cases of Scenario 1 (columns display the parameters for each case and the total amount of CO_2 injected)

Case	Total Injectors	Years of Injection	Postinjection, years	Water Extraction Area	Kv/Kh Ratio	Real Perm. Curves	Total Injected CO_2, Mt	Injected CO_2, %
Base	16	36	50	No	0.1	No change	82	2.2
1	210	36	50	No	0.1	No change	752	20.1
2	210	36	50	Duffield–Warburg	0.1	No change	1005	26.9
3	210	36	50	Duffield–Warburg	0.4	No change	996	26.6
4	210	36	50	Duffield–Warburg	0.6	No change	991	26.5
5	210	36	50	Duffield–Warburg	0.1	Changed	1024	27.4
6	210	50	36	Duffield–Warburg	0.1	Same as Case 5	1541	29.6
7	210	50	36	Duffield–Warburg	0.1	Same as Case 5	1412	27.2
Expected Total CO_2 Injection for All of the Emission Resources over 36 or 50 years							3744 or 5200	

Case 1

Case 1 is built upon the base case by adding injectors to each cluster dependent on the magnitude of the CO_2 source (Figure 38). The total number of injection wells increased from 16 to 210 to meet the ~104 Mt of CO_2 annual rate by the regional large CO_2 sources. Each injector was set with a target injection rate of 0.5 Mt/yr. By increasing the amount of injectors, a substantial increase was observed in the amount of CO_2 injected into the target system. Over a 36-year time span, a total of 752 Mt was injected, which is 20.1% of the total emissions from these sources (Table 4). Based on these results, each injection well averaged about 100,000 tons/yr of CO_2 injection, and at these rates, about 1045 wells would have been required to meet the injection target of 3744 Mt.

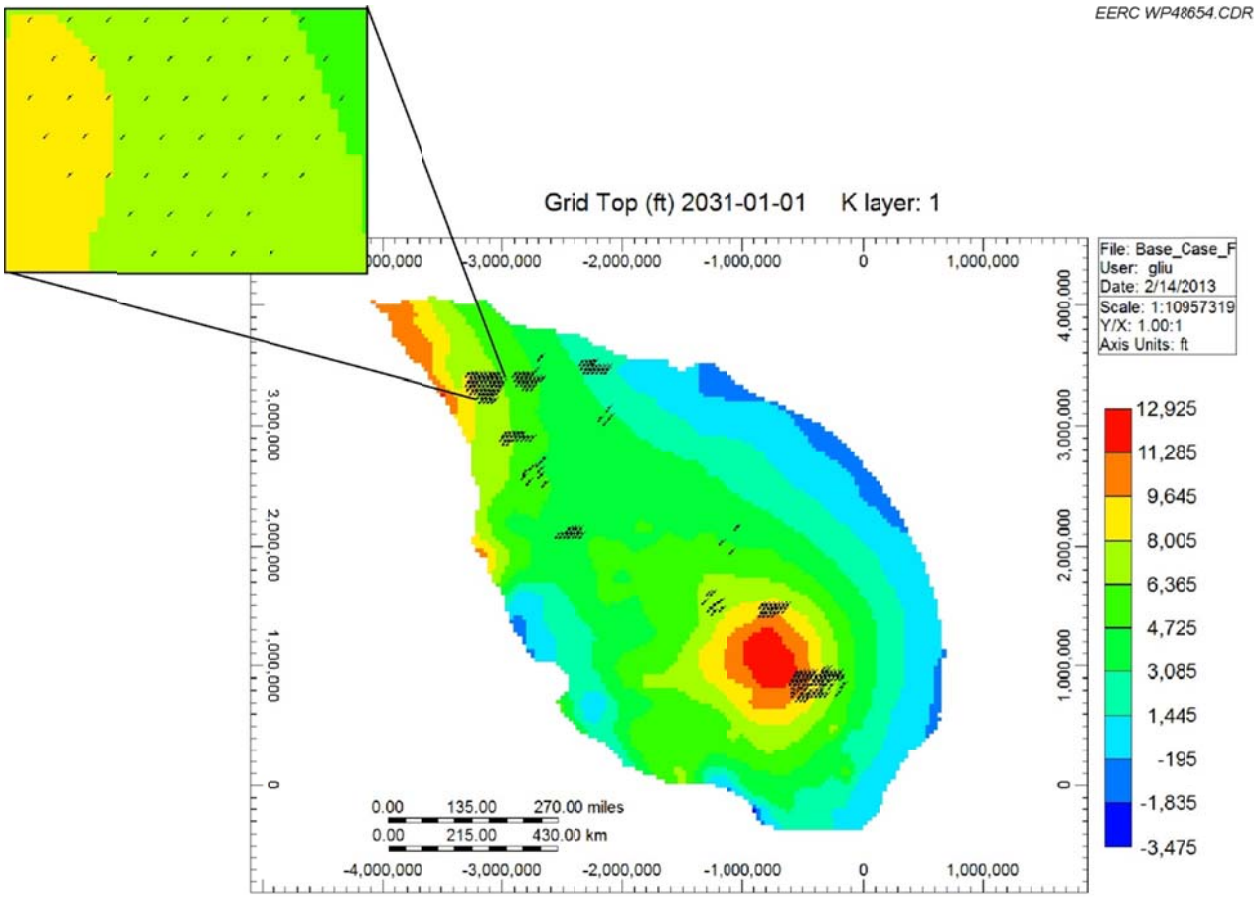

Figure 38. Case 1: 196 injectors were added on the base case to help increase CO_2 injection (210 total wells) overlain on the grid top.

Case 2

Case 2 added water extraction wells to the Duffield–Warburg complex where emissions total ~22.8 Mt of CO_2 annually in this local area (Figure 39). This is also the location with the most injection wells at 48. Adding the water extraction wells provided more pore volume access for the injected CO_2, as well as reduced pressure buildup in the local area. Utilizing water extraction wells to the Duffield–Warburg increased the injected CO_2 to a total of 1005 Mt which is 26.9% of the total emissions from these sources (Table 4). This resulted in an average annual injection rate of about 133,000 ton/yr per well. At these average injection rates, 780 wells would have been required to inject the target amount of 3744 Mt over the 36-year period.

Cases 3 and 4

Cases 3 and 4 increased Kv/Kh from 0.1 to 0.4 and 0.6, respectively, based on Case 2. Although the change in Kv/Kh slightly changes the overall storage, total injection CO_2 of Cases 3 and 4 are 996 and 991 Mt, respectively, over a 36-year time span which is about 0.5% different compared to Case 2.

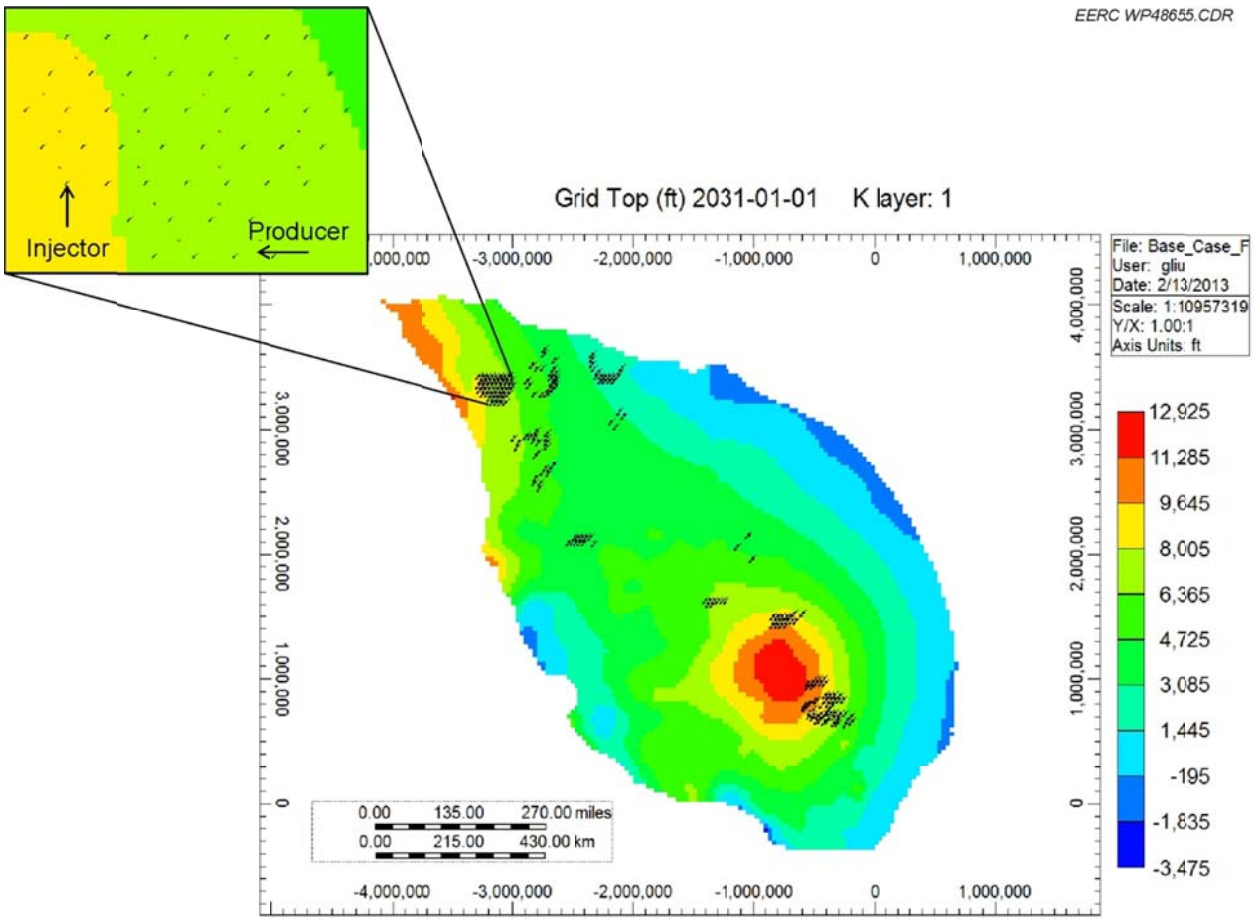

Figure 39. Case 2: Water extraction wells were added to the Duffield–Warburg area to enhance CO_2 injection overlain on the grid top.

Case 5

Case 5 built upon Case 2 by changing the residual gas and water to adjust relative permeability curves over the simulation. The curvature of the relative permeability curves are altered using exponents of Corey's equations. Overall changes in the relative permeability curves affect the amount of irreducible water and gas saturation. Case 5 increased a fraction in comparison to Case 2 with a total injection of 1024 Mt which is 27.4% of the total emissions from the sources.

Cases 6 and 7

Case 6 uses a stepwise approach to bring CO_2 injection online over the 50-year injection period, while Case 7 added up all CO_2 sources and injected all of the CO_2 at once from the beginning (Figure 40). Injecting all of the CO_2 at once decreased the overall injection from 1541 Mt in Case 6 with stepwise injection rate to 1412 Mt. Seen in Figure 41, Case 7 initially injects more cumulatively in the early years than Case 6, but eventually decreases in the later years caused by a quicker pressure buildup in the reservoir. This is the reason that Case 6 injected about 7.6% more CO_2 into the basal saline system than Case 7 overall.

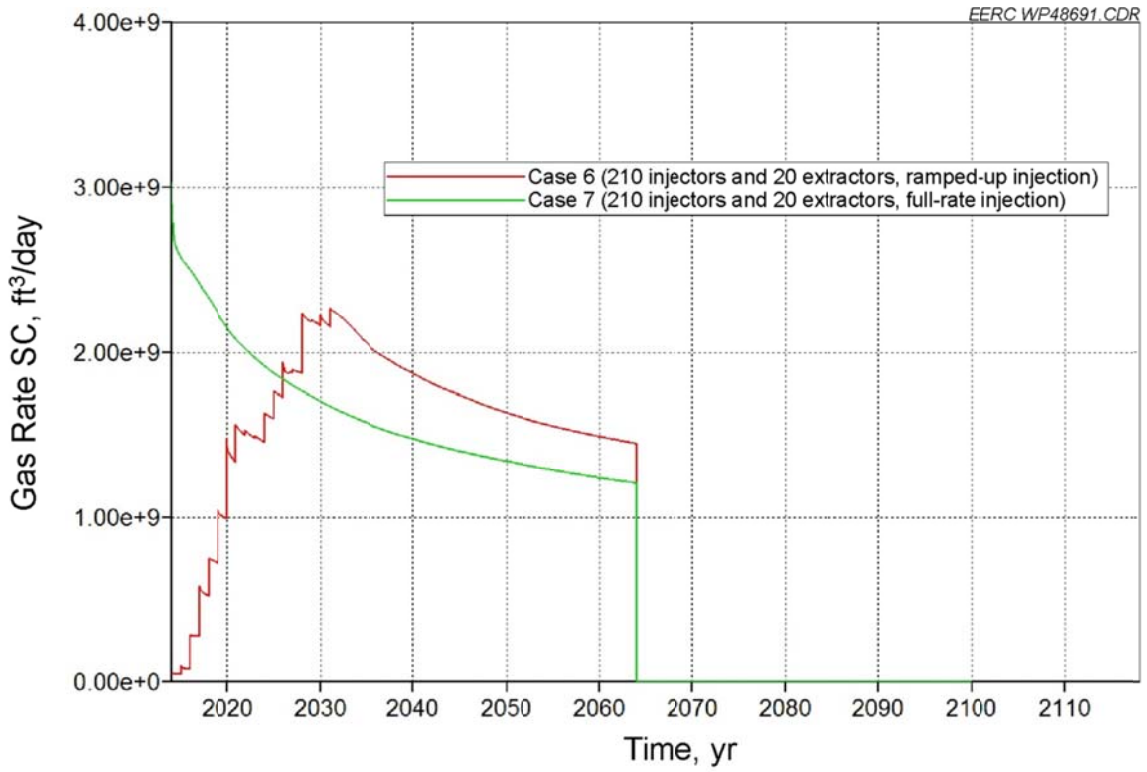

Figure 40. Injection rates of Cases 6 and 7. Case 6 uses stepwise injection, while Case 7 uses an added up constant rate from the beginning.

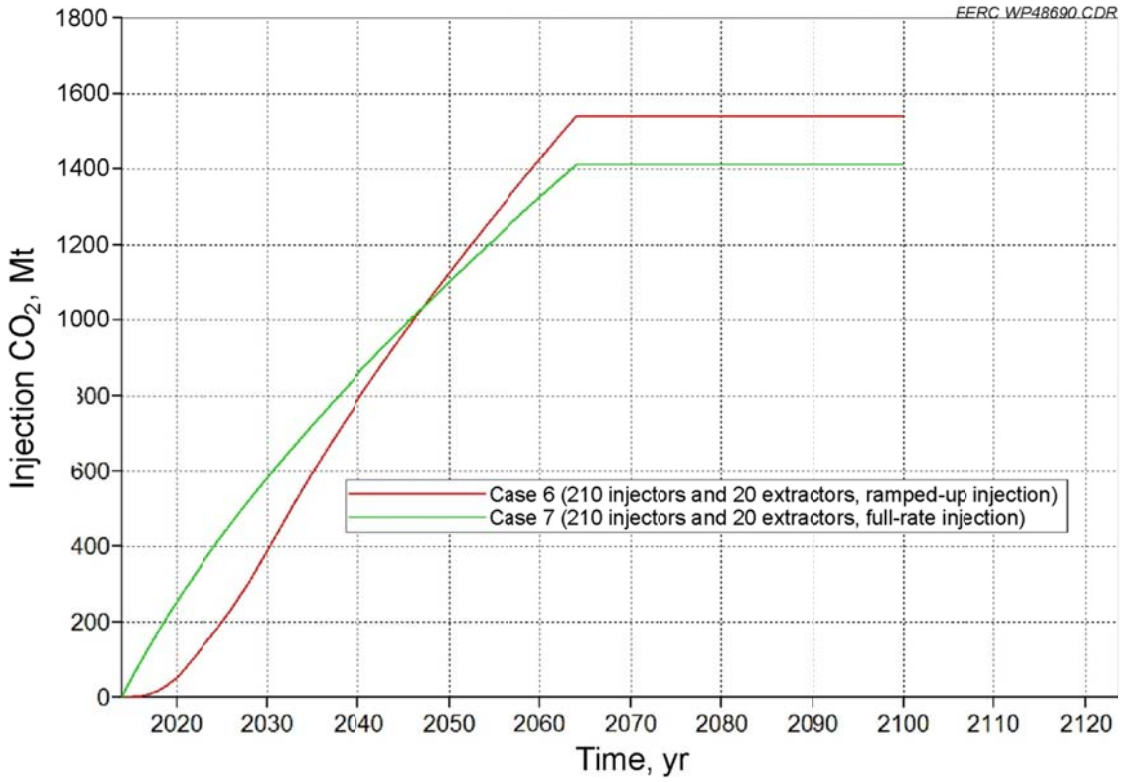

Figure 41. Overall injection of CO_2 for Cases 6 and 7. Although Case 7 stores more CO_2 in the initial years, the stepwise injection in Case 6 ultimately stores more CO_2 because of a slower reservoir pressure buildup.

Summary of Scenario 1

Simulation results of Scenario 1, a total of eight cases, provided storage potential centered on each CO_2 source in the basal saline system region (Table 4). The base case served as a baseline and allowed for the seven additional cases building upon one another to investigate the effect of various parameters on the overall CO_2 storage capacity. Changes to the cases included adding more injector wells, adding water extraction, modifying the Kv/Kh, modifying the relative permeability curves, and implementing stepwise or ramped-up injection rates.

Simulation of Cases 1 to 5 had an injection period from 2014 to 2050 and a postinjection period from 2050 to 2100. Figure 42 shows that Case 5 gives the most optimal results by injecting 1023 Mt of CO_2 which is 27.4% of the total emissions. However, Cases 2–4 are relatively similar, showing that changes to the relative permeability and Kv/Kh ratio have a small effect on the overall injection. The two largest impacts among five cases are the additional injection wells, from 16 in the base case to 210, and adding water extraction wells to the Duffield–Warburg area. Using a stepwise injection approach helped inject slightly more of the CO_2 (Case 6) than being injected all at once (Case 7). Figures 42 and 43 show the impact each changed parameter had on the overall effect of total CO_2 storage.

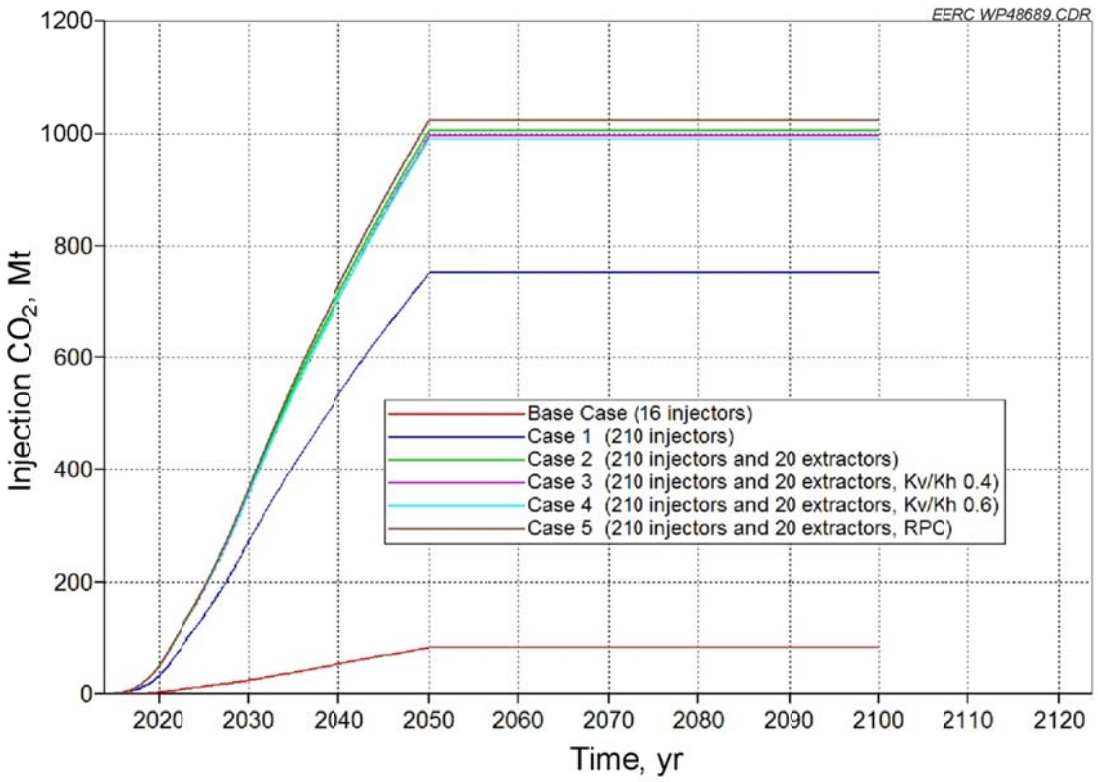

Figure 42. Results of Scenario 1 show the effect the parameters have on the overall injection of CO_2.

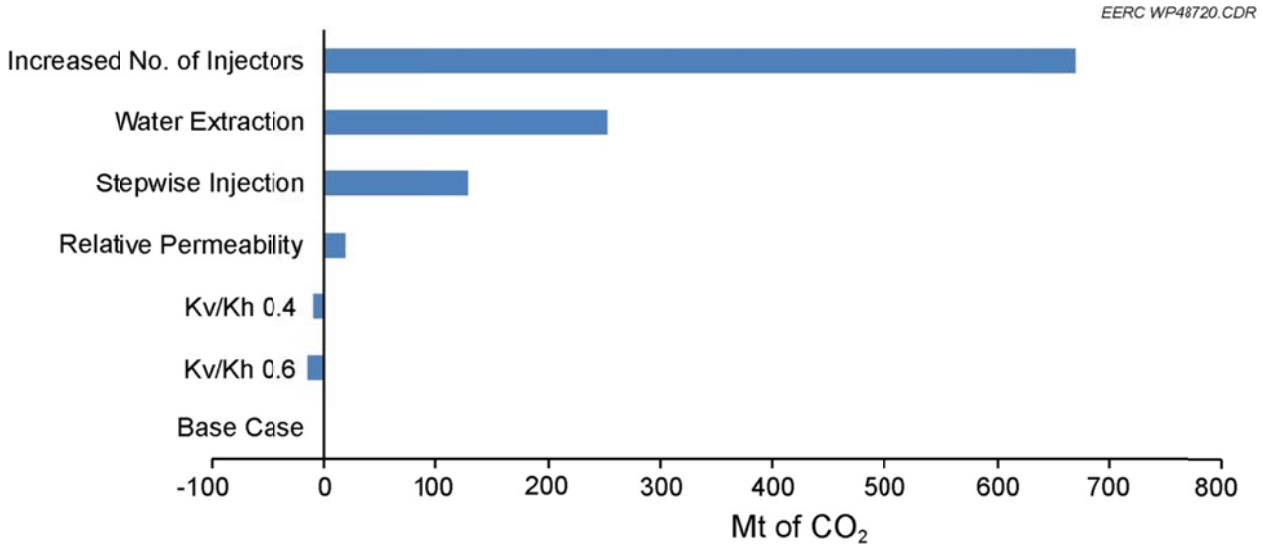

Figure 43. The overall effect of injected CO_2 based on adjustment of the variables used in Scenario 1.

The results of Scenario 1 indicate that per well injectivity of 100,000–150,000 tons/yr was achieved; however, a target of 500,000 tons/yr was needed to reach the targeted storage mass. At these injection rates, about 700–1050 injection wells would have been required to meet the storage target.

Scenario 2

In each case of Scenario 1, the reservoir was unable to accept the target levels of CO_2. To investigate an option to increase total injection, a second scenario was devised to distribute the 16 injection clusters used in Scenario 1 to 25 clusters distributed in areas where reservoir volume connection (geobodies) occurs with higher permeability in the geocellular model. Geobodies were created utilizing a cutoff to determine areas in the model where permeability is greater than 50 mD. It means that a connected volume is essentially a volume of connected cells that are directly adjacent to one another and share an assigned property of cutoff. The 16 original injection locations were disaggregated and moved (pipelined) to the large connected volumes in close relation to the original injection clusters (Figure 44). The new locations then underwent the same workflow for local grid refinement to 7000 × 7000 ft based on the global grid size 35,000 × 35,000 ft (Figure 45).

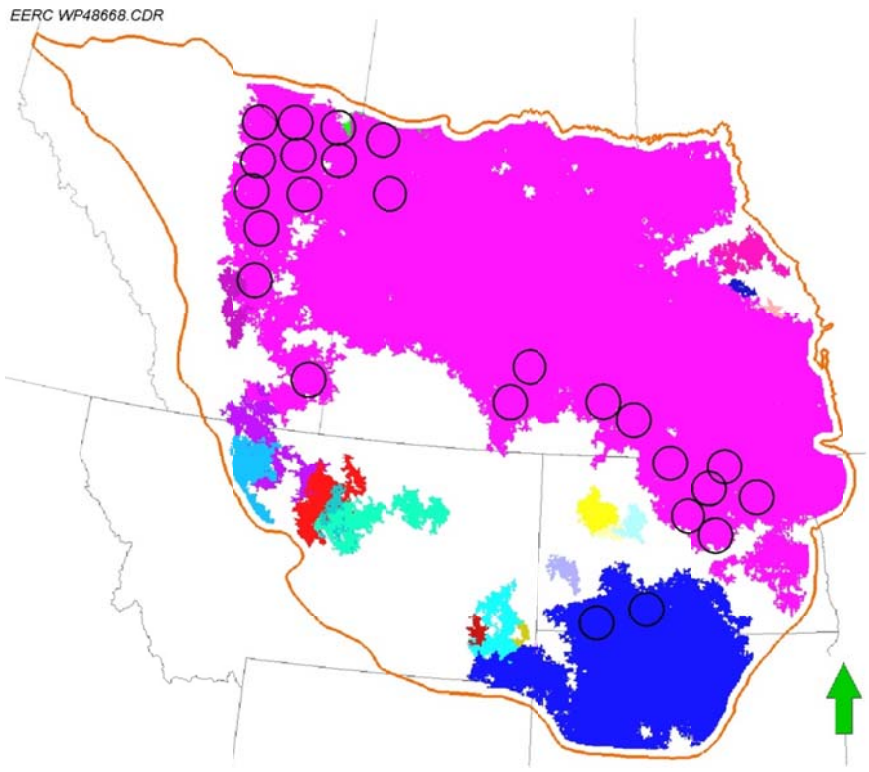

Figure 44. Connected volumes of the basal saline system with a cutoff of permeability greater than 50 mD. Twenty-five injection clusters of Scenario 2 are located in the connected volumes as marked by black circles.

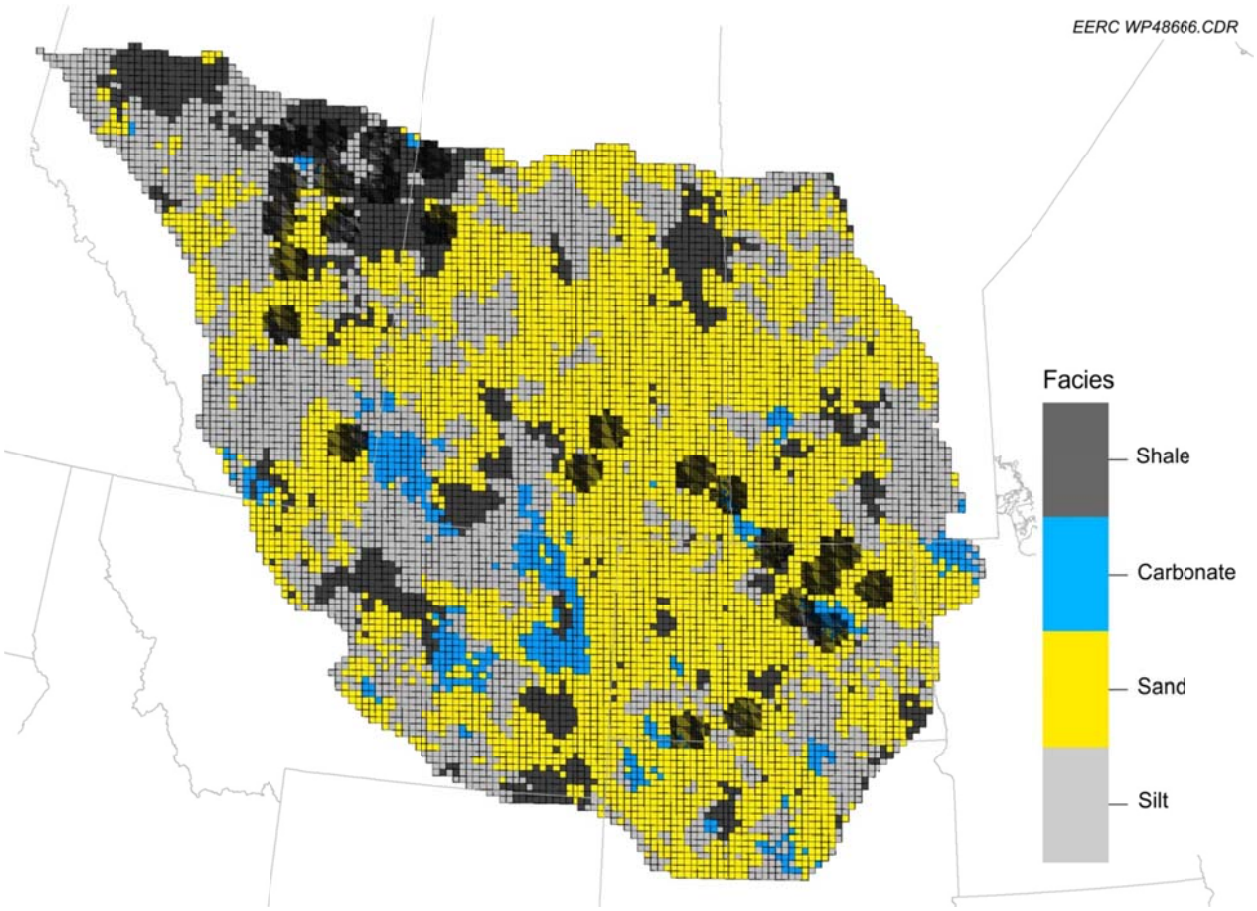

Figure 45. Location of the injection sites for Scenario 2 and the local grid refinement areas in black overlain on the facies property.

In Scenario 2, a total of eight new cases are simulated based on the new injection cluster locations. Varying strategies in this scenario include high and low rock compressibility, adding water extraction around the injectors, and converting the vertical injectors to horizontal. Geologically, rock compressibility cannot be changed, but in this study, the low and high values of the rock compressibility range in the study area were brought into the simulation to explore how much effect would be on the CO_2 storage capacity. Each case was then simulated to determine the fate of ~104 Mt of annual CO_2 capture. A total of 100 years is simulated including 50 years of injection plus 50 years of postinjection to monitor the pressure transient. A total of 211 injection wells were utilized in each case with an annual average injection target of 500,000 ton/yr over the 50-yr time frame for a total injection target of 5200 Mt.

Cases 1 and 2

Cases 1 and 2 are designed to test the effect of rock compressibility on the CO_2 injection for a vertical injection pattern. Case 1 results in a total injected mass CO_2 of 1949 Mt, which is 37.5% of the emissions with a low value of rock compressibility. This amount is a large change in comparison to any case of Scenario 1, because moving the injection clusters to "better" areas

improved the overall CO_2 injection. However, based on these results, the per well annual injection was only about 185,000 ton/yr. At these injection rates, about 563 wells would have been needed to reach the injection target of 5200 Mt.

Case 2 compares the impact on CO_2 storage by using a formation with a high rock compressibility value. High rock compressibility results have a large effect on the total amount of CO_2 storage. The total amount of mass stored in Case 2 increased to 2795 Mt which is 16.3% more than Case 1. Even with this increase, the per well annual injection rate is only about 265,000 ton/yr and would require 392 wells spread out even further to meet the injection target.

Cases 3 and 4

Cases 3 and 4 build upon Cases 1 and 2. For each case, 163 water extraction wells are added around the vertical injectors to increase the volume and maintain the reservoir pressure for CO_2 injection. Case 3 has the low rock compressibility value, and Case 4 has the high value. Case 3 injected 2644 Mt compared to 1949 Mt from Case 1, and Case 4 injected 3042 Mt compared to 2795 Mt in Case 2. This shows that water extraction can play a significant role in CO_2 injection. However, water extraction will play a more significant role if rock compressibility is low. In addition, it may be more effective to use those 163 extractors as injectors in other areas to increase the total storage even higher. Based on the Case 1 results, adding an additional 163 injectors may have added 1508 Mt of storage or 3457 Mt (66.5%) of the target mass. The increase in the high-rock-compressibility case may have been much more pronounced with 374 injectors potentially storing 95% of the target volume based on Case 2 per well injection rates.

Cases 5 and 6

Cases 5 and 6 were designed to test the effects of horizontal injection in comparison to vertical injection in Cases 1 and 2. For both cases, all vertical injection wells are converted to horizontal injectors (7000 ft long) to enhance more CO_2 injection without water extraction. Case 5 has the low rock compressibility value, and Case 6 has the high value. The change from vertical to horizontal injectors does not have a large impact on the amount of CO_2 injected. Case 5 injected a total of 2039 Mt compared to 1949 Mt in Case 1, and Case 6 injected 2899 Mt compared to 2795 Mt in Case 2. Both cases increased injection about 2%.

Cases 7 and 8

Cases 7 and 8 include both water extraction and horizontal injection. With low and high rock compressibility in Cases 7 and 8, total injected CO_2 for Cases 7 and 8 were 2695 and 3111 Mt, respectively.

Summary of Scenario 2

The large difference between Scenarios 1 and 2 included the movement of the injection clusters to areas where high permeability values were connected in the geocellular model and distributed 16 injection clusters to 25 injection locations. Rock compressibility, water extraction

at each injection cluster, and conversion of vertical injectors to horizontal are also sensitive parameters in determining the amount of injected CO_2. These variables for each case were changed to help optimize injection and determine the effect on the overall storage capacity. Table 5 presents the results and the parameters used in each case of this scenario.

The largest effects that helped increase CO_2 injection in this scenario are the rock compressibility values, added water extraction at each site, and moving the injection locations to "better" locations (Figure 44). Each of these parameters was combined in Case 8, which injected 59.8% of the overall emissions from large CO_2 sources of the study area (Figures 46 and 47). This case gave the most optimal injection scenario over a 50-year injection period than others.

Based on the results of Scenario 2, the selection of areas with better permeability and connected volume had a large impact on increasing the total amount of CO_2 stored and the per well injection rates. However, even in the better area, the COSS was not able to support 211 injection wells with an average annual injection rate of 0.5 Mt/yr. In Scenario 2, the average annual per well injection rate was between 185,000 to 275,000 ton/yr with horizontal wells. At these average injection rates, a total of 378 to 563 wells would have been required to meet the injection target.

Discussion of the Two Scenarios

Reservoir heterogeneity plays a crucial role in overall CO_2 injection. The basal saline system has ideal characteristics but relies on optimal operations which selected the "better" geologic injection location to sink the total emitted CO_2. The two different scenarios did not reach the total output of the CO_2 emissions because of the limited number of wells and injection clusters. Problems of injection occur for Scenario 1 because of the location of the initial injection clusters over areas of poor geologic conditions such as areas of low permeability and porosity and disconnected volumes. Scenario 2 increased injectivity after the injection clusters were moved to areas of "better" geologic properties and distributed nine more injection clusters based on Scenario 1 to reach 59.8% of the total CO_2 emissions. Figure 48 shows the results and comparisons of each case for both scenarios.

The most optimal case in Scenario 1, Case 6, had the best CO_2 injection by using a stepwise injection approach and water extraction in the Duffield–Warburg area. This optimal case injected 1411.61 Mt of CO_2 over a 50-year period which is 28.4% of the annual emissions in the region. The results of Scenario 2 for each separate injection cluster had mixed results where some sources were able to inject most of the emissions and some very little (Appendix B). Regions that injected little amounts of the emitted CO_2 are areas where the reservoir started to thin and had areas of lower Kh (mD*ft) even with high permeability in the connected volume (Figure 49). Results of Scenario 2 would be more optimistic with increasing better injection locations and the number of injectors and adding water extractors around the injectors for the total amount of emitted CO_2.

Table 5. Results of the Simulation Cases of Scenario 2 (columns display the parameters for each case, the total amount of CO_2 injected, and percentage of the total large-scale emissions in the study area)

Case	Total Injectors	Total Extractors	Years of Injection	Postinjection, years	Water Extraction	Horizontal Injection	Rock Compressibility	Total Injected CO_2, Mt	Injected, CO_2, %
1	211	No	50	36	No	No	Low	1949	37.5
2	211	No	50	36	No	No	High	2795	53.8
3	211	163	50	36	Yes	No	Low	2644	50.8
4	211	163	50	36	Yes	No	High	3042	58.5
5	211	No	50	36	No	Yes	Low	2040	39.2
6	211	No	50	36	No	Yes	High	2899	55.8
7	211	163	50	36	Yes	Yes	Low	2695	51.8
8	211	163	50	36	Yes	Yes	High	3112	59.8
Expected Total CO_2 Injection for All of the Emission Resources over 50 years								5200	100

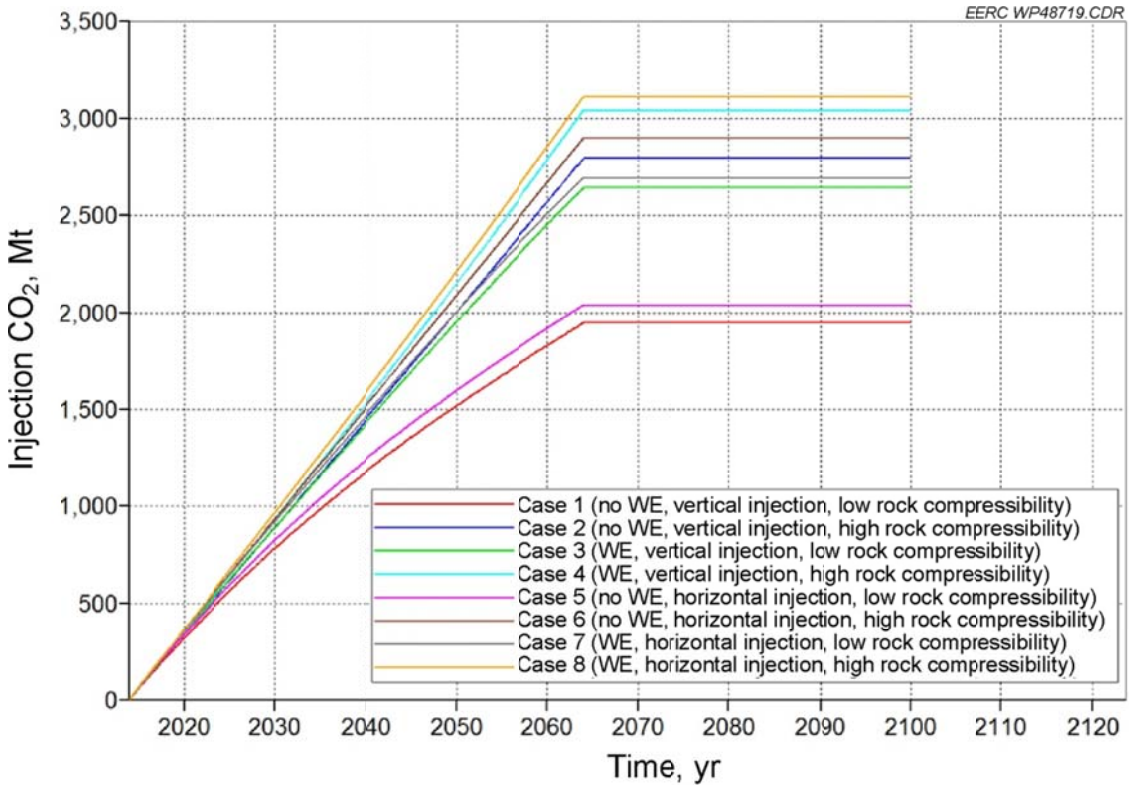

Figure 46. Overall injection history of cases for 50-year injection period. The different cases show the impact the different variables have on the overall CO_2 injection.

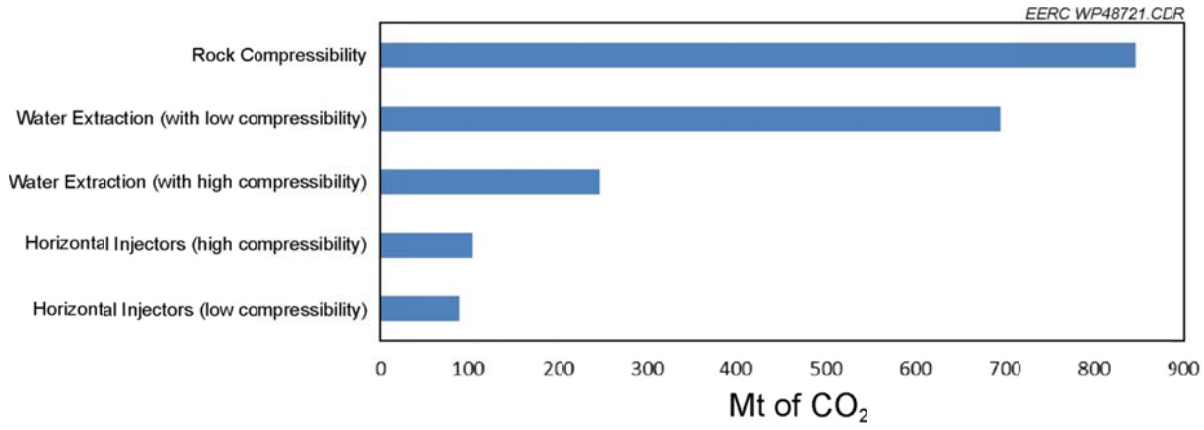

Figure 47. The adjustment of the variables used in Scenario 2 shows the overall effect on the total amount of injected CO_2.

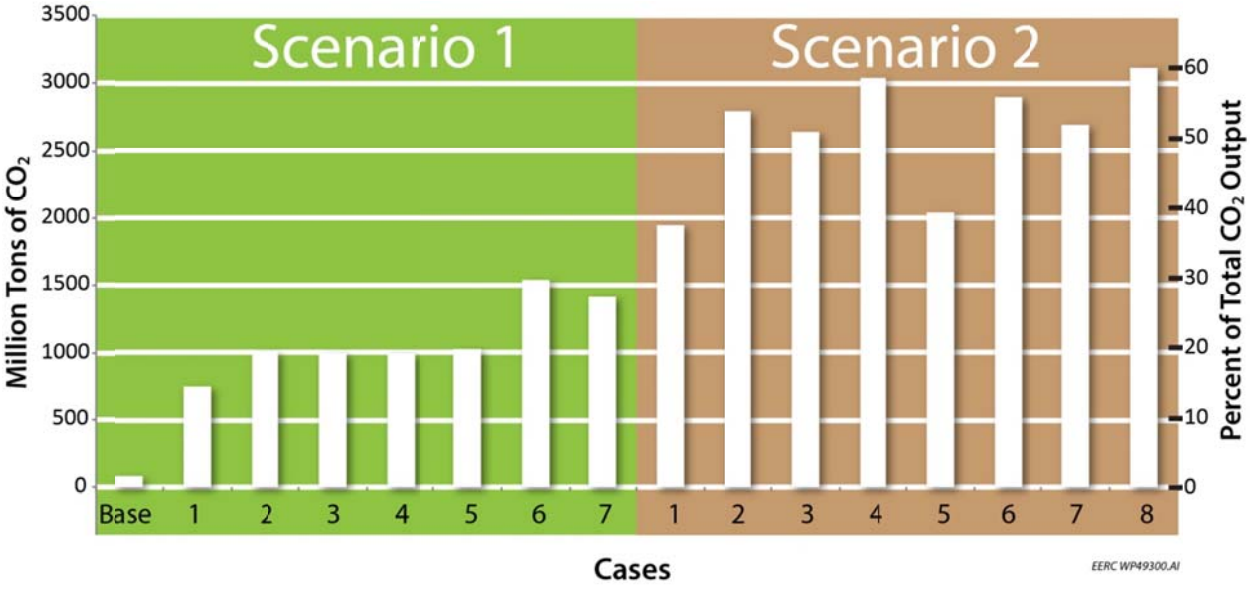

Figure 48. Cases are compared between Scenarios 1 and 2. The best simulation results in this study occurred in Scenario 2, with the inclusion of "better" geology and optimal operations.

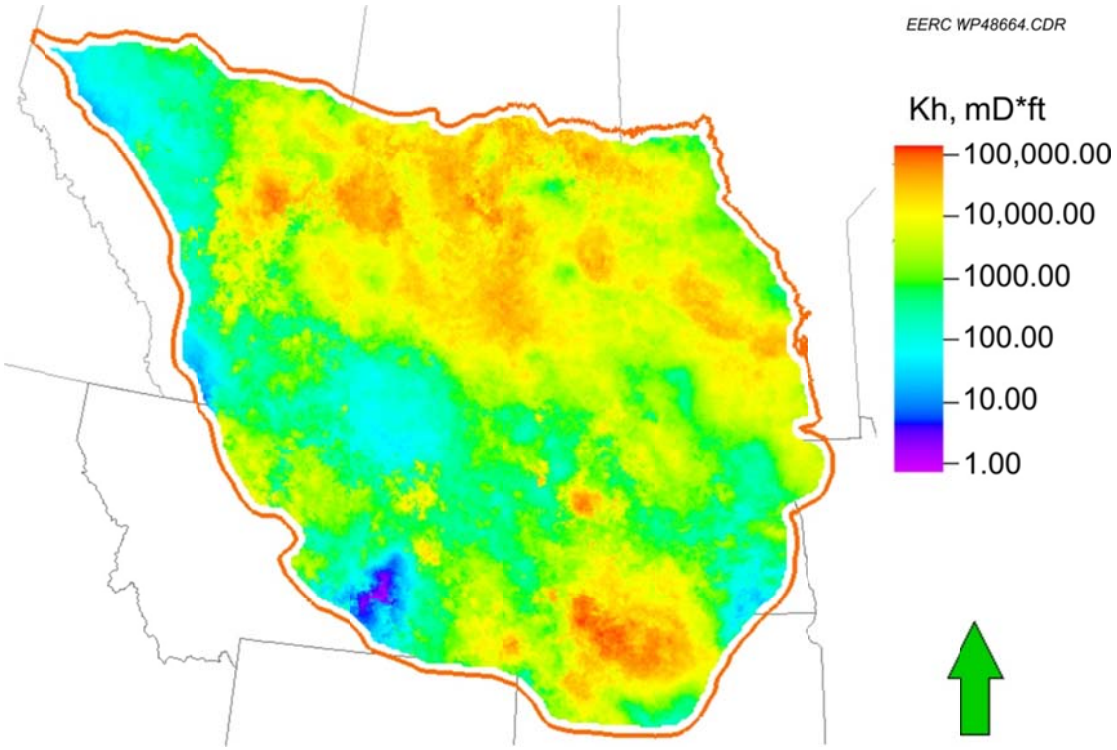

Figure 49. Kh (mD*ft) map of the basal saline system.

Pressure differences were monitored in the simulation during the 50-year injection period and a 36-year postinjection period for Scenario 2. Monitoring the pressure differences help determine associated risks with long-term storage in the basal saline system. Results on the pressure differences for each case in Scenario 2, found in Appendix C, show small changes over a 36-year time frame. These minimal pressure differences indicate small risks of leakage from the reservoir and integrity of the sealing cap rock due to CO_2 injection in the basal saline aquifer system.

The basal saline system should be considered an overall target formation for CO_2 sequestration with 412 Gt of calculated static storage capacity at a 9.1% efficiency factor. A static storage mass was calculated for areas only suitable for CO_2 storage. Areas suitable for storage exist where a suitable cap rock occurs and injection is in areas where TDS is greater than 10,000 ppm.

Reservoir quality and heterogeneity play a large role in the injection process. Moving the injection clusters to more optimal geology helped inject larger amounts of CO_2 in the basal saline system. Moreover, increasing the number of injectors and adding water extractors around the injectors could be the primary option to increase the injectivity and, ultimately, the total amount of injected CO_2 from emission sources rather than changing Kv/Kh ratio, using horizontal wells, and tracking residual water/gas.

Rock compressibility shows an important role for reservoir pressure transient regarding storage capacity for the cases without water extraction. This effect is reduced by adding water extraction because of the balance of the injection and production in the system. It means that selecting the injection location with high rock compressibility could be a better choice for more CO_2 injection than these locations with low rock compressibility.

The reservoir pressure in all of the cases with water extraction is lower than the cases without water extraction. This means that water extraction could play a significant role in reservoir management and risk assessment.

STATIC CO_2 STORAGE RESOURCE VS. DYNAMIC CO_2 STORAGE CAPACITY

The static CO_2 storage resource potential was estimated to be approximately 218, 412, and 706 Gt at the P10, P50, and P90 confidence intervals. With this amount of storage potential, the COSS should be able to store between 2100 and 6780 years of the current 104 Mt/yr of point source CO_2 emissions from the overlying sources. Based on this calculation, it should seem relatively straightforward to store 104 Mt/yr for 36 or 50 years, resulting in a total storage of 3744 or 5200 Mt, respectively. However, when different cases were designed to simulate the injection and storage into the COSS, no cases were run where this total goal was met. In each case, injectivity was a limiting factor, and in all cases, many more wells would have been required to meet the storage target. The postsimulation analysis reveals that to inject and store 104 Mt/yr of CO_2 for 50 years (5200 Mt) in the COSS, a total of 378 to 1050 wells would have been required, instead of the 210 or 211 wells that were simulated. This would require dispersing the CO_2 to a greater number of injection areas than the 25 that were simulated.

To increase the total stored mass of CO_2, it may be more effective to use additional injection wells across a broader area rather than a blending of injection and water extraction wells in a more confined extent. For example, if the 163 water extraction wells in Cases 3 and 4 of Scenario 2 were, instead, 163 injectors in another region of the COSS, and an additional 1508 to 3457 Mt of storage could be obtained, resulting in nearly 66% of the target storage value. The increase in stored CO_2 in the high-rock-compressibility case of Scenario 2 may have been much more pronounced, with 374 injectors potentially storing 95% of the target storage mass based on Case 2 per well injection rates.

In a comparison of the total static CO_2 resource value for the 25 injection areas of Scenario 2 to the high and low case injection totals in the dynamic simulations, only a relatively small fraction of the total capacity was used (Table 6). However, it should be noted that this does not imply that the efficiency factors used in this investigation are inaccurate. The dynamic simulations in Scenario 2 were only run for 50 years, and for a majority of the cases, the slope of the injection rate was constant across that time period. The steady injection rate indicates that the COSS was still accepting CO_2 and the true dynamic capacity had not yet been reached.

CONSIDERATIONS AND FUTURE WORK

The COSS static geocellular model was built with limited amounts of data for the size of the region it encompasses. This limited amount of data results in relatively high uncertainty in areas where wells do not exist. This is especially true near most of the clusters used in the dynamic simulations. The model was built with one statistical realization which can result in optimal geologic conditions being predicted for one emission source over another. This does not necessarily mean the geology is, in reality, optimal (or poor) at that CO_2 source, but that multiple realizations should be performed to bolster the statistical significance of the geologic prediction. It should also be noted that because of the broad-scale coarseness of this model, it should not be used for site-specific planning of a commercial CO_2 storage project.

The explorations with more injectors and extractors need to be investigated for the amount of CO_2 from emission sources. All expected CO_2 from resources may be injected with more wells (injectors and extractors), especially in areas with better Kh (thick, connected, high-permeability). Moreover, the fine-scale model with much focus on local injection areas for specific CO_2 emission sources may provide detailed insights of storage potential. In addition, geomechanical, geochemical, and geothermal behaviors need to be integrated throughout the entire modeling and simulation process to investigate the role of these variables in the overall storage estimation.

Table 6. Static versus Dynamic Capacity (Gt) for Scenario 2 Injection Locations

Total	Static Resource After Efficiency Factor Applied			Dynamic Capacity	
Resource	P10	P50	P90	Low	High
107.6	7.9	15.0	25.8	1.9%	3.1%

CONCLUSIONS

A binational effort between the United States and Canada successfully characterized the COSS in the Williston and Alberta Basins of the northern Great Plains–Prairie region of North America in the United States and Canada. Through this characterization process, an extensive 3-D geocellular model of the system was constructed for the purpose of determining the static CO_2 capacity and to serve as the foundation for dynamic simulation. The resulting static storage capacity of 218, 412, and 706 Gt at the P10, P50, and P90 percentiles reflect the application of storage efficiency values of 4.8%, 9.1%, and 15.6%, respectively, for clastic reservoirs. At the current emission rate of approximately 104 Mt/yr for the large-scale CO_2 sources in the region, the static capacity represents thousands of years of storage.

Two scenarios were investigated to determine the feasibility of injecting a total of 104 Mt from the 25 large stationary sources overlying the COSS. The first injection scenario considered seven cases where the target was to inject this total mass of CO_2 for 36 or 50 years in 16 injection areas using a total of 210 wells. The number of wells is based on an assumed per well injection rate of ~0.5 Mt/yr. Results from these cases show a total mass of CO_2 injected ranging from 82 to 1412 Mt across the injection period of 36 and 50 years. These values represent between 2.2% and 27.2% of the available CO_2 emitted from the 16 source locations. The second scenario investigated eight new cases where the original 16 injection locations were disaggregated and moved (pipelined) to areas defined by the model as having good reservoir volume connection (geobodies) based on permeabilities greater than 50 mD. Injection amounts in the second scenario range from 1949 to 3112 Mt of CO_2. These values represent 37.5% to 59.8% of the CO_2 emitted from the source locations. Based on the results of both scenarios, the selection of areas with better permeability and connected volume had a large impact on increasing the total amount of CO_2 stored and the per well injection rates. However, even in the better area the COSS was not able to support 211 injection wells with an average injection rate of 0.5 Mt/yr. In the second scenario, the average annual per well injection rate was between 185,000 and 275,000 tons/yr. At these injection rates, a total of 378 to 563 wells would have been required to meet the injection target. Pressure differences monitored in the second scenario show small changes in the 50-year injection time period. These minimal pressure differences indicate low risks of leakage from the reservoir and impact to the integrity of the sealing cap rock as a result of CO_2 injection in the COSS. Although this broad-scale study should not be used for site-specific interpretation, the COSS should be considered as a large-scale viable target for CO_2 storage across the central interior of North America.

ACKNOWLEDGMENTS

The authors would like to acknowledge Dr. Stefan Bachu of Alberta Innovates for initiating the international effort to investigate this extensive saline system. Recognition is also extended to the geological surveys and oil and gas regulatory agencies of North Dakota, South Dakota, Montana, Alberta, Saskatchewan, and Manitoba for their contribution of data. In addition, guidance and support of this effort from members of the PCOR Partnership Technical Advisory Board have been greatly appreciated.

REFERENCES

AAPG, American Association of Petroleum Geologists, CSDE, COSUNA, and Geothermal Survey Data_Rom, 1994, provided by SMU Geothermal Laboratory, 2012.

Bachu, S., and Adams, J.J., 2003, Sequestration of CO_2 in geological media in response to climate change—capacity of deep saline aquifers to sequester CO_2 in solution: Energy Conversion and Management, v. 44, no. 20, p. 3151–3175.

Bachu, S., Faltinson, J., Hauck, T., Perkins, E., Peterson, J., Talman, S., and Jensen, G., 2011, The basal aquifer in the Prairie region of Canada—characterization for CO_2 storage: Preliminary report for Stage I (Phases 1 and 2), Alberta Innovates Technology Futures.

Barnes, D.A., Bacon, D.H., and Kelley, S.R., 2009, Geological sequestration of carbon dioxide in the Cambrian Mount Simon sandstone—regional storage capacity, site characterization, and large-scale injection feasibility, Michigan Basin: Environmental Geosciences, v. 16, no. 3 (September 2009), p. 163–183.

Bell, L.H., 1970, Depositional history of the Cambrian Flathead sandstone, Park County, Wyoming: Guidebook – Wyoming Geological Association, v. 22, p. 115–131.

Bennion, B., and Bachu, S., 2005, Relative permeability characteristics for supercritical CO_2 displacing water in a variety of potential sequestration zones in the Western Canada Sedimentary Basin: SPE Paper 95547, SPE Annual Technical Conference and Exhibition, Dallas, Texas, USA, October 9–12, 2005.

Blackwell, D. and Richards, M., 2004, Geothermal map of North America: AAPG map, scale 1:6,500,000, Product Code 423.

Blackwell, D., Richards, M., and Stepp, P., 2010, Texas geothermal assessment for the I35 corridor east: Final Report, Texas State Energy Conservation Office Contract CM709, p. 88.

Bradshaw, J., Bachu, S., Bonijoy, D., Burruss, R., Holloway, S., Christensen, N.P., and Mathiassen, O.M., 2007, CO_2 storage capacity estimation—issues and development of standards: International Journal of Greenhouse Gas Control, v. 1, p. 62–68.

Carbon Sequestration Leadership Forum, 2007, Estimation of CO_2 storage capacity in geological media: June 2007, 43 p.

Carlson, C.G., and Thompson, S.C., 1987, Stratigraphy of the Deadwood Formation and Winnipeg Group in the Williston Basin, Williston Basin—anatomy of a cratonic oil province: Rocky Mountain Association of Geologists, Symposium on the Williston Basin, p. 71–80.

Crowell, A., and Gosnold, W., 2011, Correcting bottom-hole temperatures—a look at the Permian Basin (Texas), Anadarko and Arkoma Basins (Oklahoma) and Williston Basin (North Dakota): Geothermal Resources Council Transactions, v. 35, p. 735–738.

Downey, J.S., and Dinwiddie, G.A., 1988, The regional aquifer system underlying the northern Great Plains in parts of Montana, North Dakota, South Dakota, and Wyoming—summary: U.S. Geological Survey Professional Paper 1402–A, p. A1–A64.

Ferguson, G.A.G., Betcher, R.N., and Grasby S.E., 2007. Hydrogeology of the Winnipeg Formation in Manitoba, Canada: Hydrogeology Journal, v. 15, p. 573–587, doi:10.1007/ s10040-006-0130-4.

Gorecki, C.D., Sorensen, J.A., Bremer, J.M., Knudsen, D.J., Smith, S.A., Steadman, E.N., and Harju, J.A., 2009, Development of storage coefficients for determining the effective CO_2 storage resource in deep saline formations: SPE Paper 126444, SPE International Conference on CO_2 Capture, Storage, and Utilization, San Diego, November 2–4, 2009.

Goodman, A., Hakala, A., Bromhal, G., Deel, D., Rodosta, T., Frailey, S., Small, M., Allens, D., Romanov, V., Fazio, J., Huerta, N., McIntyre, D., Kutchko, B., and Guthrie, G., 2011, U.S. DOE methodology for the development of geologic storage potential for carbon dioxide at the national and regional scale: International Journal of Greenhouse Gas Control, v. 5, p. 952–965.

Gosnold, W., Lefever, R., Mann, M., Klenner, R., and Salehfar, H., 2010, EGS potential in the northern midcontinent of North America: Geothermal Resources Council Transactions, v. 34, p. 355–358.

Griffith, A., and Nichols, N., 1996, Accounting for model error in data assimilation using adjoint methods, *in* Computational differentiation: Techniques, Applications and Tools, Proceedings.

Harrison, W.E., Luza, K.V., Prater, M.L. and Chueng, P.K., 1983, Geothermal resource assessment of Oklahoma: Oklahoma Geological Survey, Special Publication 83-1.

Hutchinson, M., 1989, A stochastic estimator of the trace of the influence matrix for Laplacian smoothing splines: Communication in Statistics – Simulation and Computation, v. 19, no. 2, p. 433–450.

Intergovernmental Panel on Climate Change, 2005, Special report on carbon dioxide capture and storage: Cambridge University Press, Cambridge, United Kingdom, and New York.

Kent, D.M., 1987, Paleotectonic controls on sedimentation in the northern Williston Basin, Saskatchewan Williston Basin—anatomy of a cratonic oil province: Rocky Mountain Association of Petroleum Geologists, p. 45–56.

LeDimet, F., Ngodock, H., and Navon I., 1995, Sensitivity analysis in variational data assimilation: Supercomputer Computations Research Institute Technical Report, FSU-SCRI-95T-103, The Florida State University, Tallahassee, Florida.

Leetaru, H.E., and McBride, J.H., 2009, Reservoir uncertainty, Precambrian topography, and carbon sequestration in the Mt. Simon sandstone, Illinois Basin: Environmental Geosciences, v. 16, p. 1–9, doi:10.1306/eg.08110808003.

LeFever, R.D., 1996, Sedimentology and stratigraphy of the Deadwood–Winnipeg interval (Cambro-Ordovician): Williston Basin, Society for Sedimentary Geology, Rocky Mountain Section, p. 11–28.

Macke, D.L., 1993, Cambrian through Mississippian rocks of the Powder River Basin, Wyoming, Montana, and adjacent areas: U.S. Geological Survey Bulletin 1917-M, M1-M174.

Murphy, E.C., Nordeng, S.H., Juenker, B.J., and Hoganson, J.W., 2009, North Dakota stratigraphic column: North Dakota Geological Survey, Miscellaneous Series 91.

National Institute of Standards and Technology Standard, 2003, Reference Database No. 69, March 2003, Linstrom, P.J., and Mallard, W.G., eds.

Nunn, J., Guichang, L., and Zhang, L., 1999, Thermal insulation by low thermal conductivity shales—implications for basin-scale fluid flow and heat transport, *in* Förster, A., and Merriam, D., eds., Geothermics in basin analysis: Kluwer, New York, p. 117–130.

Peck, W.D., Buckley, T.D., Battle E.P., and Grove, M.M., compilers and creators, 2013, Plains CO_2 Reduction (PCOR) Partnership atlas (4th ed., rev.): Prepared for the U.S. Department of Energy National Energy Technology Laboratory and the PCOR Partnership, Grand Forks, North Dakota, Energy & Environmental Research Center, 124 p.

U.S. Department of Energy Office of Fossil Energy, 2007, Carbon sequestration atlas of United States and Canada, 1st edition.

U.S. Department of Energy Office of Fossil Energy, 2008, Methodology for development of geologic storage estimates for carbon dioxide, 2nd edition.

U.S. Department of Energy Office of Fossil Energy, 2010, Carbon sequestration atlas of the United States and Canada, 3rd edition.

U.S. Department of Energy Office of Fossil Energy, 2012, Carbon sequestration atlas of the United States and Canada, 4th edition.

U.S. Environmental Protection Agency, 2012, http://water.epa.gov/ (accessed January 2012).

.

APPENDIX A

PROPERTIES OF THE BASAL CAMBRIAN AQUIFER SYSTEM

PROPERTIES OF THE BASAL CAMBRIAN AQUIFER SYSTEM

Table A-1. Permeability and Porosity Properties for the Aquifer and Different Lithologies

	Min. Perm.	Mean Perm.	Max. Perm	Std Dev. Perm.	Min. Porosity	Mean Porosity	Max. Porosity	Std. Dev. Porosity
Aquifer	0.01	24.8	3202	122	0.00	0.07	0.38	0.074
Sand	0.01	40	3202	120.7	0.01	0.11	0.38	0.080
Shale	0.001	1.4	2	0.7	0.00	0.01	0.15	0.004
Carbonate	0.003	0.3	37	1.7	0.00	0.02	0.27	0.031
Silt	0.01	14	53	68	0.00	0.06	0.28	0.050

Table A-2. Variogram Properties for the Geocellular Model

Variogram	Vertical	Max.	Min.	Max. Dir.	Min. Dir.
Shale	123	1,845,219	1,626,989	140	50
Carbonate	174	621,785	326,831	140	50
Sand	156	1,778,645	1,326,341	140	50
Silt	173	357,010	327,708	140	50
Porosity and Permeability	97	1,440,000	1,440,000	N/A	N/A

APPENDIX B

INJECTION RESULTS FOR SCENARIO 2 (CASES 1–8)

INJECTION RESULTS FOR SCENARIO 2 (CASES 1–8)

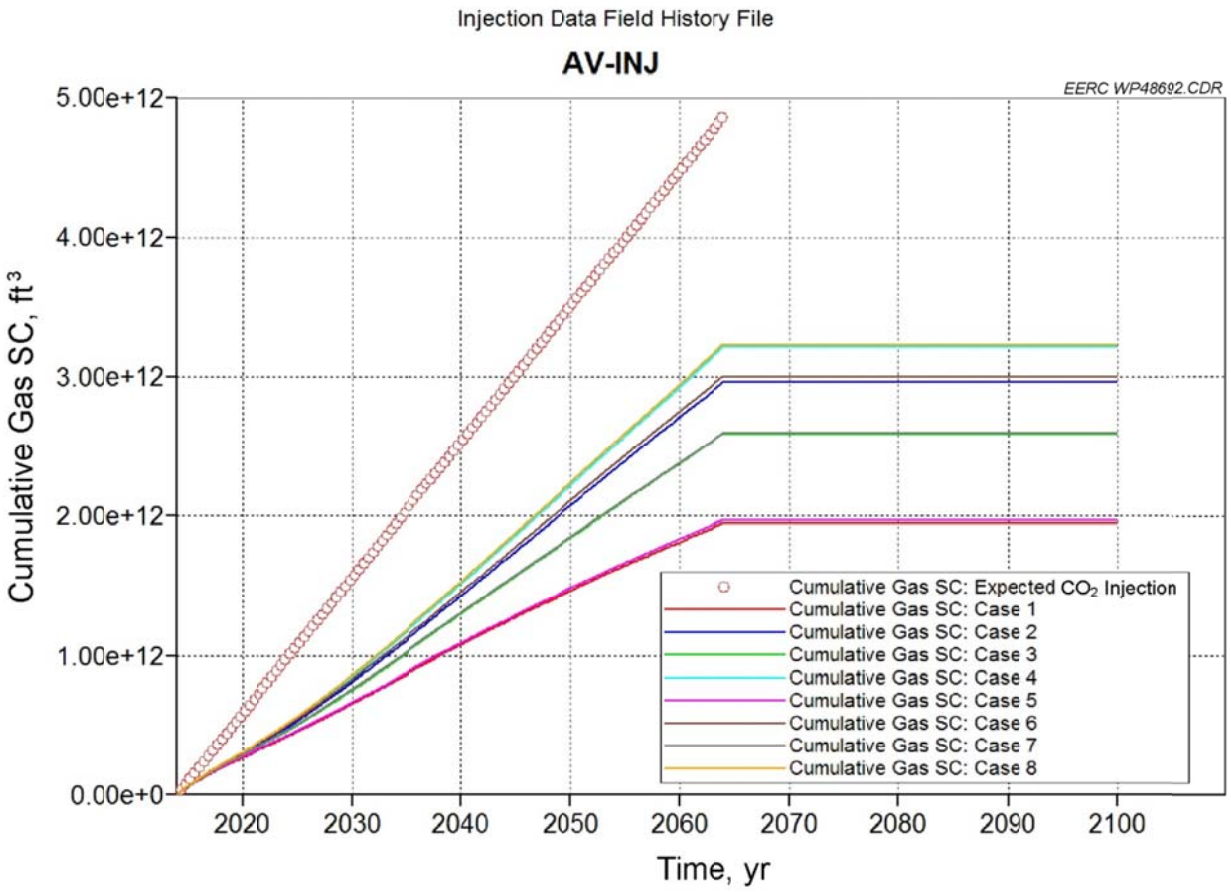

Figure B-1. Cumulative injection and expected injection at Antelope Valley for Cases 1–8 of Scenario 2.

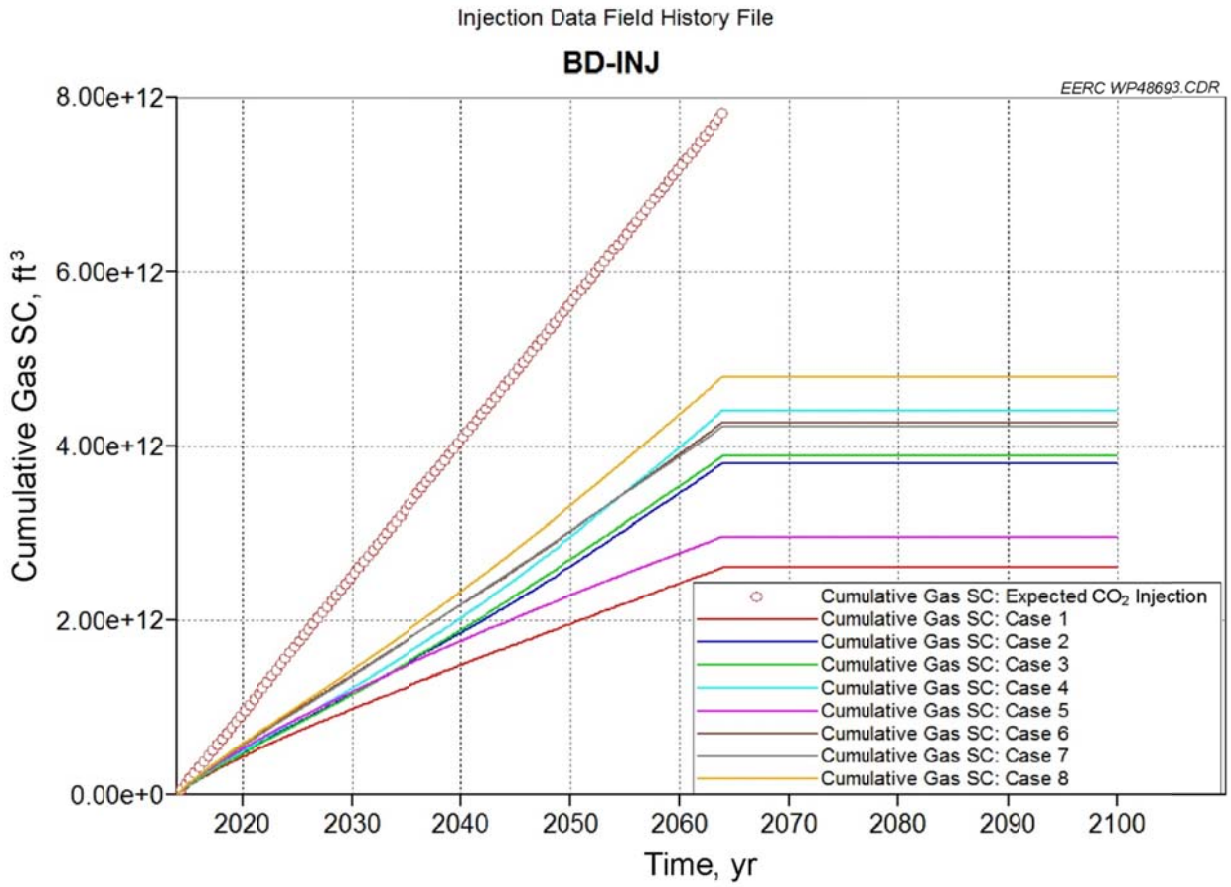

Figure B-2. Cumulative injection and expected injection at Boundary Dam for Cases 1–8 of Scenario 2.

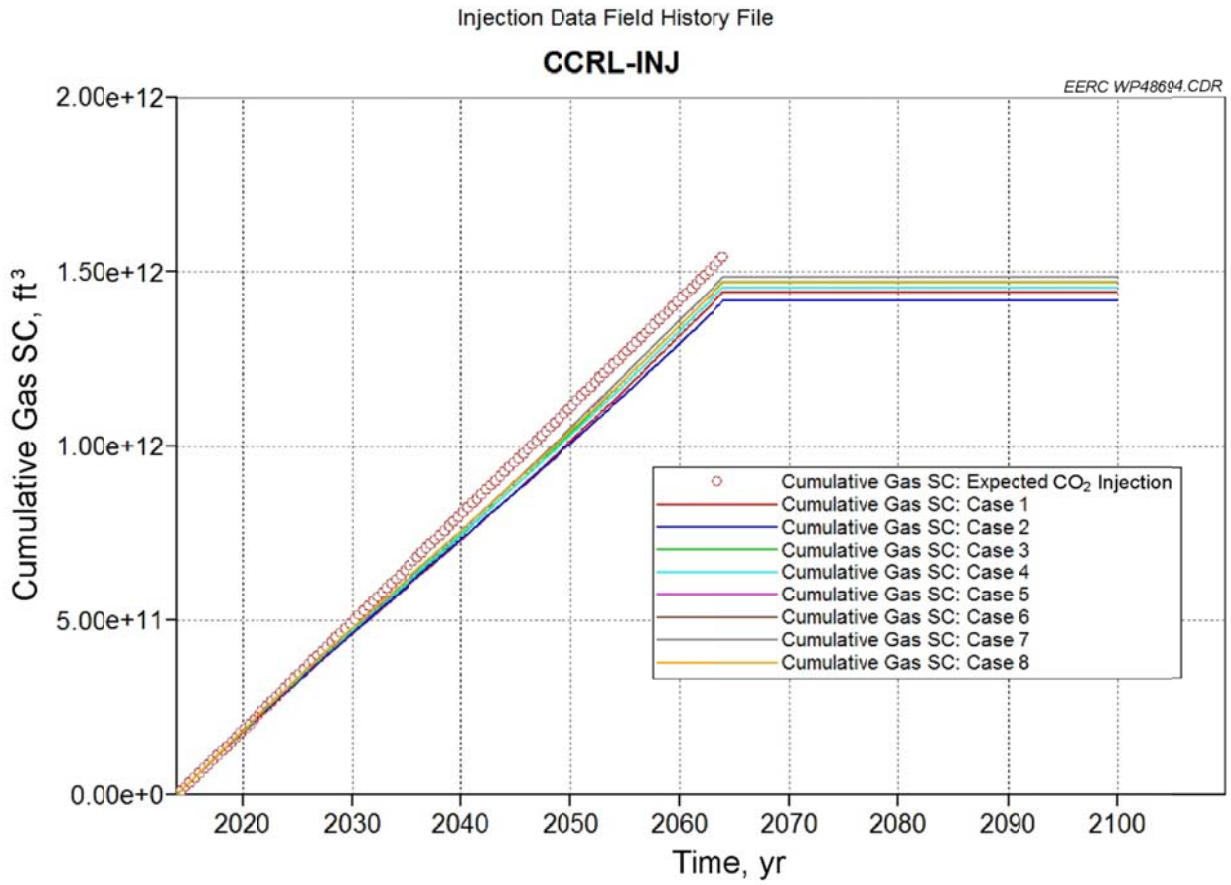

Figure B-3. Cumulative injection and expected injection at CCRL/NEI Refinery – Upgrader Complex for Cases 1–8 of Scenario 2.

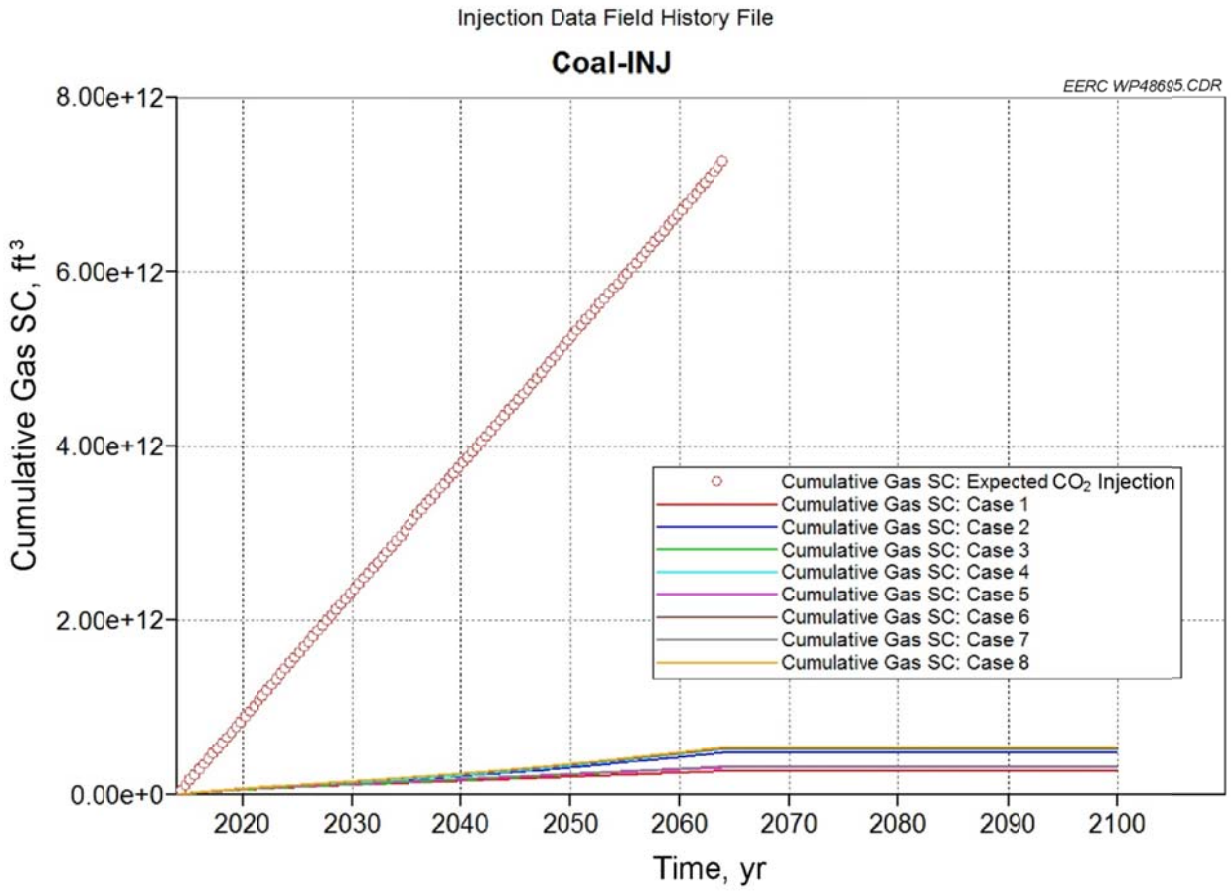

Figure B-4. Cumulative injection and expected injection at Coal Creek for Cases 1–8 of Scenario 2.

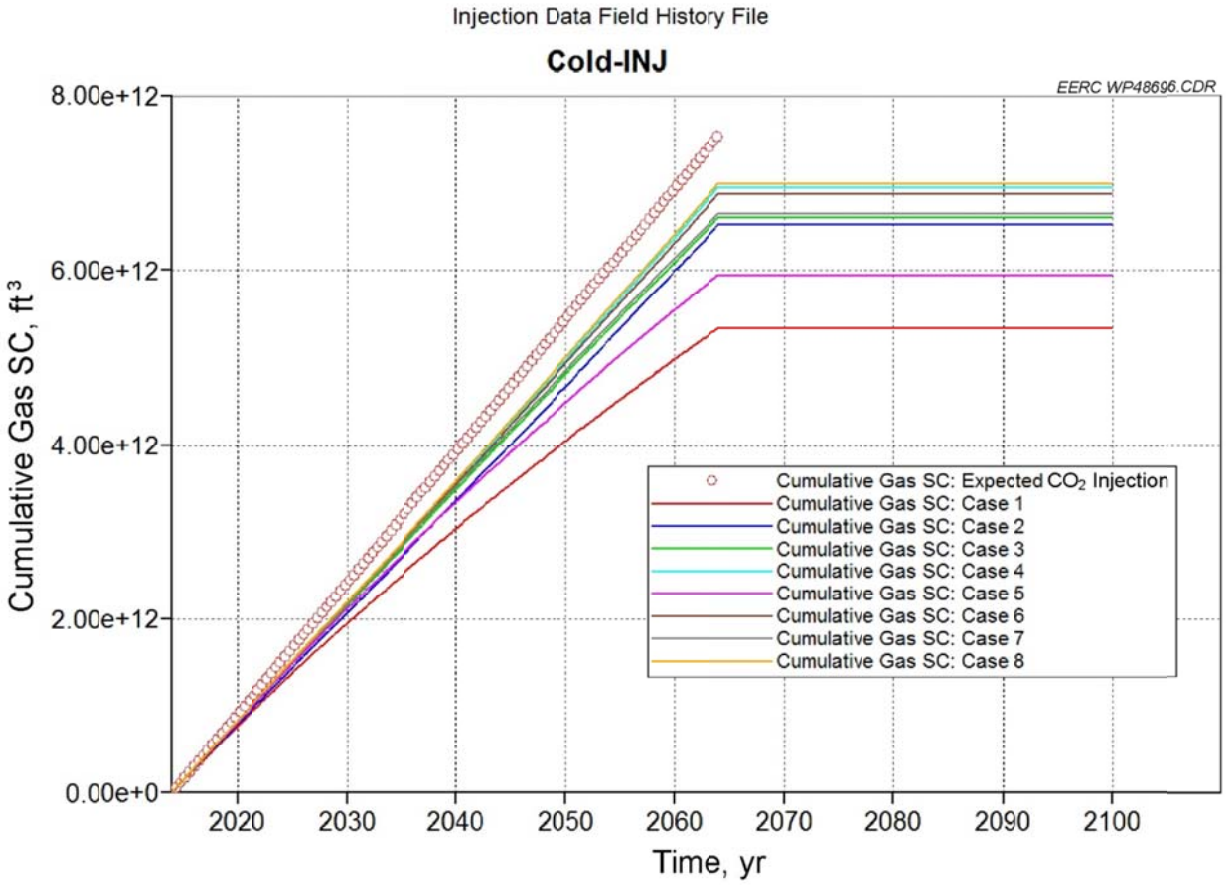

Figure B-5. Cumulative injection and expected injection at Cold Lake–Bonnyville for Cases 1–8 of Scenario 2.

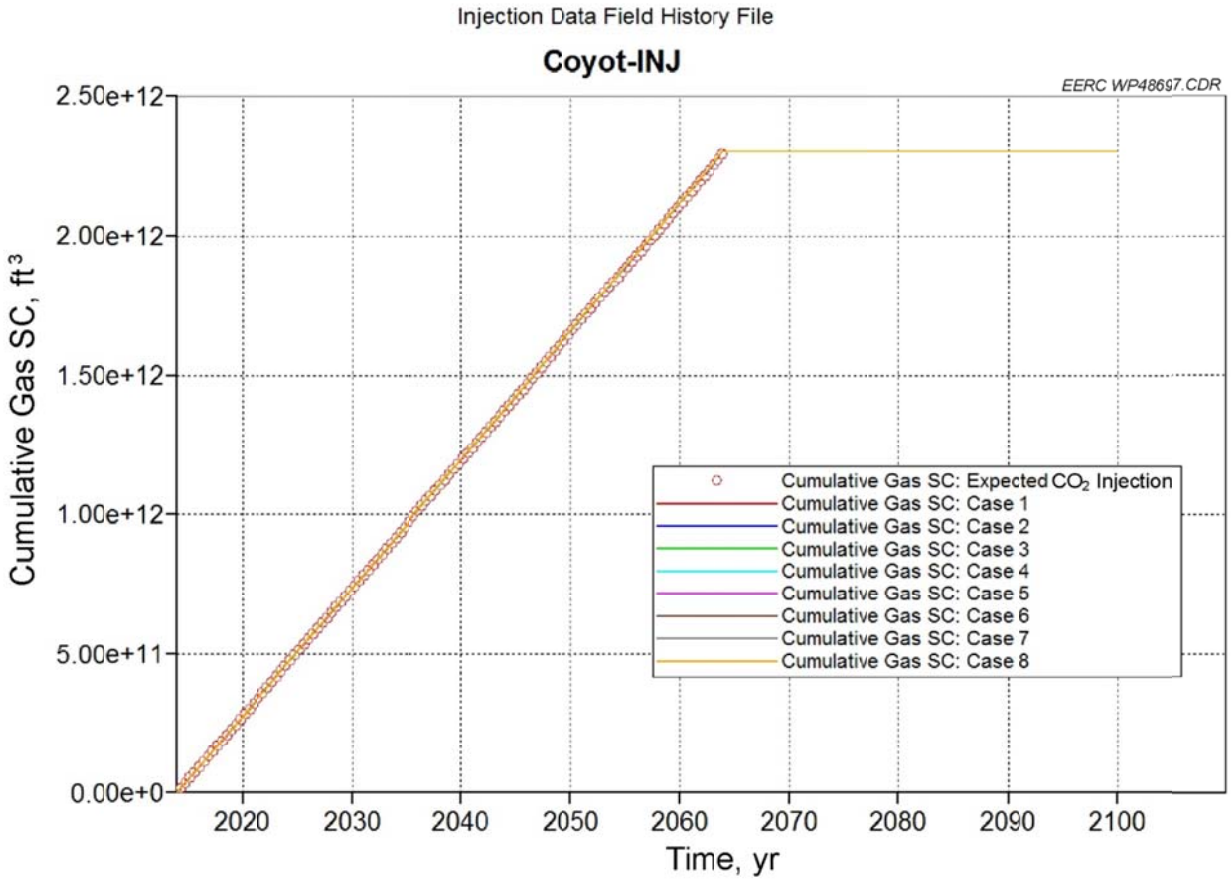

Figure B-6. Cumulative injection and expected injection at Coyote for Cases 1–8 of Scenario 2.

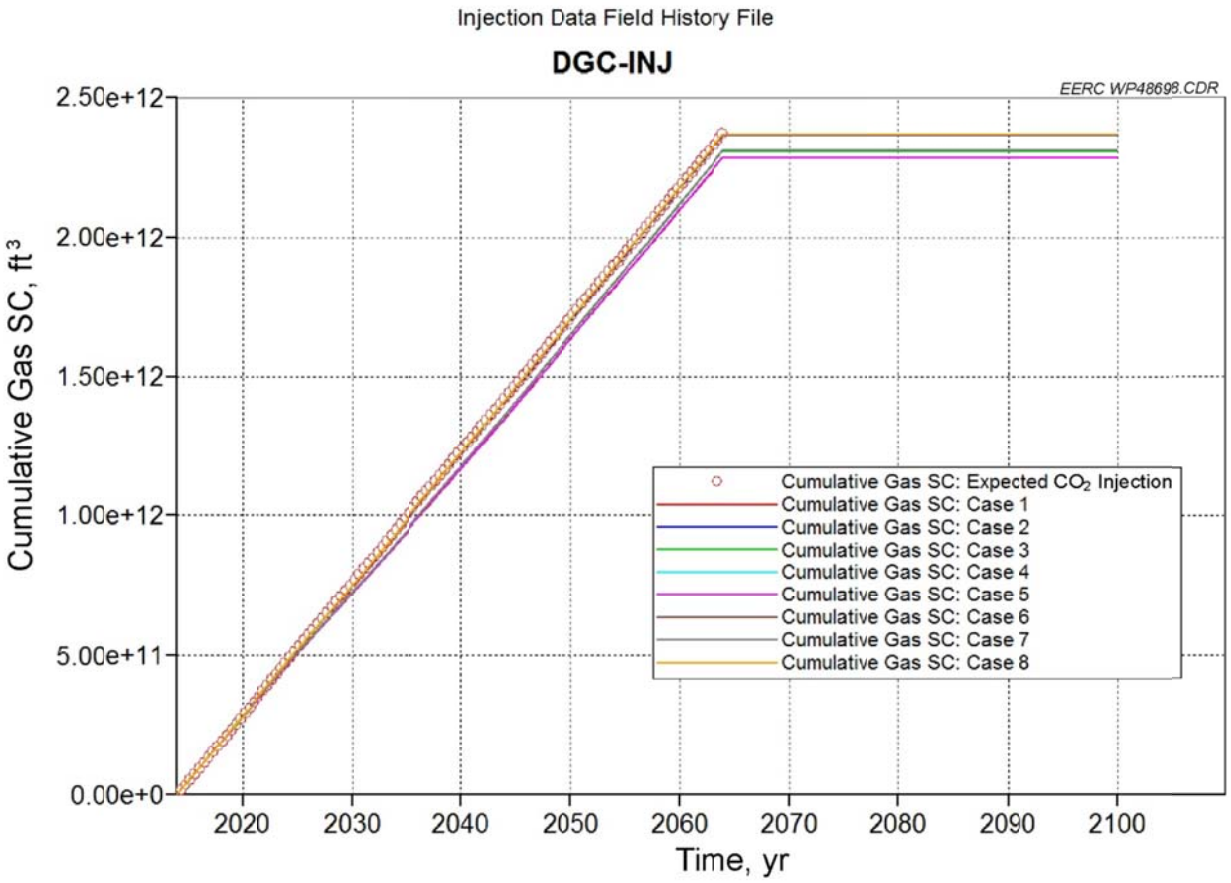

Figure B-7. Cumulative injection and expected injection at Dakota Gasification Company for Cases 1–8 of Scenario 2.

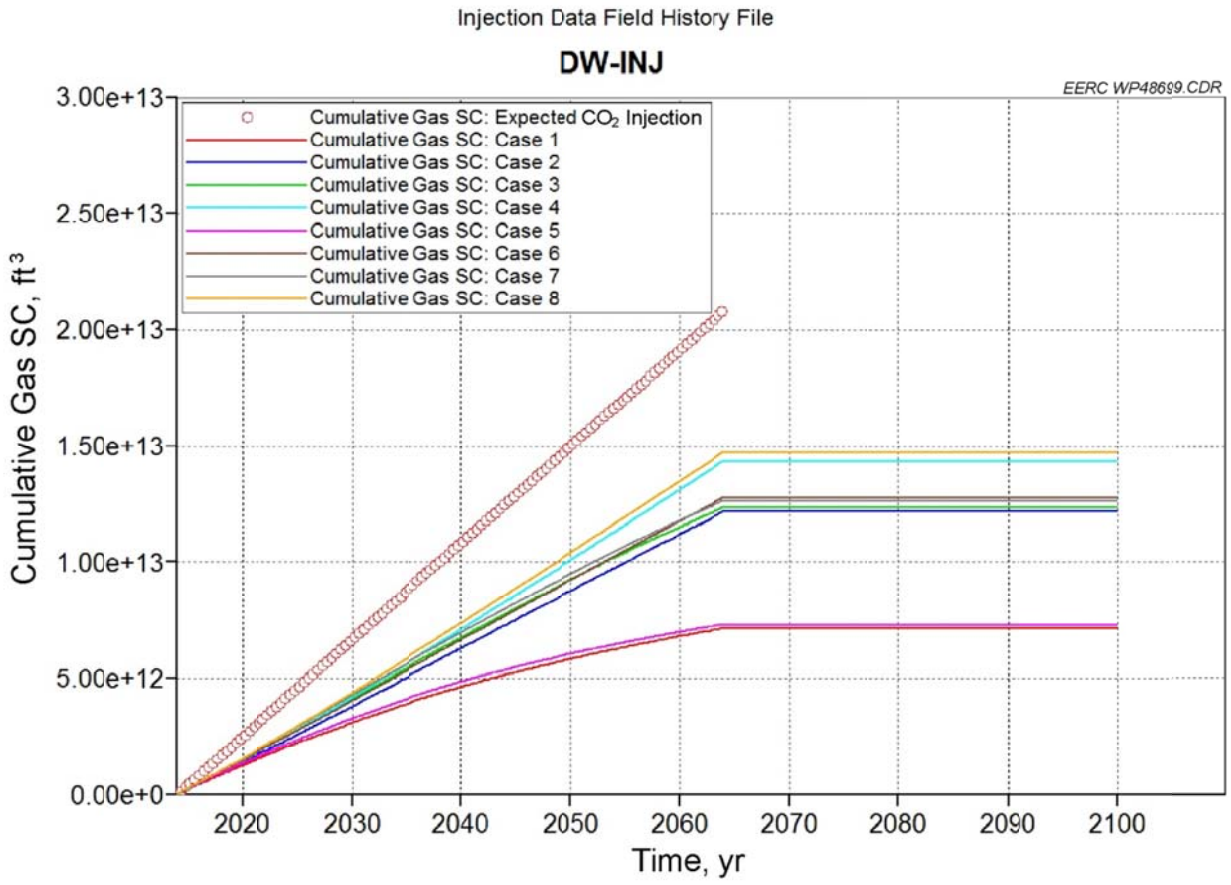

Figure B-8. Cumulative injection and expected injection at Duffield–Warburg for Cases 1–8 of Scenario 2.

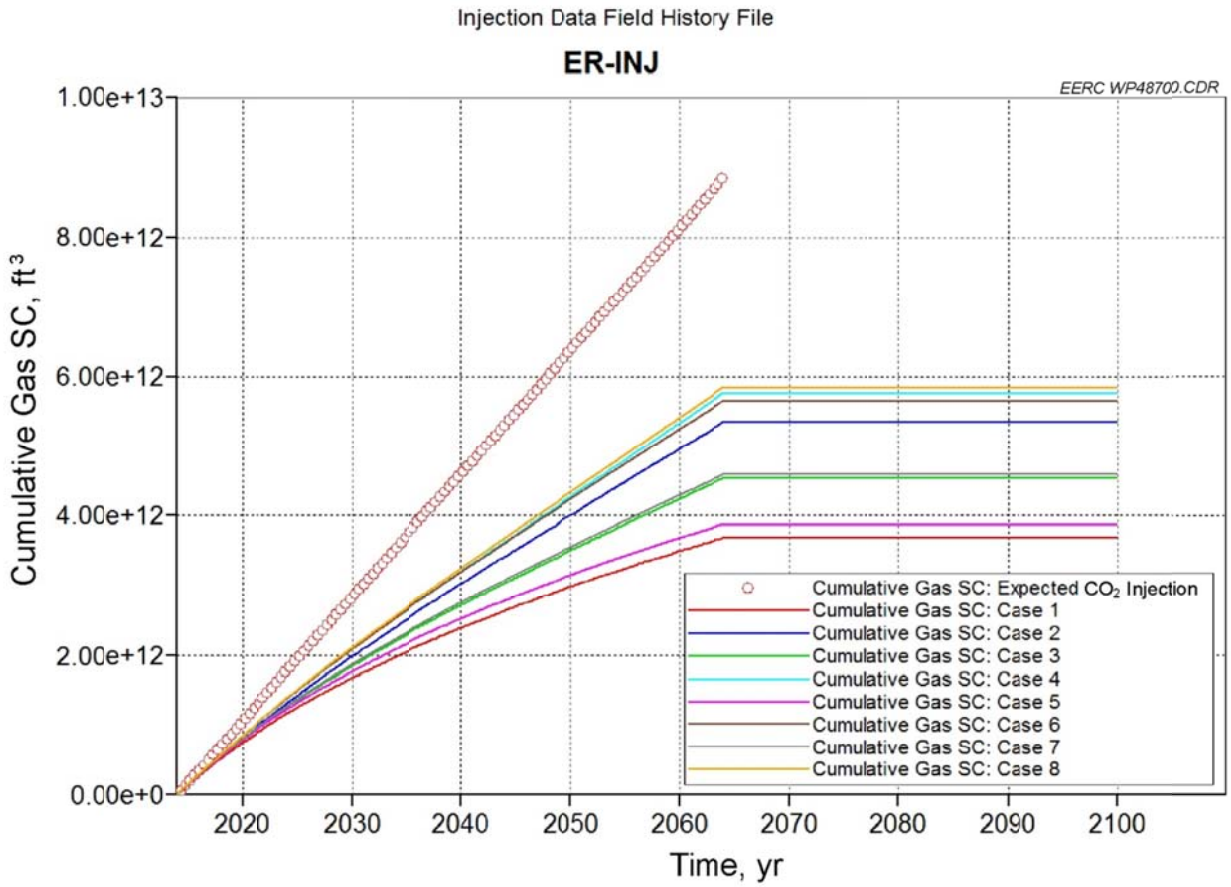

Figure B-9. Cumulative injection and expected injection at Edmonton–Redwater for Cases 1–8 of Scenario 2.

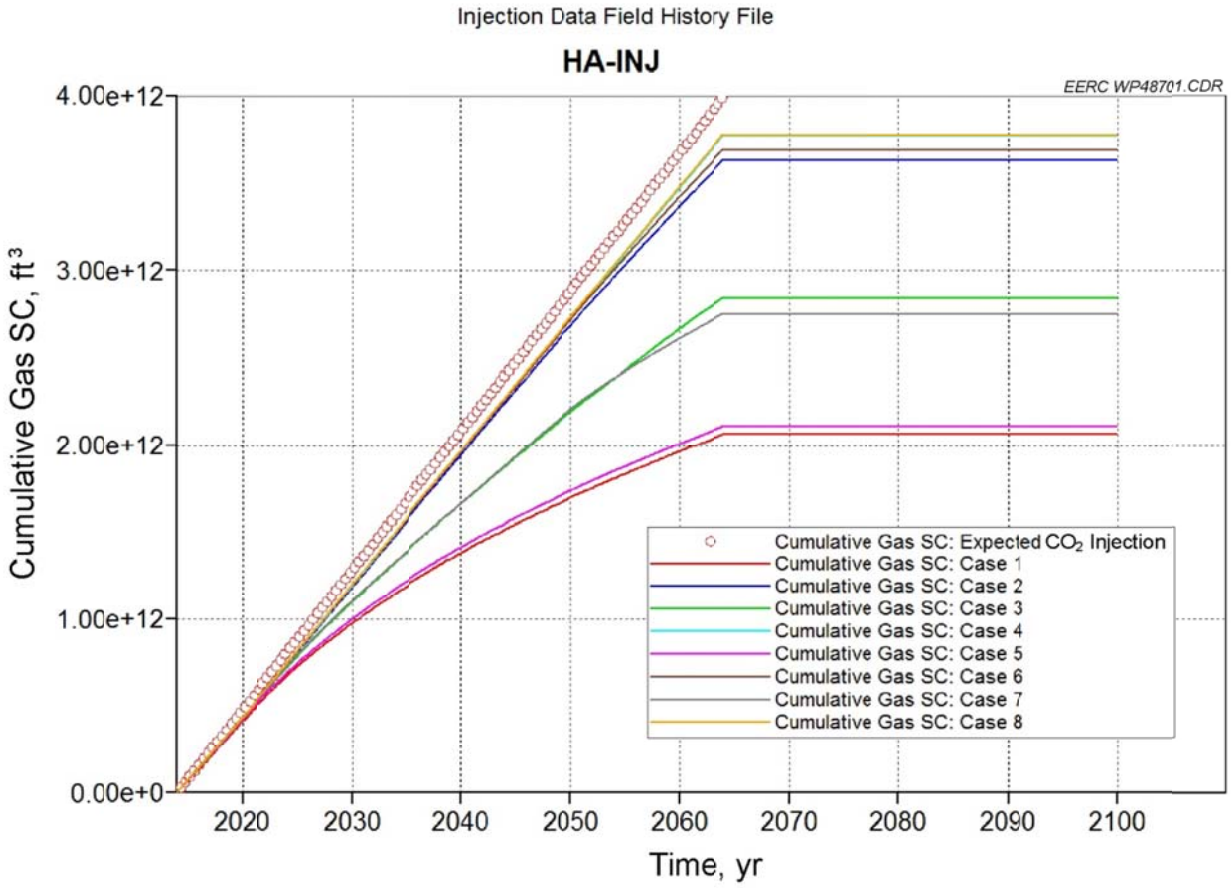

Figure B-10. Cumulative injection and expected injection at Hanna for Cases 1–8 of Scenario 2.

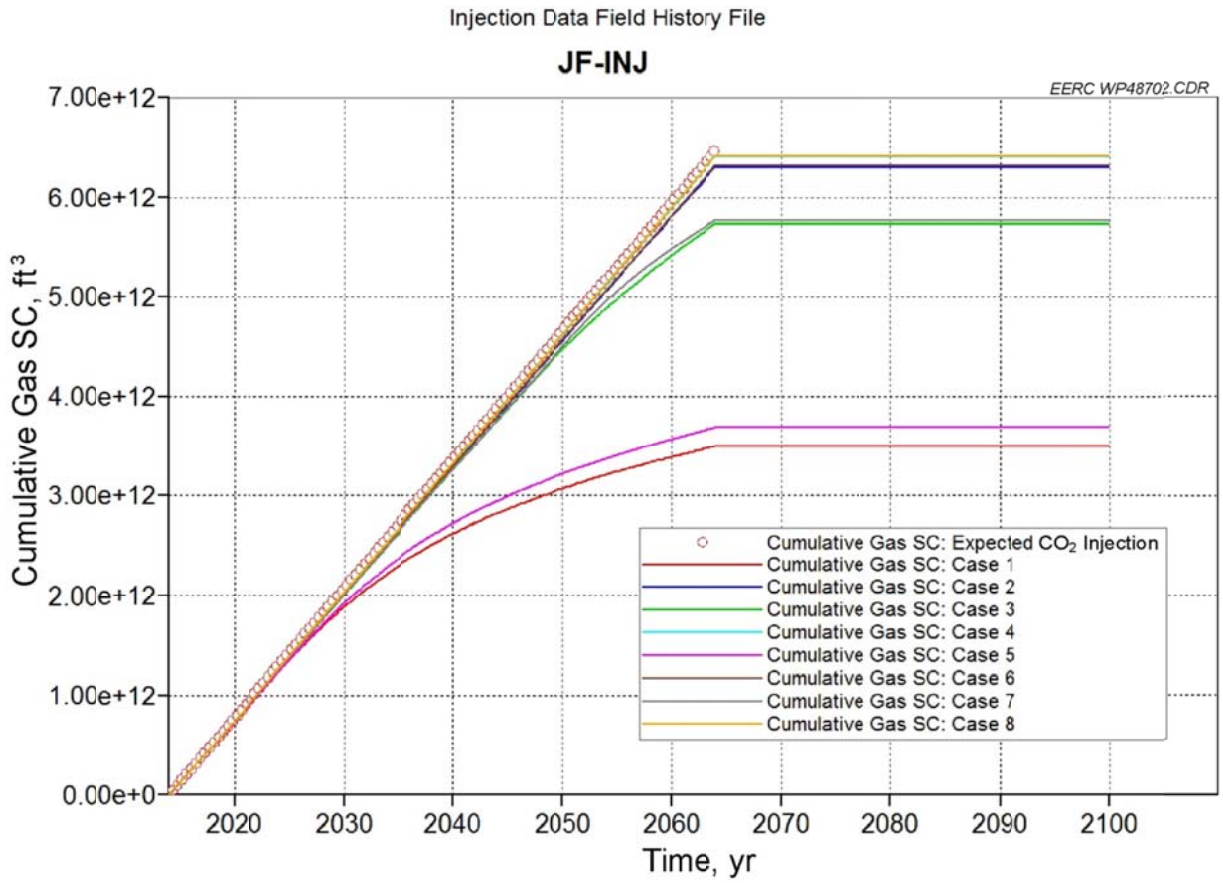

Figure B-11. Cumulative injection and expected injection at Joffe–Forestburg for Cases 1–8 of Scenario 2.

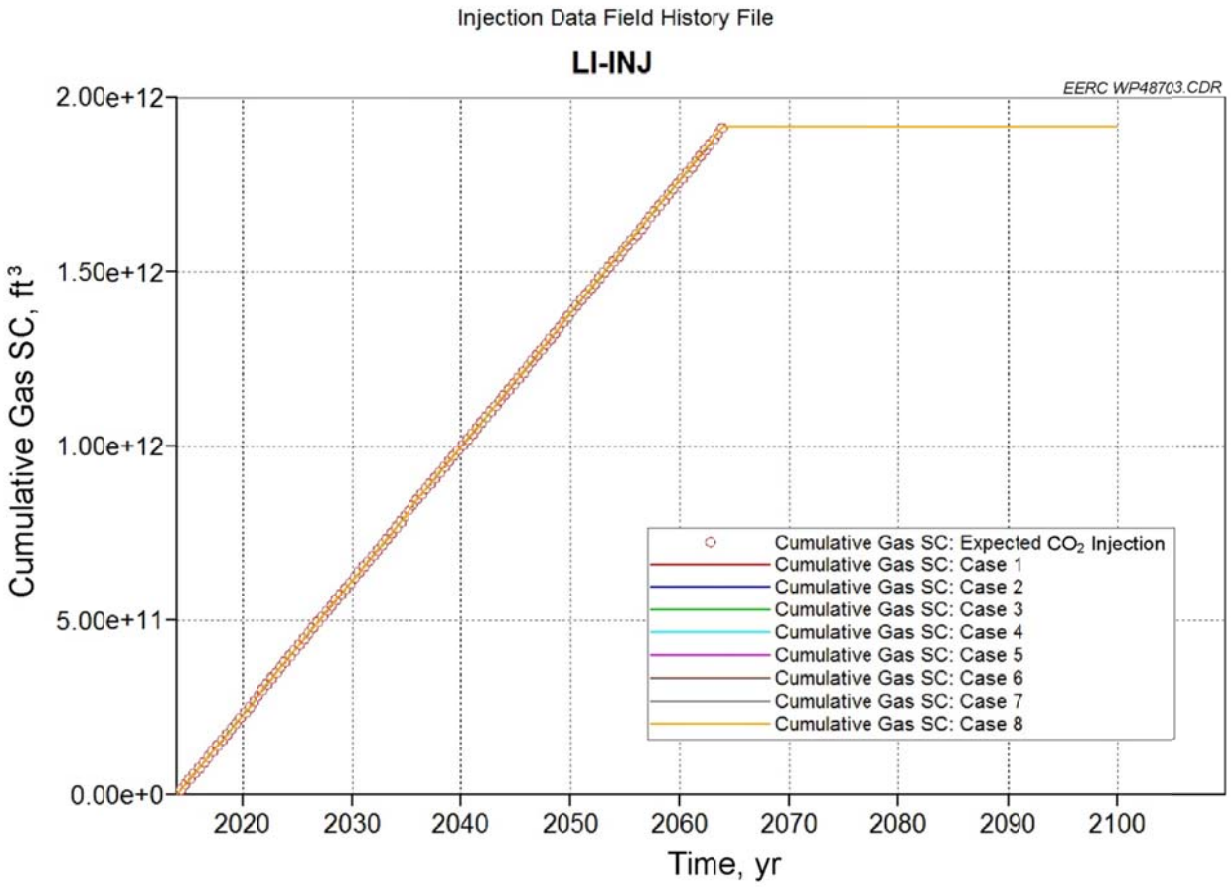

Figure B-12. Cumulative injection and expected injection at Lloydmister for Cases 1–8 of Scenario 2.

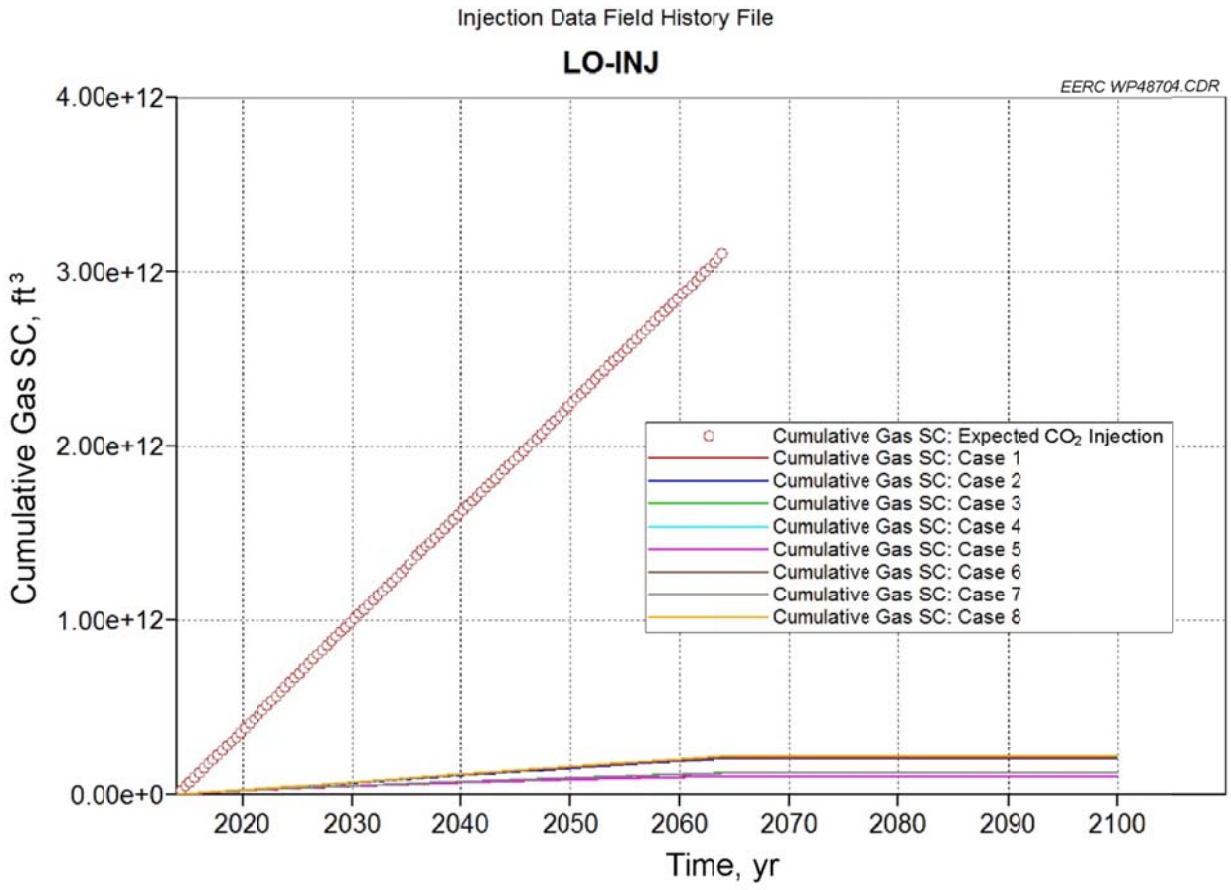

Figure B-13. Cumulative injection and expected injection at Leyland Olds for Cases 1–8 of Scenario 2.

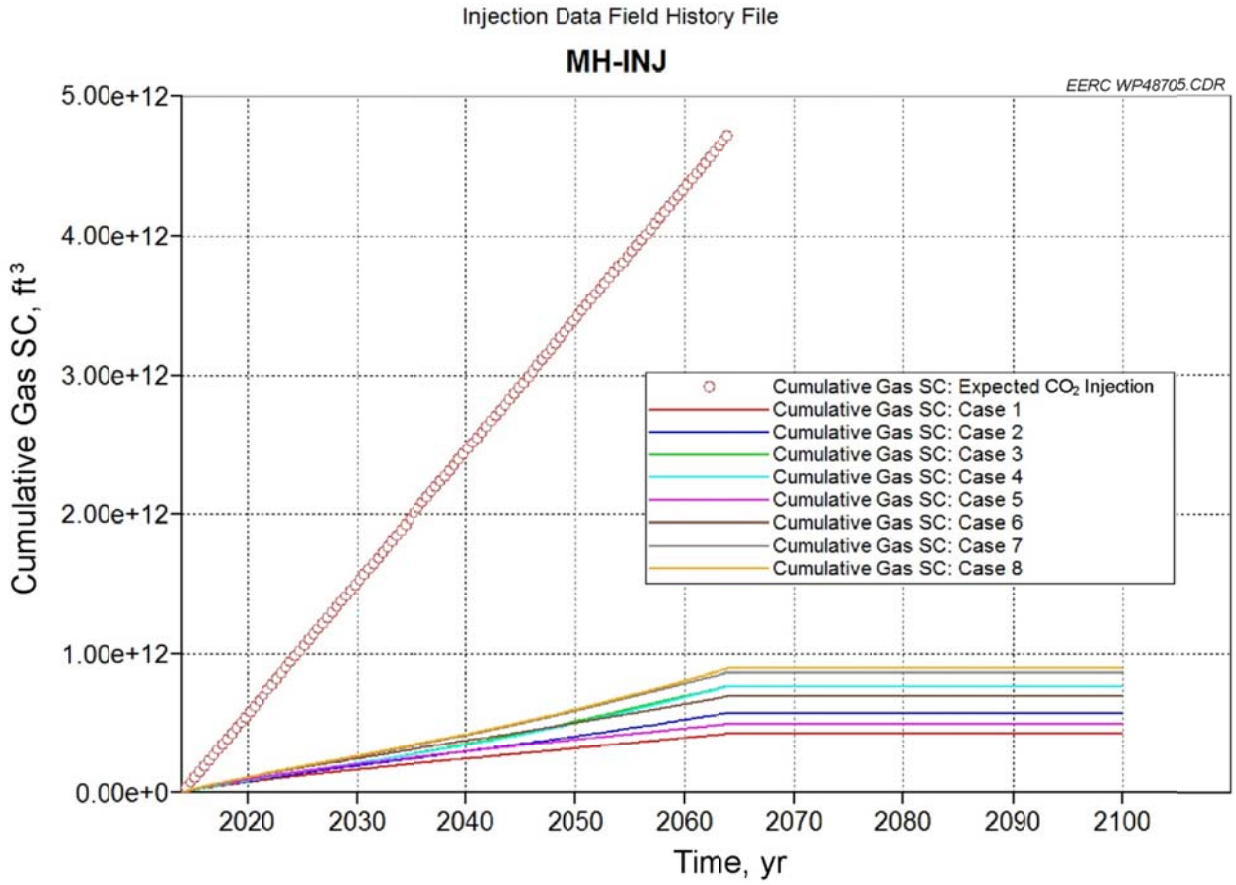

Figure B-14. Cumulative injection and expected injection at Medicine Hat–Empress for Cases 1–8 of Scenario 2.

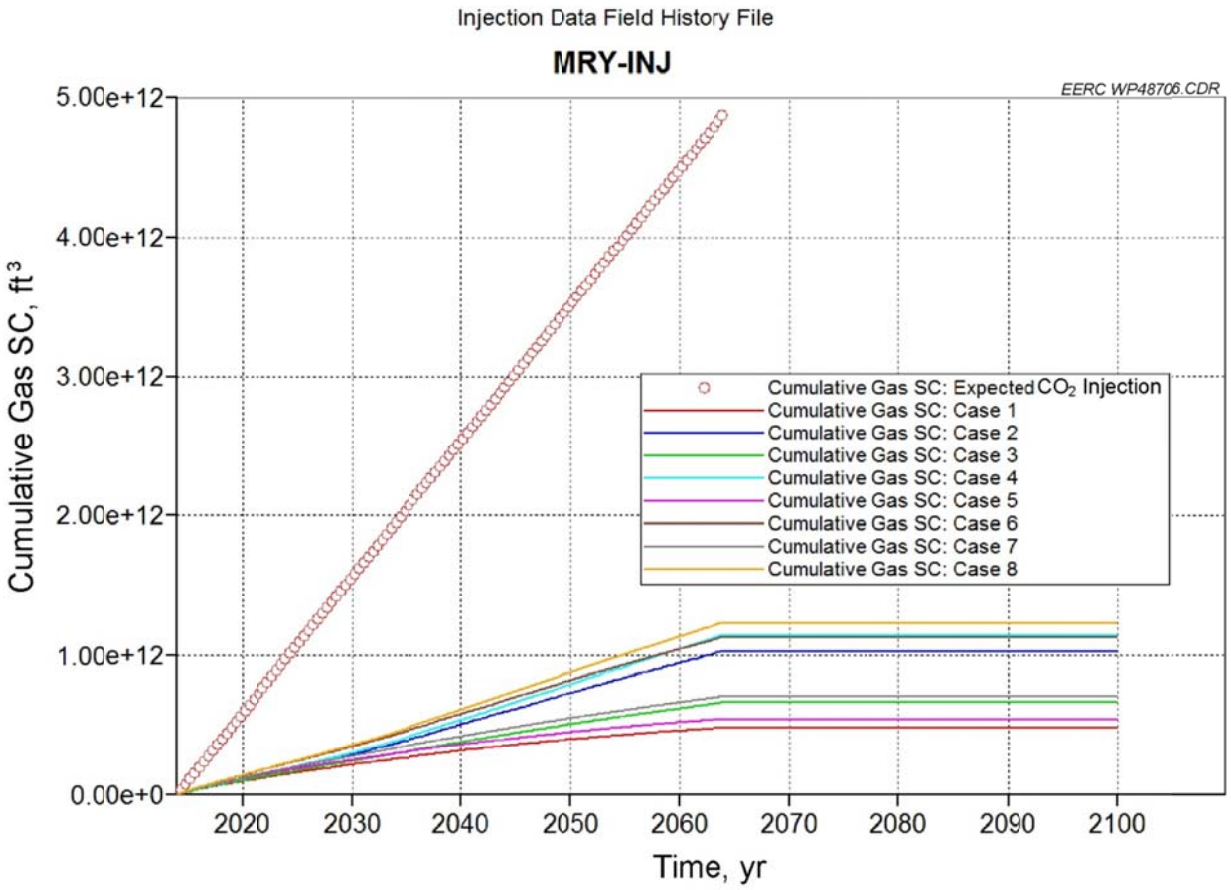

Figure B-15. Cumulative injection and expected injection at Milton R. Young for Cases 1–8 of Scenario 2.

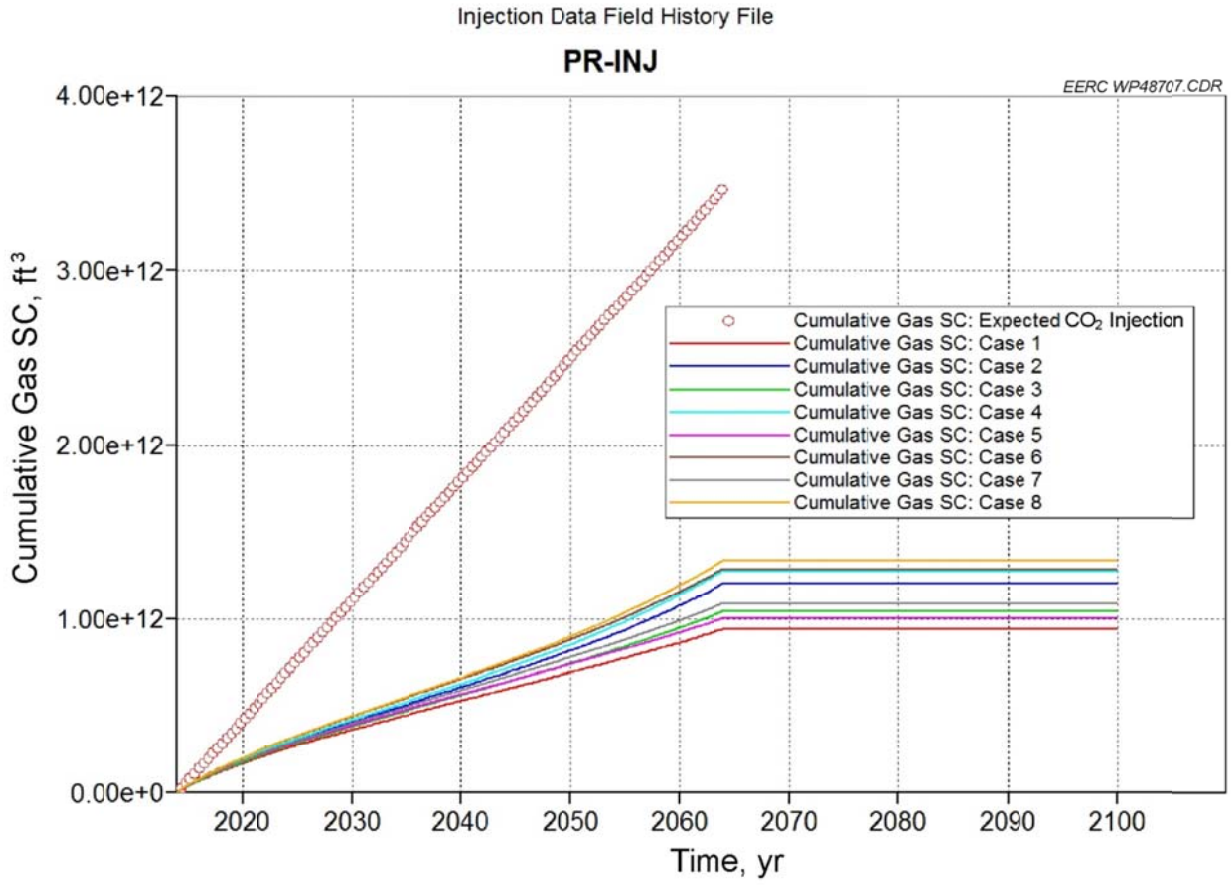

Figure B-16. Cumulative injection and expected injection at Poplar River for Cases 1–8 of Scenario 2.

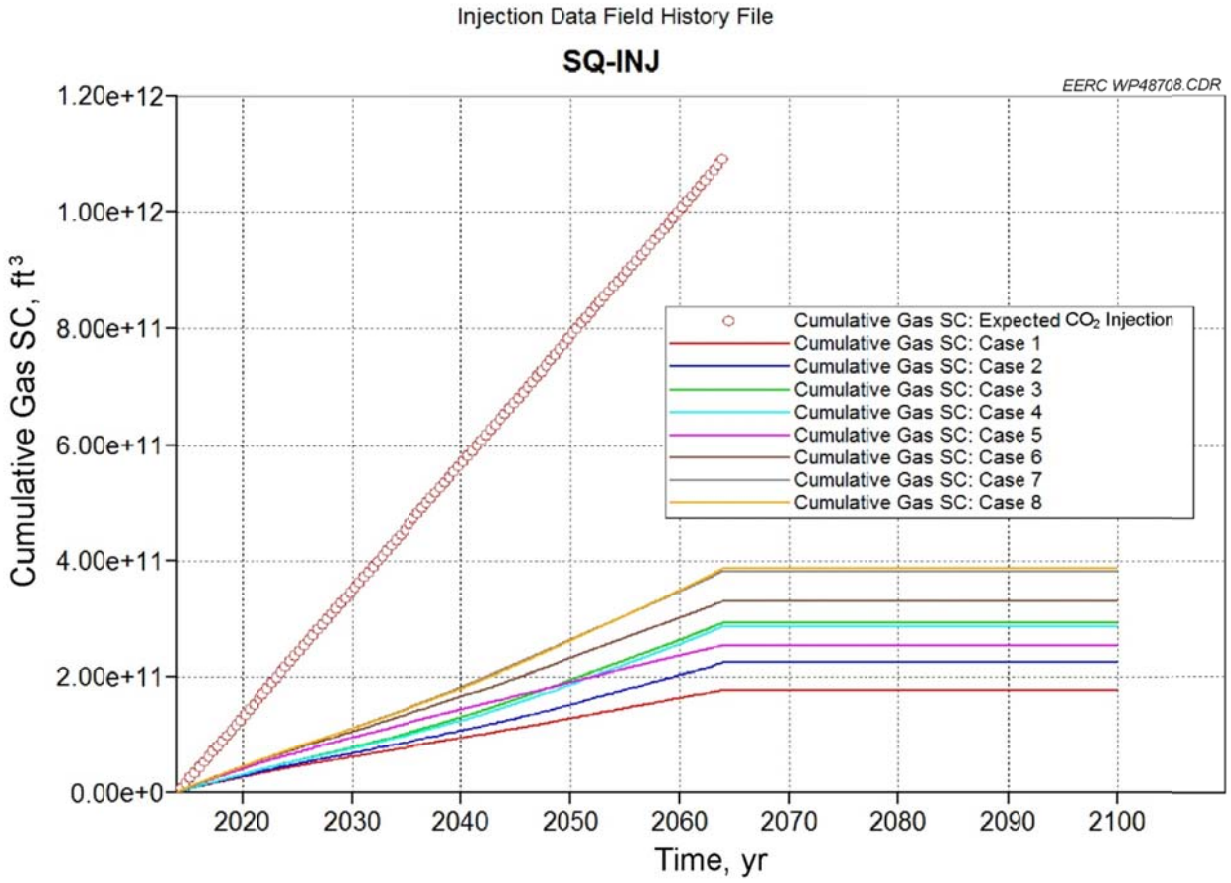

Figure B-17. Cumulative injection and expected injection at Shell Quest for Cases 1–8 of Scenario 2.

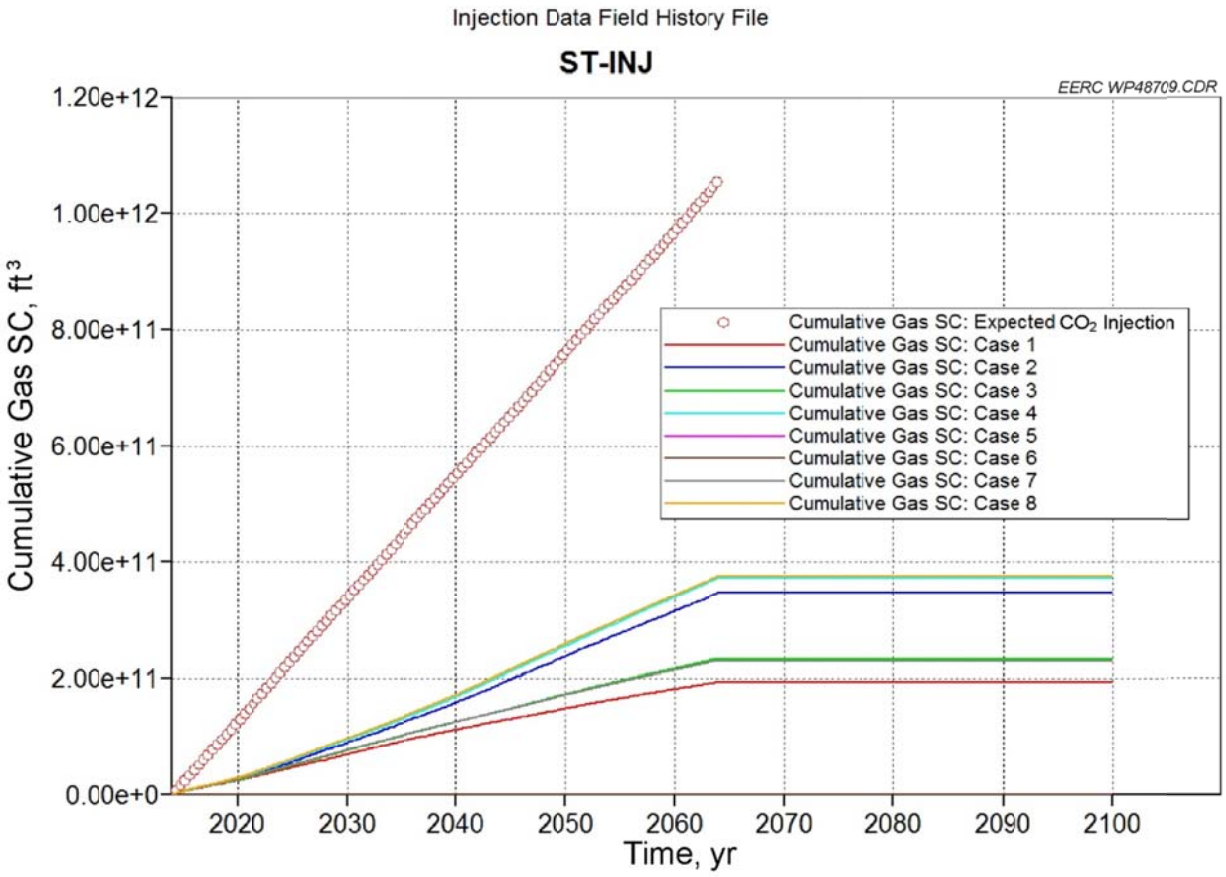

Figure B-18. Cumulative injection and expected injection at Stanton for Cases 1–8 of Scenario 2.

APPENDIX C

COMPARISONS OF PRESSURE DIFFERENCES FOR SCENARIO 2 (CASES 1–8)

COMPARISONS OF PRESSURE DIFFERENCES FOR SCENARIO 2 (CASES 1–8)

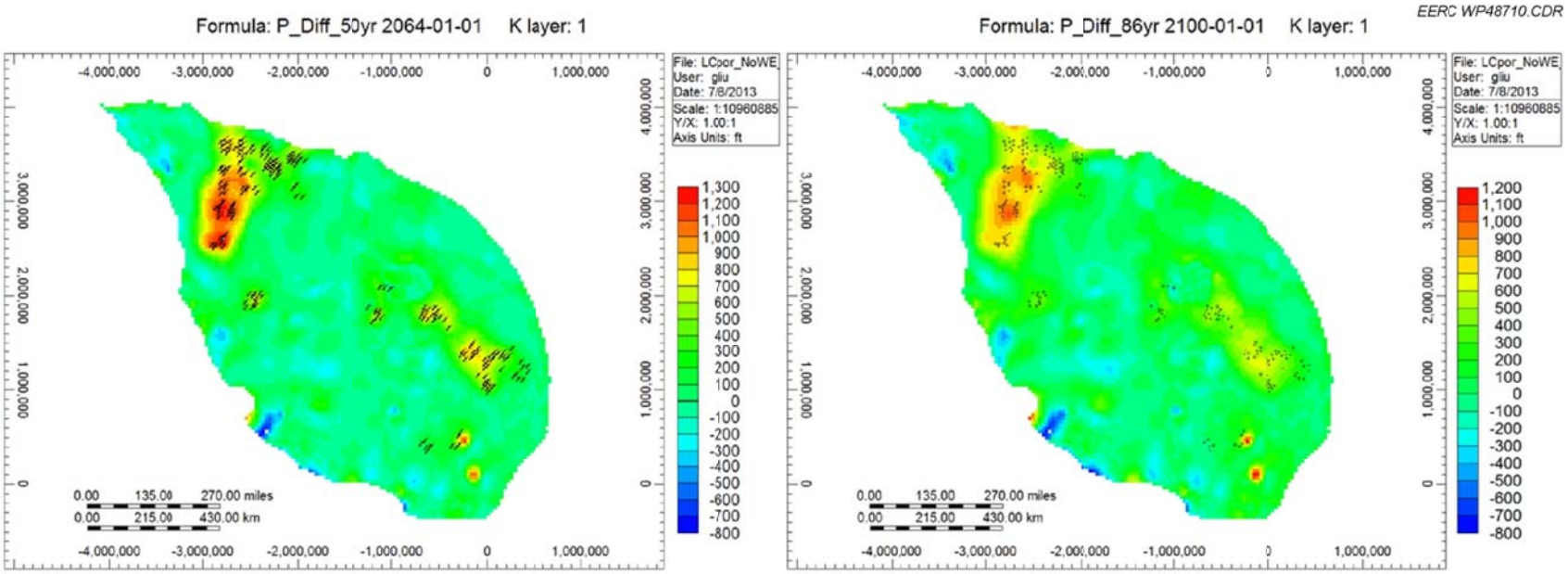

Figure C-1. Pressure differences after 50-year injection (left) and after 36-year postinjection (right) for Scenario 2: Case 1.

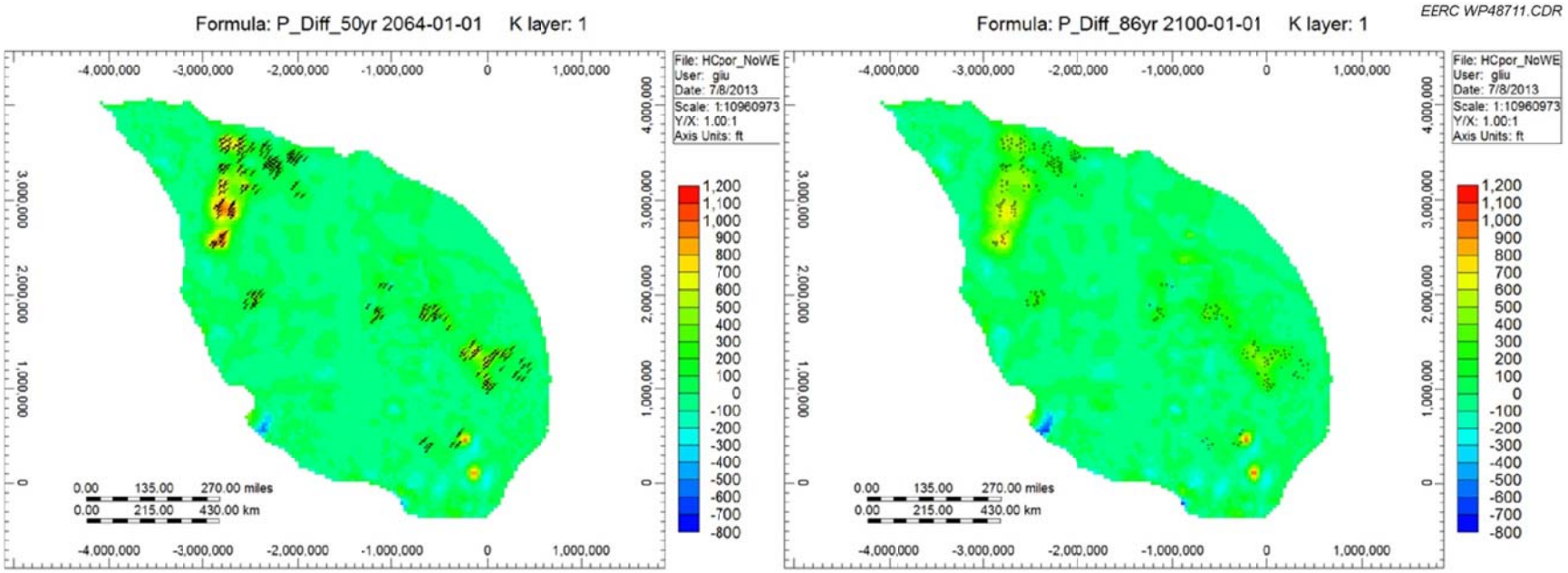

Figure C-2. Pressure differences after 50-year injection (left) and after 36-year postinjection (right) for Scenario 2: Case 2.

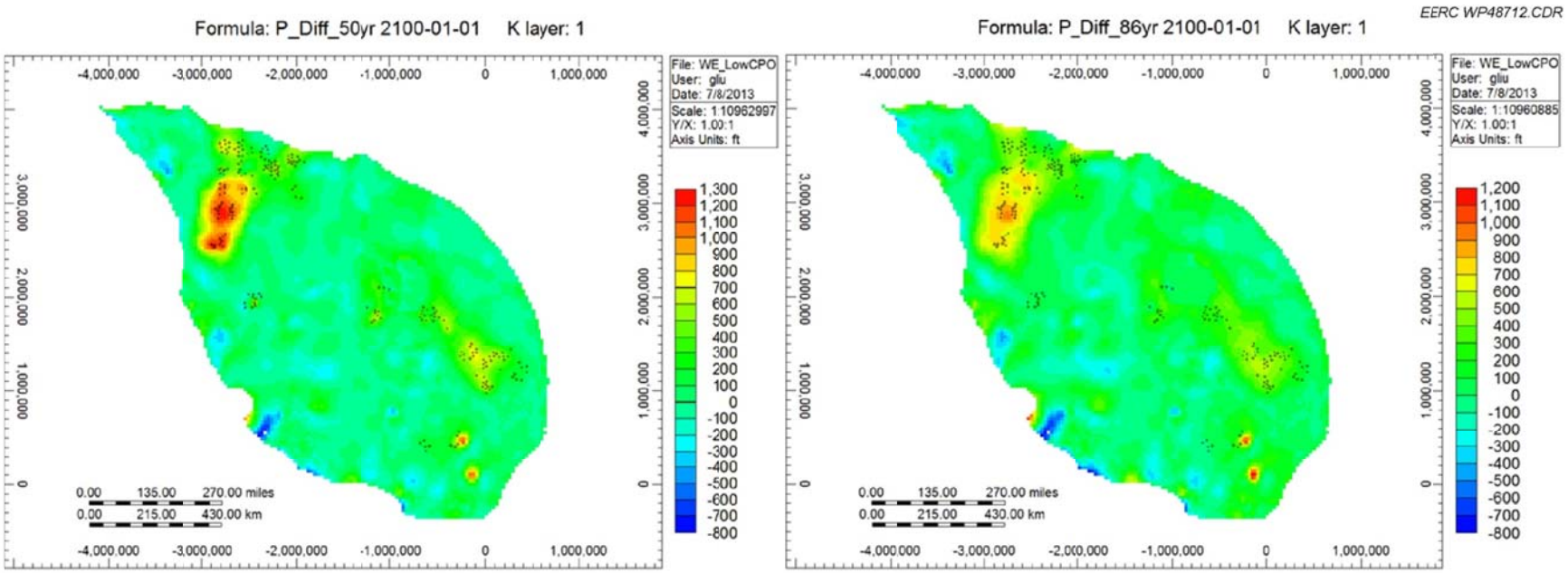

Figure C-3. Pressure differences after 50-year injection (left) and after 36-year postinjection (right) for Scenario 2: Case 3.

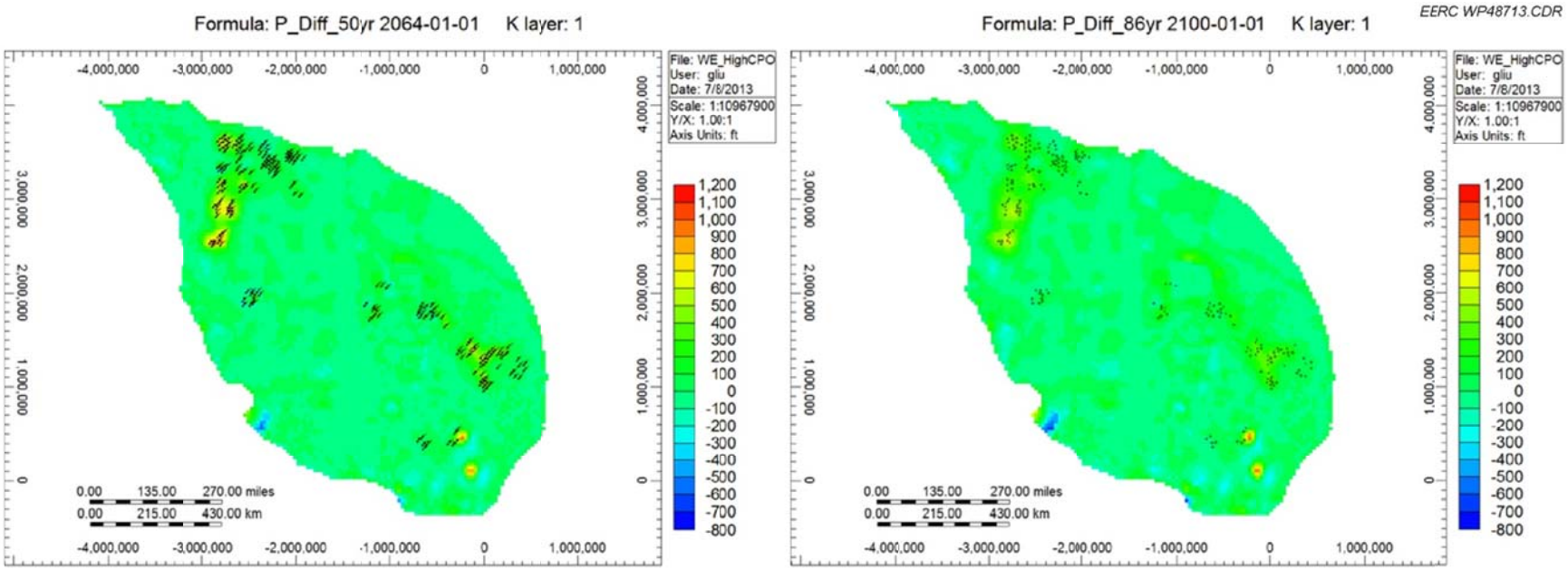

Figure C-4. Pressure differences after 50-year injection (left) and after 36-year postinjection (right) for Scenario 2: Case 4.

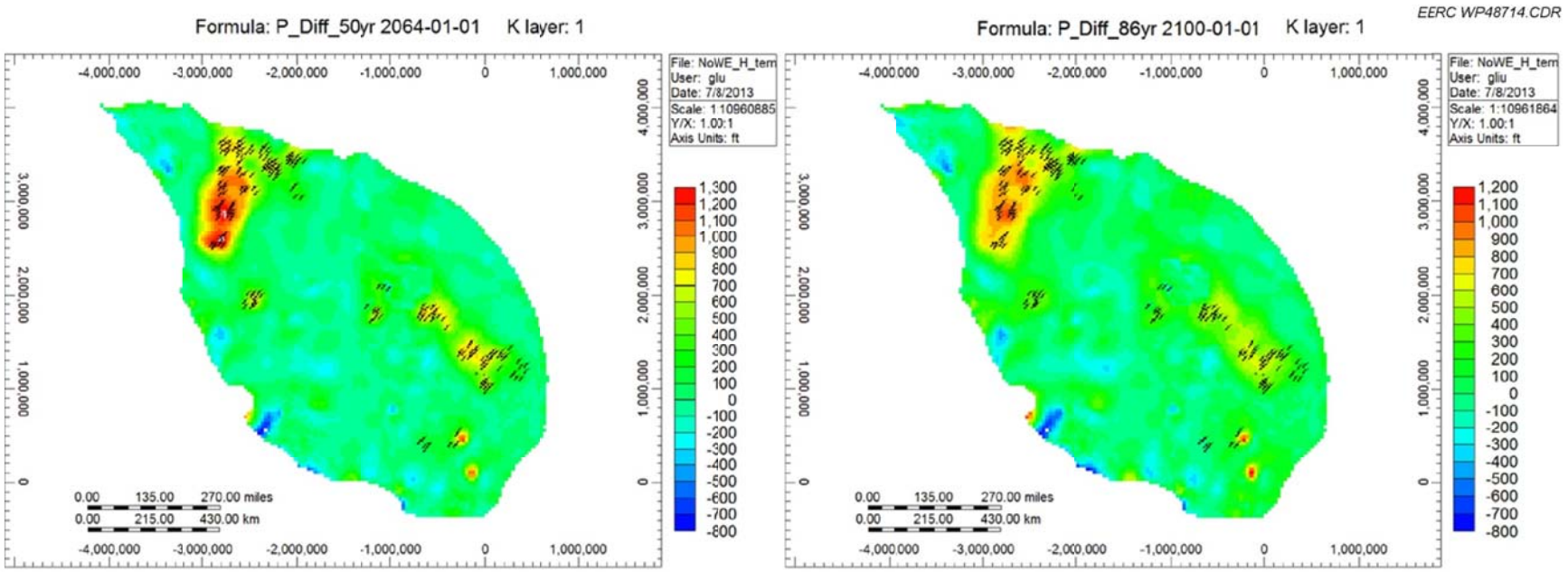

Figure C-5. Pressure differences after 50-year injection (left) and after 36-year postinjection (right) for Scenario 2: Case 5.

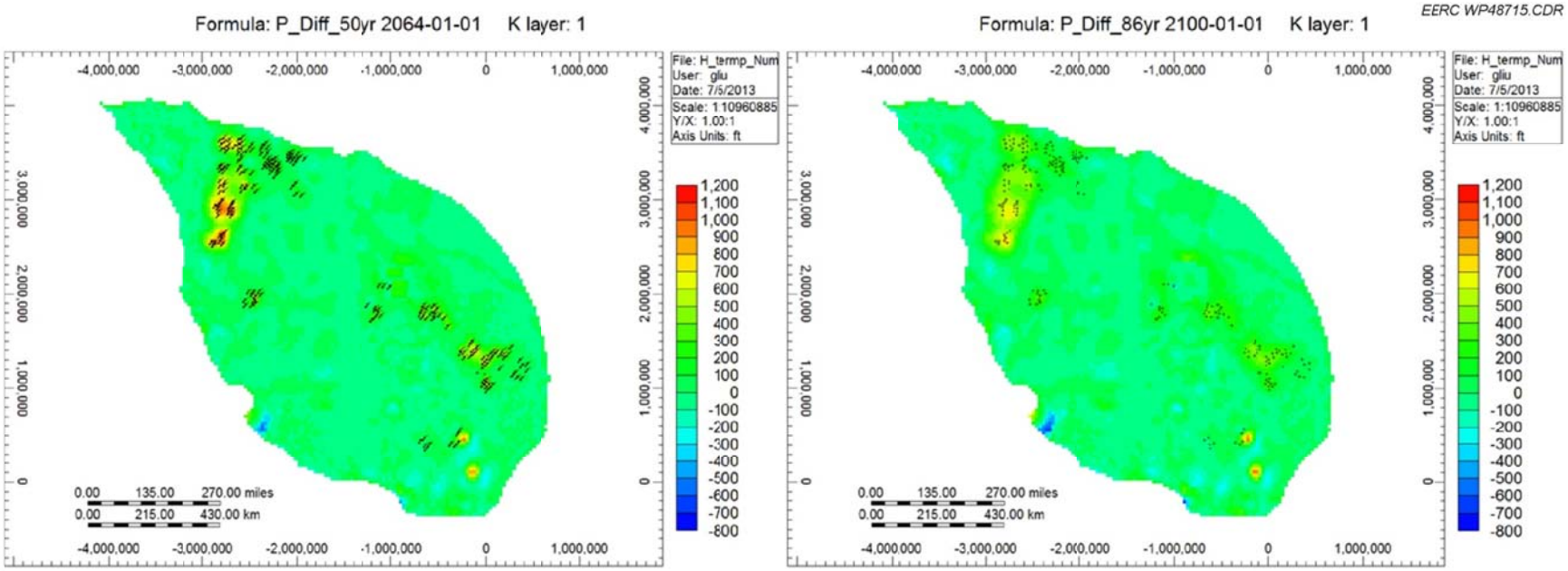

Figure C-6. Pressure differences after 50-year injection (left) and after 36-year postinjection (right) for Scenario 2: Case 6.

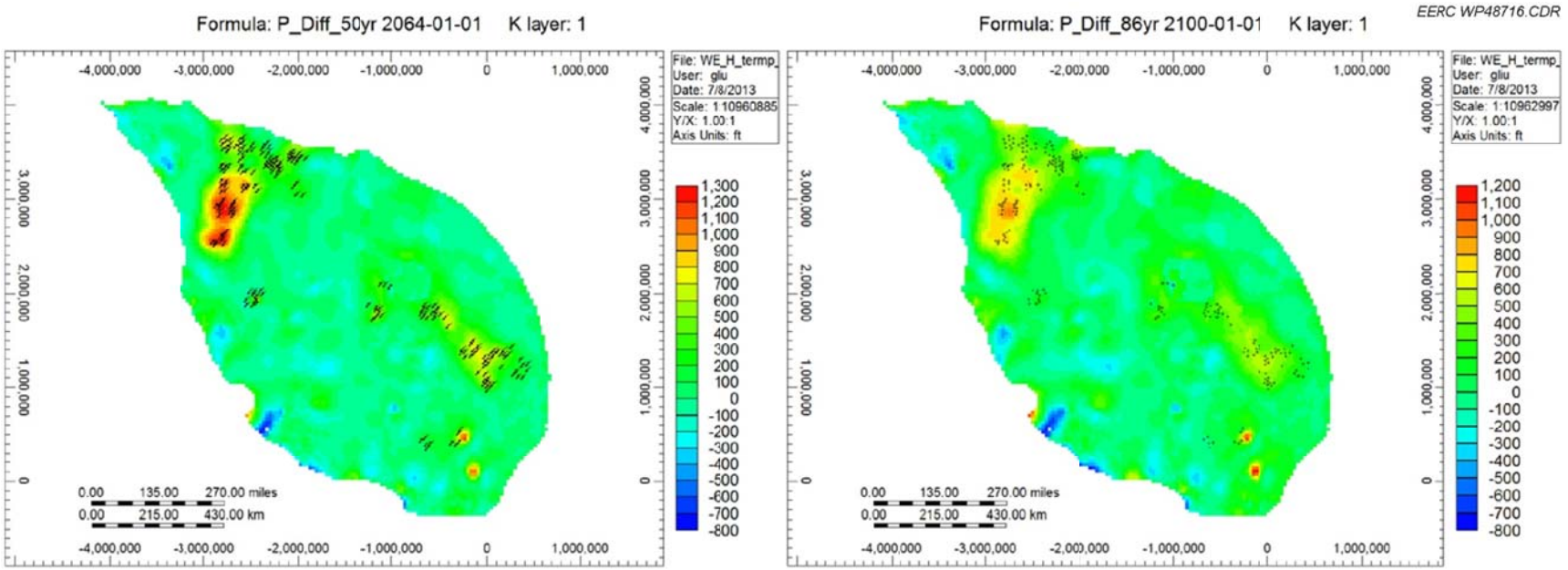

Figure C-7. Pressure differences after 50-year injection (left) and after 36-year postinjection (right) for Scenario 2: Case 7.

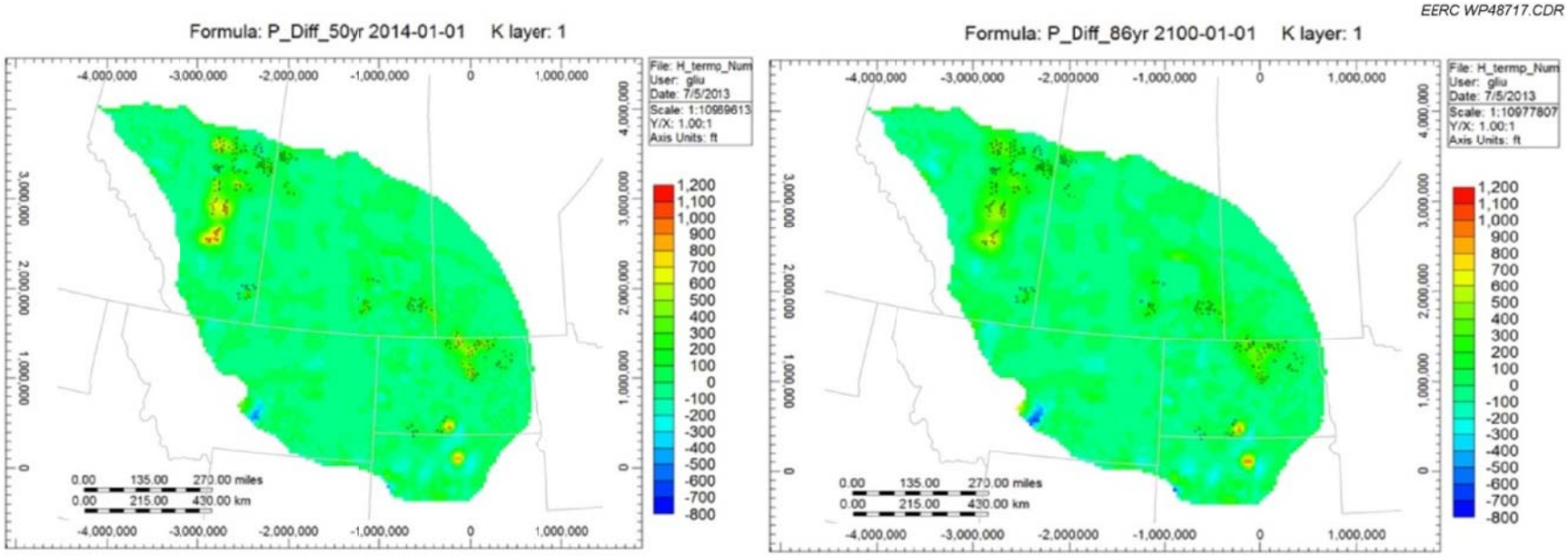

Figure C-8. Pressure differences after 50-year injection (left) and after 36-year postinjection (right) for Scenario 2: Case 8.